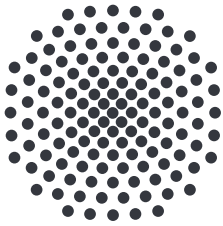


Superfluid Behaviour of Dipolar Quantum Gases

Masterarbeit
vorgelegt von
Michael Eisenmann



Universität Stuttgart

Hauptberichter: Prof. Dr. Tilman Pfau
Zweitberichter: Prof. Dr. Peter Michler

5. Physikalisches Institut
Universität Stuttgart
1. Juni 2018

Statutory Declaration

I herewith formally declare that I have written the submitted thesis independently. I did not use any outside support except for the quoted literature and other sources mentioned in the thesis.

I clearly marked and separately listed all of the literature and all of the other sources which I employed when producing this academic work, either literally or in content.

Stuttgart, June 1st, 2018

Michael Eisenmann

Deutsche Zusammenfassung

Ziel der vorliegenden Arbeit ist die Untersuchung suprafluider Phänomene in einem dipolaren Quantengas.

Das weitläufige Feld reibungsfreier Strömungen umfasst sowohl eher festkörperspezifische Effekte wie Supraleitung bei welcher beispielsweise der elektrische Widerstand vollständig verschwindet [42], als auch Phänomene aus der Atomphysik wie Suprafluidität, die einen Verlust von innerer Viskosität in flüssigen Gasen wie Helium beschreibt [43].

Im Folgenden sollen Stabilität wie generelles langreichweitiges Verhalten eines speziellen Suprafluids, nämlich eines dipolaren Bose-Einstein Kondensats aus Dysprosium untersucht werden. Dazu rühren wir mit einem oder mehreren Laserstrahlen gaußförmiger Intensitätsverteilung durch ^{162}Dy und ^{164}Dy -Atomwolken und untersuchen die resultierende Temperaturentwicklung. Geschieht die Bewegung langsam genug, so bleibt der suprafluide Zustand erhalten und keine Erwärmung ist beobachtbar. Überschreitet man allerdings eine kritische Geschwindigkeitsgrenze, so beginnt sich das Kondensat durch die Bewegung des Defekts aufzuheizen und der suprafluide Zustand wird zerstört.

Dieses Verhalten wurde theoretisch erstmalig 1941 von Lev Landau als ein Ergebnis der Erzeugung von Anregungen im Suprafluid beschrieben [41]. Seine Untersuchungen gipfelten in der Postulierung seiner berühmten kritischen, oder "Landau", Geschwindigkeit, die in beeindruckend simpler Weise das mikroskopische Anregungsspektrum des Mediums, in Form von dessen Dispersionsrelation, mit makroskopischen Flusseigenschaften in Verbindung setzt. Wir verwenden Dysprosium, weil es dasjenige Element mit dem höchsten magnetischen Moment im Periodensystem ist [33], was es uns ermöglicht, Anisotropie durch die Dipol-Dipol-Wechselwirkung in die Dispersionsrelation einzubringen [40]. Dadurch wiederum unterscheiden sich die kritischen Geschwindigkeiten gemäß Landaus Vorhersagen parallel und orthogonal zu der Dipolrichtung. Diese richtungsabhängige Aufspaltung wurde zwar schon theoretisch vorhergesagt [49], doch wir sind die Ersten die diese Prognosen in einem dipolaren Quantengas experimentell verifizieren.

Zur Bestimmung der kritischen Geschwindigkeit rühren wir mit einem attraktiv wirkenden Laserstrahl der Wellenlänge 532 nm linear durch das Kondensat. Die Erwärmung bei verschiedenen Rührgeschwindigkeiten wird daraufhin verglichen und durch Anlegen einer entsprechenden Fit-Funktion [45] die kritische Geschwindigkeit ermittelt, wobei experimentelle und numerische Simulationsergebnisse in überragender Übereinstimmung miteinander und mit theoretischen Vorhersagen für das Verhalten eines homogenen Bose-Einstein Kondensates [40] stehen.

Es konnte verifiziert werden, dass die kritische Geschwindigkeit in einem Dysprosium BEC durch die Ausrichtung der mikroskopischen Dipole manipuliert werden kann, so dass sie sich parallel und orthogonal zu der Projektion der Dipole in die Röhrebene unterscheiden. Dieser Effekt wird nicht durch reine Dichteänderungen, hervorgerufen durch die Dipol-Dipol-Wechselwirkung, erzeugt, und der genaue Wert der Grenzgeschwindigkeit kann durch Adaption der Wolkenform beziehungsweise durch Änderungen an den Rührereigenschaften modifiziert werden.

Um das qualitative Verhalten der kritischen Geschwindigkeit weiter zu analysieren wurden zusätzliche Simulationen bei unterschiedlichen Rührbedingungen durchgeführt. Dabei konnte unter anderem gezeigt werden, dass das mehrmalige Abfahren desselben Streckenabschnitts in den Simulationen ein nährungsweise lineares Heizverhalten erzeugt. Wird das magnetische Feld zum Anordnen der Dipole auch in Zwischenstufen zwischen orthogonaler und paralleler Anordnung zur Kondensatebene angelegt, so konnten wir eine monotone Abnahme der kritischen Geschwindigkeit mit zunehmendem Drehwinkel beobachten. Fährt man mit dem Laserstrahl entlang beliebiger Winkel relativ zur Dipolprojektion, so nimmt die Landau-Geschwindigkeit zwar monoton aber nicht linear zur orthogonalen Ausrichtung hin ab. Dieses Verhalten ist in Übereinstimmung mit theoretischen Vorhersagen in [47] die diese Nichtlinearität damit erklären, dass die Ausbreitungsrichtung der erzeugten Anregungen nicht notwendigerweise entlang des Rührweges liegen muss. Erhöht man die Amplitude der Strahlbewegung, so konnte eine signifikante Erhöhung der resultierenden Wärmeentwicklung und ein Verschieben des maximalen Heizpunkts zu höheren Geschwindigkeiten beobachtet werden. Eine Verbreiterung des Rührers führt ebenso zu einer höheren Wärmeentwicklung, allerdings nimmt die kritische Geschwindigkeit hier ab. Erhöht man die Potentialtiefe des Rührers, so nimmt die erzeugte Wärmemenge weiter zu. Zu guter Letzt wurde noch die Kontaktwechselwirkungsstärke adaptiert. Die Idee war hier durch Vergleich der experimentellen und numerischen Ergebnisse den exakten Wert für diesen Parameter in ^{162}Dy zu bestimmen, der bisher nicht genau bekannt ist. Durch unsere Ergebnisse konnten wir ihn auf den Bereich $121 a_0 < a_s^{\text{Dy},162} < 161 a_0$ eingrenzen, was ziemlich exakt mit früheren Ergebnissen der Stanford-Gruppe von Benjamin Lev übereinstimmt [35,51,58,59].

Zusätzlich zur Bestimmung der kritischen Geschwindigkeit in unserem System beschäftigten wir uns auch mit der Erzeugung von Vortices. Diese sind von besonderer Bedeutung für den Nachweis von Suprafluidität, da sie nur unter dieser Bedingung auftreten können.

Um zu verifizieren, dass unsere numerischen Simulation in der Lage sind Vortexerzeugungen abzubilden, rotieren wir kreisförmig mit zwei identischen Laserstrahlen um die Kondensatmitte. Im Gegensatz zu den zuvor besprochenen Simulationsläufen benutzen wir nun repulsive Strahlen, da diese zur Vortexerzeugung besser geeignet sind [37]. Im realen Experiment wurde dafür im Rahmen dieser Arbeit eine 405 nm Laserdiode aufgebaut und vollständig in das nötige EOD-System eingekoppelt, sowie der Strahl ausgerichtet.

Die Hauptherausforderung in den Vortexsimulationen stellte das Auffinden eines funktionierenden Parameterbereichs bezüglich Rührer- und Falleneigenschaften dar. Im Zuge unzähliger Versuche stellte sich heraus, dass eine signifikante Evolutionszeit nach dem Abschließen der Strahlbewegungen notwendig ist, um die Ausbildung von Vortices zu ermöglichen. Abhängig von den exakten Systemparametern zeigt sich, dass eine Rührzeit von etwa $t_{\text{stir}} = 300 \text{ ms}$ und eine darauf folgende Evolutionsdauer von circa $t_{\text{evo}} = 400 \text{ ms}$ das Minimum an zu simulierender Zeit darstellen.

Die kritische Rührfrequenz zur Erzeugung der ersten Vortices wurde dann untersucht und befand sich in grober Übereinstimmung mit theoretischen Vorhersagen. Der Erzeugungsvorgang stellte sich als äußerst sensitiv bezüglich Inhomogenitäten in den Fallenparametern dar, was bei zukünftigen experimentellen Verifikationen unserer Ergebnisse möglicherweise zu Problemen bezüglich Messungenauigkeiten und langfristigen Drifts in realen Fallenparametern führen könnte.

Von besonderem Interesse war für uns das Verhalten von Vortex-Gittern unter Variation

der Dipol-Ausrichtung, da das die große Stärke unseres Material Dysprosium darstellt. Bei Untersuchungen des Grundzustands konnten wir zeigen, dass die kritische Rotationsfrequenz des Mediums von der Ausrichtung der Dipole abhängt. Mit zunehmendem Kippwinkel der Dipole in die Kondensatebene nahm die nötige Frequenz zur Vortexerzeugung zu und die Vortices änderten ihre relative Ausrichtung. Ordnen sich diese normalerweise dreiecksförmig in einem Abrikosov-Gitter an [65], so konnten wir eine Änderung hin zu einer linearen Anordnung [64] entlang der Dipolprojektionsrichtung beobachten. Dieses Verhalten konnte in einem dynamischen System mit zwei kreisförmigen Rührern verifiziert werden, wobei der Kontrast und damit die Sichtbarkeit der Vortex-Kerne deutlich abgenommen hat.

Alles in allem stellen die Resultate dieser Arbeit eine Zusammenfassung der suprafluiden Eigenschaften in Dysprosium Bose-Einstein Kondensaten dar, wobei unsere Ergebnisse eine überwältigende Übereinstimmung zwischen experimentellen, numerisch simulierten und theoretisch prognostizierten Verhaltensmustern darstellen.

Contents

| | | |
|----------|--|-----------|
| 1 | Introduction | 1 |
| 2 | Bose-Einstein condensation of Dysprosium | 3 |
| 2.1 | Bose-Einstein Condensation | 3 |
| 2.2 | Two-body Interactions | 4 |
| 2.2.1 | Contact-Interaction | 4 |
| 2.2.2 | Dipolar interaction | 5 |
| 2.3 | Theoretical Description | 7 |
| 2.3.1 | Mean-field and Extended Gross-Pitaevskii Equation | 7 |
| 2.3.2 | Weak Interaction Limit - Variational Method | 8 |
| 2.3.3 | Strong Interaction Limit - Thomas-Fermi Approximation | 9 |
| 2.3.4 | Beyond Mean-Field Effects - Quantum Fluctuations | 10 |
| 2.3.5 | Complete effective GPE | 11 |
| 2.4 | Excitations in a dBEC | 11 |
| 2.4.1 | Speed of Sound in a Homogeneous Dipolar Gas | 11 |
| 2.4.2 | Anisotropic Speed of Sound | 13 |
| 3 | Experimental Setup | 14 |
| 3.1 | Dysprosium | 14 |
| 3.2 | Creation of Dysprosium BECs | 15 |
| 3.3 | Time-Averaged Potentials by an Electro-Optical Deflector (EOD) | 17 |
| 4 | Numerical Simulation Methods | 21 |
| 4.1 | Simulated Stirring Characteristics | 21 |
| 4.2 | Mathematical and Numerical Tools | 22 |
| 4.2.1 | Split-step method | 22 |
| 4.2.2 | Crank-Nicolson Scheme | 23 |
| 4.2.3 | Real Time Evolution | 24 |
| 4.2.4 | Imaginary Time Evolution | 25 |
| 4.3 | Explicit Stirring Procedures | 26 |
| 4.3.1 | Linear Stirring | 26 |
| 4.3.2 | Circular Stirring | 27 |
| 4.4 | Rescaling of Simulation Data | 28 |

| | | |
|----------|---|-----------|
| 5 | Breakdown of Superfluidity | 30 |
| 5.1 | Landau Critical Velocity | 30 |
| 5.2 | Anisotropy in the Critical Velocity of Dysprosium | 32 |
| 5.3 | Qualitative Behaviour of the Critical Velocity | 37 |
| 5.3.1 | Anisotropic Heating of a Dipolar Superfluid | 37 |
| 5.3.2 | Variation of the Stirring Angle | 39 |
| 5.3.3 | Variation of the Stirring Amplitude | 40 |
| 5.3.4 | Variation of the Beam Size | 41 |
| 5.3.5 | Variation of the Potential Depth | 42 |
| 5.3.6 | Influence of the Number of Stirring Cycles | 43 |
| 5.3.7 | Variation of the S-Wave-Scattering Length | 44 |
| 6 | Vortices | 46 |
| 6.1 | Theoretical Background | 46 |
| 6.2 | Vortex Creation | 48 |
| 6.2.1 | Forming Mechanisms | 49 |
| 6.2.2 | Critical Frequency | 52 |
| 6.3 | Influence of Anisotropic Trapping | 54 |
| 6.4 | Vortices at Tilted Magnetic Fields | 56 |
| 6.4.1 | Static solutions | 56 |
| 6.4.2 | Dynamic solutions | 58 |
| 7 | Conclusion and Outlook | 60 |
| A | Appendix | 62 |
| A.1 | Speed of Sound in a strongly trapped Dipolar Gas and Roton excitation . . | 62 |
| B | Bibliography | 65 |

1 Introduction

Technological progress and increasing automation in our modern societies create the necessity for the availability of arbitrarily large amounts of electrical energy even at very remote locations. As our demand is still mostly met by a centralised system consisting of a small number of large-scale power plants, the ability for low-loss energy transfer becomes increasingly important.

The most promising path towards this goal was opened in 1911 when Heike Onnes discovered the phenomenon of superconductivity [67], a state with exactly zero electrical resistance.

The very broad topic of dissipationless flow knows many manifestations, for example as the already discussed vanishing of electrical resistance [42], or as loss of inner viscosity in liquid helium [43] forming a superfluid state. These two phenomena, superfluidity and superconductivity, are manifestations of the same phenomenon [72] either in charged or neutral matter.

These parallels motivate us to try to get deeper insights into the stability and long-range behaviour of superfluid systems in our quantum gas. Atomic physics is known as a field for ground breaking proof of concept research [74,75,76], as it typically enables precise control of the system's external degrees of freedom [77]. A good example are ultracold quantum gases, allowing the study of many-body phenomena known from solid state physics [68].

In this thesis we investigate the stability and behaviour of a superfluid state in the form of a Dysprosium Bose-Einstein condensate. We show that the response of such a state to an impurity moving through it is highly dependent on the objects velocity. Below a certain threshold superfluidity persists, while surpassing this threshold results in the creation of excitations and the breakdown of the superfluid state. This behaviour could be explained by Lev Landau in 1941 through the creation of excitations in the superfluid [41]. He was able to postulate his well-known critical, or "Landau", velocity, connecting in a remarkably easy way the microscopic dispersion relation of a superfluid system to its macroscopic flow properties. Using Dysprosium, the element with the highest magnetic moment in the periodic system [33] further creates anisotropies in the condensates dispersion relation [40]. This enables us to verify a direction dependency of the sound velocity, as well as the critical velocity in our dipolar system, through experimental investigations and full numerical simulations. This behaviour has already been theoretically predicted [49] but was never observed before our work.

Through variations in the linear stirring process, potentially in the form of different stirring angles relative to the dipoles tilt [47] or through modifications in the stirrer potential [37], the qualitative scaling behaviour of the critical velocity in our system can be studied. Depending on the trajectory of the impurity, in our case an attractive or repulsive laser beam, different excitations can be created, ranging from phonons for linear stirring [69] to vortices, as carriers of angular momentum, for stirring circularly [50].

Vortex creation is of special interest when probing for superfluidity, as their existence is clear evidence thereof [61]. While vortices have been observed many times in isotropic systems [50,62], their possible existence and behaviour in anisotropic dipolar systems has until now only been theoretically predicted [70].

During this work, the relevant parameters for vortex creation through laser stirring in a Dysprosium BEC will be explored through numerical simulations. The dependency of vari-

ations in this values is of special interest, as experimental verifications of our numerical results might be limited by measurement inaccuracies and other experimental difficulties. Of most relevance will be the investigation of dipolar influences on vortex creation and arrangement when the dipole-orientation is varied. Following theoretical predictions we expect changes in the density distribution around the vortex core [71], as well as adaptations in the arrangement inside a vortex lattice from a typical triangular Abrikosov lattice [65] to linear lines [64] and possibly even more peculiar patterns [40]. The work in this thesis will compare analytical, numerical and experimental results in order to enable a well-rounded understanding of the relevant processes.

2 Bose-Einstein condensation of Dysprosium

All investigations on superfluidity discussed in this thesis will be conducted on a Bose-Einstein condensate of the rare earth metal Dysprosium. It is thus a natural choice to start this chapter with some deeper insights into the process of Bose-Einstein condensation in general, the most relevant forms of interaction in a dipolar gas, as well as their mathematical description.

2.1 Bose-Einstein Condensation

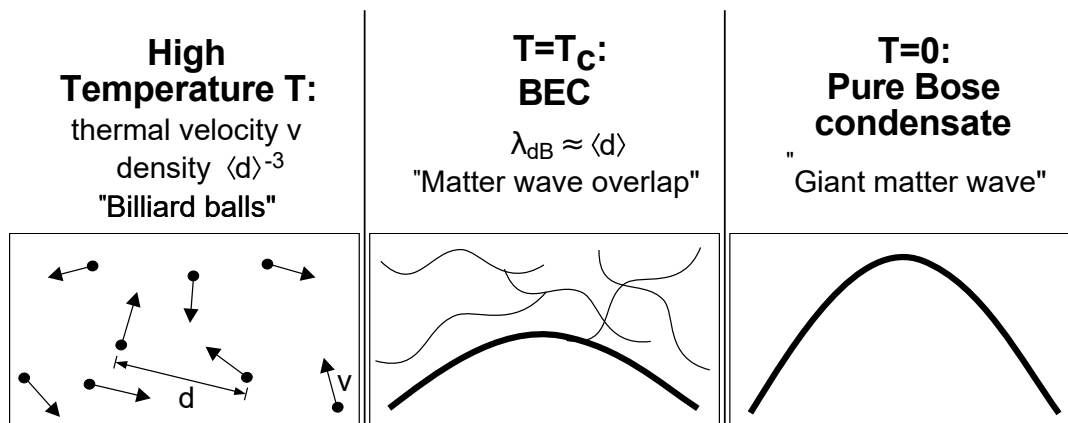


Figure 1: Simplified visualization of the condensation process from a thermal gas to a BEC. For high temperatures, meaning temperatures well above the critical temperature $T \gg T_C$, atomic gases can be understood as clusters of classical particles with mean distance $\langle d \rangle$. If the temperature is reduced, the former classical particles tend to behave like waves with the de-Broglie wavelength λ_{dB} . Around the critical temperature $T = T_C$, when λ_{dB} gets in the order of d , the wavefunctions can be regarded as overlapping until they form a single giant matter wave at the theoretical limit of $T = 0 K$. (Adapted from [5])

One of the most surprising states of matter, discovered in the last century, manifests itself in an ensemble of bosons, macroscopically occupying the lowest energy state with zero momentum $\vec{p} = \vec{0}$.

The concept of what is known today as "Bose-Einstein Condensation" was first predicted by Satyendranath Bose in 1924 for photons [1] and was later extended by Albert Einstein for non-interacting bosons [2,3]. More than 40 years after this predictions the first occurrence of a Bose-Einstein Condensate (BEC) could be experimentally detected in trapped, laser cooled, neutral atoms of ^{87}Rb and ^{23}Na [4,24].

To give a short theoretical inside into the very broad topic of Bose-Einstein condensation, we want to reflect upon the behaviour of an ideal Bose gas, during a cooling process into degeneracy. Let this discussion start with N particles confined into a volume V , resulting in a density n . The quantity typically used for characterising the onset of Bose-Einstein condensation is the phase space density

$$\mathcal{D} = n\lambda_{dB}^3 \quad (2.1.1)$$

depending on the thermal de-Broglie wavelength λ_{dB} . This temperature dependent wavelength can be understood as the coherence length of the involved particles [22]

$$\lambda_{\text{dB}}(T) = \sqrt{\frac{2\pi\hbar^2}{m k_B T}}, \quad (2.1.2)$$

where \hbar is the reduced Planck constant, m the particle mass, k_B the Boltzmann constant and T the temperature. One can show [22] that Bose-Einstein condensation does not arise directly at $\mathcal{D} = 1$, where one would intuitively expect it, due to the wavefunctions beginning to overlap, but at a later point $D > \zeta(3/2) \approx 2.612^1$. This insight allows us to introduce the critical temperature for a non-interacting three-dimensional gas with no internal degrees of freedom [22]

$$T_C = \frac{2\pi\hbar^2}{m k_B} \left(\frac{n}{\zeta(3/2)} \right)^{2/3} \approx 3.3125 \frac{\hbar^2 n^{2/3}}{m k_B}. \quad (2.1.3)$$

Through further cooling the condensed fraction of particles [22] can be increased, until it reaches unity at zero temperature.

$$\frac{N_{\text{BEC}}}{N_{\text{tot}}} = 1 - \left(\frac{T}{T_C} \right)^3 \quad (2.1.4)$$

Here N_{BEC} denotes the particle number in the ground state in contrast to the whole number of participants N_{tot} .

2.2 Two-body Interactions

As in the ideal case a BEC has zero momentum, its kinetic energy cancels and any weak interaction will play a dominant role. In the following section the most relevant interactions describing a dipolar gas, namely short-range isotropic contact-interaction and long-range anisotropic dipole-dipole-interaction, will be introduced and their quantitative influence on condensate shape and characteristics discussed.

2.2.1 Contact-Interaction

The most basic form of interaction in a Bose-Einstein condensate is the contact interaction. It has its origin in the Van-der-Waals attraction scaling as $-C_6/r^6$ [52] with the element-dependent Van-der-Waals coefficient C_6 and their interparticle distance r .

At smaller distances an electrostatic repulsion, due to an overlap of electron orbitals with an r^{12} -dependence dominates and creates together with the Van-der-Waals interaction a molecular potential, the so called Lennard-Jones potential.

¹ $\zeta(x) = \sum_{k=1}^{\infty} k^{-x}$ is the Riemann zeta function

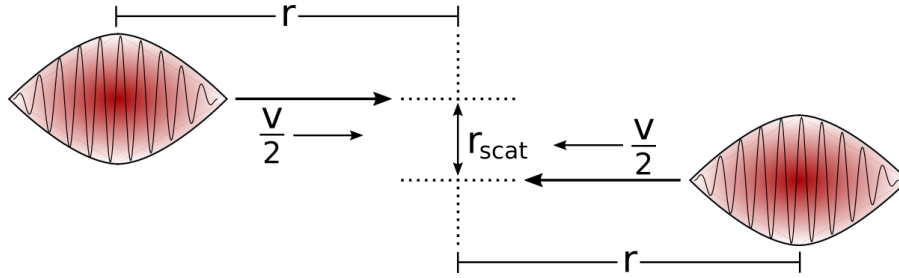


Figure 2: Two colliding quantum mechanical particles with relative velocity v and scattering distance r_{scat} in the center of mass frame

One can show that since the VdW interaction is short-range ($1/r^6$), at low collision energies the only angular momentum is $l = 0$, allowing only spherically symmetric s-waves-scattering. The Van-der-Waals interaction, dictating the long-range behaviour in this potential, exhibits an effective range that can be estimated from the kinetic energy acquired due to the attractive potential [53] of

$$r_{\text{vdW}} = \sqrt[4]{\frac{2mC_6}{\hbar^2}}. \quad (2.2.1)$$

This is in general significantly smaller than the particle's de-Broglie wavelength and can not be resolved effectively. Therefore the exact form of the interaction potential is irrelevant, enabling the replacement by a pseudo-potential with infinitesimal radius [54], that can be written as

$$V_s(r) = g \delta(r) \quad (2.2.2)$$

with the Dirac Delta-distribution $\delta(r)$ and the contact interaction coupling strength

$$g = \frac{4\pi\hbar^2}{m} a_s \quad (2.2.3)$$

where the whole information about the scattering process is now contained in the scattering length a_s (and the mass m), that is positive for repulsive and negative for attractive interactions and can be varied via Feshbach-resonances [25]. While this contact-interaction is present in every Bose-Einstein condensate, another, and due to its anisotropy often more interesting form of inter-particle interaction, can be found if the condensate atoms possess a magnetic moment.

2.2.2 Dipolar interaction

The resulting interaction between particles possessing a magnetic moments is, as opposed to the contact interaction, long-range and anisotropic, allowing the study of a broader variety of phenomena. For a more detailed description of this anisotropic, long-range interaction we want to start with the assumption that all dipoles are aligned in the same direction. In actual experiments this is realised by applying an external magnetic field strong enough

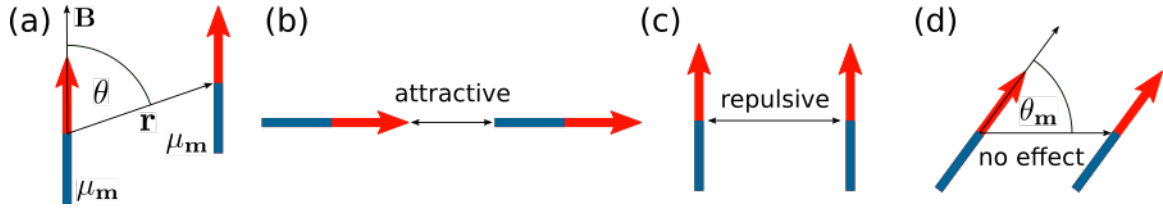


Figure 3: (a) Relative orientation of dipoles inside a dipolar condensate. The two shown dipoles are aligned along the magnetic field direction \mathbf{B} at a distance \mathbf{r} and an angle $\theta = \angle(\mathbf{r}, \mathbf{B})$ to each other. (b),(c) and (d) illustrate the effect of the dipolar interaction in dependence of the dipole orientation. The dipoles attract each other in a head-to-tail configuration (b), repel each other when they are side-by-side (c) and have no effective interaction with each other, if they are tilted by the "magic angle" $\theta_m \approx 54.7^\circ$.

to polarize the whole cloud of atoms. Under such conditions, the interaction potential between two dipoles takes the form [55]

$$V_{dd}(r, \theta) = \frac{\mu_0 \mu_m^2}{4\pi} \frac{1 - 3\cos^2(\theta)}{r^3} \quad (2.2.4)$$

with the relative position between the dipoles described by their distance r , the angle $\theta = \angle(\mathbf{r}, \mathbf{B})$ between the external magnetic field, presetting the dipole polarization direction $\boldsymbol{\mu}$, and the magnetic vacuum permeability μ_0 . The anisotropy enters through the angle θ , resulting in an attractive interaction around $\theta = 0$ or π and a repulsive one around $\theta = \pi/2$ and $3\pi/2$ separated by the so called "magic angle" $\theta_m = \arccos(1/\sqrt{3}) \approx 54.7^\circ$ with a vanishing dipolar interaction potential. The characteristic length scale associated with the dipole-dipole interaction is known as the dipolar length [55]

$$a_{dd} = \frac{\mu_0 \mu_m^2 m}{12\pi \hbar^2} \quad (2.2.5)$$

where the prefactors are chosen such that a dipolar BEC under three-dimensional homogeneous conditions becomes unstable for $a_{dd}/a > 1$ [55]. Likewise, as an equivalent to the contact interaction coupling strength the dipolar coupling strength is introduced:

$$g_{dd} = \frac{4\pi \hbar^2 a_{dd}}{m} = \frac{\mu_0 \mu_m^2}{3} \quad (2.2.6)$$

These definitions allow for an easy comparison between the strengths of the two interaction types through their ratio, the relative dipolar strength

$$\epsilon_{dd} = \frac{g_{dd}}{g} = \frac{a_{dd}}{a_s} = \frac{\mu_0 \mu_m^2 m}{12\pi \hbar^2 a_s}. \quad (2.2.7)$$

The remaining challenge is to describe a realistic Bose-Einstein condensate where both interactions are present. In the following we will refer to such an object as a dipolar BEC

(dBEC). In the limit of weak dipolar interactions the so called "first-order Born approximation" [9] is valid, allowing us to neglect coupling effects between these two interactions and to describe the overall interaction potential as the simple sum of its both constituents.

$$V_{int}(\mathbf{r}) = V_s(\mathbf{r}) + V_{dd}(\mathbf{r}) = g\delta(\mathbf{r}) + \frac{3}{4\pi}g_{dd}\frac{1-3\cos^2(\theta)}{r^3} \quad (2.2.8)$$

In order to observe the dipolar effects clearly and have the condensate's long-range behaviour dominated by the dipole-dipole-interactions, the dipolar interaction length should desirably be of comparable size to the contact interaction $a_{dd} \geq a_s$ or larger.

2.3 Theoretical Description

After taking a look into the process of Bose-Einstein condensation and the relevant interactions, our next step is to discuss the necessary theory to describe such a complex many body system as a Bose-Einstein condensate. Systems consisting of high numbers of interacting particles prove to be quite challenging to describe theoretically without resorting to approximations. In the following we will try to simplify the many-body problem, explore special cases for weak and strong interactions and take a short look into higher order effects.

2.3.1 Mean-field and Extended Gross-Pitaevskii Equation

In order to reasonably describe a high number of interacting particles, a common approximation is to sum the interaction potentials, that a single particle experiences from all its peers, up into a single effective potential. For the beginning we will start with the complete many-body Hamiltonian in second quantization after switching into the Heisenberg representation [22]

$$i\hbar\frac{\partial}{\partial t}\widehat{\Psi}(\mathbf{r},t) = \left[\widehat{\Psi}(\mathbf{r},t), H\right] = \left(-\frac{\hbar^2}{2m}\nabla^2 + V_{ext}(\mathbf{r}) + \int d^3r'\widehat{\Psi}^\dagger(\mathbf{r}',t)V_{int}(\mathbf{r}-\mathbf{r}')\widehat{\Psi}(\mathbf{r}',t)\right)\Psi(\mathbf{r},t) \quad (2.3.1)$$

describing N bosons in an external potential V_{ext} and interacting corresponding to the interaction potential V_{int} from equation (2.2.8), with the normalized boson annihilation and creation operators $\widehat{\Psi}(\mathbf{r})$, $\widehat{\Psi}^\dagger(\mathbf{r})$. This time dependent field operator can be decomposed into a mainly occupied condensate wave function given by the complex number $\Psi = \langle\widehat{\Psi}(\mathbf{r},t)\rangle$ and a perturbation Operator $\delta\widehat{\Phi}$ with vanishing expectation value $\langle\delta\widehat{\Psi}(\mathbf{r},t)\rangle = 0$.

$$\widehat{\Psi}(\mathbf{r},t) = \Phi(\mathbf{r},t) + \delta\widehat{\Psi}(\mathbf{r},t) \quad (2.3.2)$$

In the non-interacting case at zero temperature, all atoms occupy a single state. The approximation we are applying here is that this remains mostly the case, but due to interactions a small perturbation given in the form of the perturbation operator $\delta\widehat{\Psi}(\mathbf{r},t)$

reduces the condensate fraction minimally. At a later stage we will encounter this perturbation again under the name of "quantum fluctuations", but for now it shall be neglected ($\delta\widehat{\Psi}(\mathbf{r}, t) = 0$). Plugging this decomposition into equation (2.3.1) and therefore limiting oneself to work only with the expectation value of the particle wave function is known as "mean-field ansatz" and results in the non-local, time-dependend Gross-Pitaevskii equation, describing the dynamics of a dBEC

$$i\hbar\frac{\partial}{\partial t}\Psi(\mathbf{r}, t) = \left(-\frac{\hbar^2}{2m}\nabla^2 + V_{ext}(\mathbf{r}) + gn(\mathbf{r}, t) + \int d^3r' V_{dd}(\mathbf{r} - \mathbf{r}') n(\mathbf{r}', t) \right) \Psi(\mathbf{r}, t) \quad (2.3.3)$$

including the atomic density $n(\mathbf{r}, t) = |\Psi(\mathbf{r}, t)|^2 = |\sqrt{n(\mathbf{r}, t)} e^{i\phi}|^2$ [22]. Separating the space- and time-dependency in the wavefunction $\Psi(\mathbf{r}, t) = \psi(\mathbf{r}) \exp(-i\mu t/\hbar)$ with the chemical potential μ , allows us to separate off the time-dependency in the Gross-Pitaevskii equation, leading to the stationary GPE useful for investigation of ground state properties

$$\mu\psi(\mathbf{r}) = \left(-\frac{\hbar^2}{2m}\nabla^2 + V_{ext}(\mathbf{r}) + gn(\mathbf{r}) + \int d^3r' V_{dd}(\mathbf{r} - \mathbf{r}')n(\mathbf{r}') \right) \psi(\mathbf{r}) \quad (2.3.4)$$

where the kinetic energy can be identified as the first summand, the external potential as the second, the contact interaction as the third and the dipolar interaction as the last one. Resulting from equation (2.3.4) the corresponding energy functional can be given by [22]

$$E(n, \mathbf{r}) = \int d^3r \left(\frac{\hbar^2}{2m}\nabla^2 + V_{ext}(\mathbf{r}) + \frac{1}{2} \left[gn(\mathbf{r}) + \int d^3r' V_{dd}(\mathbf{r} - \mathbf{r}')n(\mathbf{r}') \right] \right) n(\mathbf{r}) . \quad (2.3.5)$$

Taking into account all interactions for dipolar gases leads to the problem that neither analytical nor semi-analytical solutions of the Gross-Pitaevskii equation can be found, making it necessary to fall back on the study of special cases.

2.3.2 Weak Interaction Limit - Variational Method

One way to bypass the mentioned problem that no exact solutions for the energy-functional (2.3.5) can be found is to use a Gaussian wave function

$$\Psi(\mathbf{r}) = \sqrt{\frac{N}{\pi^{3/2}\sigma_x\sigma_y\sigma_z}} \exp\left(-\frac{x^2}{2\sigma_x^2} - \frac{y^2}{2\sigma_y^2} - \frac{z^2}{2\sigma_z^2}\right) \quad (2.3.6)$$

as an Ansatz and minimize the energy through variation of the lengths $\sigma_{x,y,z}$. This wave function then results in a density distribution that also exhibits a Gaussian form

$$n(\mathbf{r}) = |\Psi(\mathbf{r})|^2 = \frac{N}{\pi^{3/2}\sigma_x\sigma_y\sigma_z} \exp\left(-\frac{x^2}{\sigma_x^2} - \frac{y^2}{\sigma_y^2} - \frac{z^2}{\sigma_z^2}\right) . \quad (2.3.7)$$

The described approximate solution in equation (2.3.7) then represents the exact ground state solution only for non-interacting particles. When increasing the interaction strength the validity of this approach gets worse, but still gives the correct scaling dependencies.

2.3.3 Strong Interaction Limit - Thomas-Fermi Approximation

The other special case we want to discuss is the one of strong inter-particle interactions. Assuming them to exceed the influence of the particle's kinetic energy significantly, the first term in equation (2.3.4) can be neglected, leading to the so called "Thomas-Fermi approximation". At this point we want to limit ourselves to the most relevant results following this approximation and refer for more details to [22]. When neglecting the influence of the kinetic energy the GPE simplifies to

$$\mu\psi(\mathbf{r}) = \left(\frac{m}{2} (\omega_x^2 x^2 + \omega_y^2 y^2 + \omega_z^2 z^2) + gn(\mathbf{r}) + \int d^3r' V_{dd}(\mathbf{r} - \mathbf{r}') n(\mathbf{r}, t) \right) \psi(\mathbf{r}) . \quad (2.3.8)$$

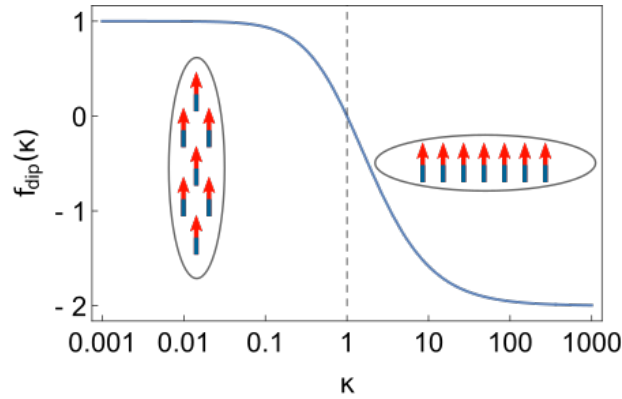


Figure 4: Dipolar anisotropic function f_{dip} depending on the cloud aspect ratio κ . For prolate clouds ($\kappa < 1$), f_{dip} is positive, while it is negative for oblate traps ($\kappa > 1$) and vanishes for spherically symmetric systems.

Through dipolar interactions and consequently resulting anisotropic magnetostriction, the shape of a cloud made of dipolar particles will get deformed. For clarification of a few relevant parameters we want to start with a distinction between the deformation of the trap, in form of the trap aspect ratio $\lambda = \omega_z/\omega_\rho$ (for simplicity we assume identical trap frequencies ω_ρ orthogonal to the magnetic field direction, which shall be, arbitrarily chosen, the z -direction), and the real BEC-cloud-deformation described by the cloud aspect ratio $\kappa = R_\rho/R_z$, for the moment manifested in the ratio of the radii of a purely contact interacting BEC [22]

$$R_{x,y,z}^{\text{contact}} = 15^{1/5} \left(\frac{Na}{\bar{a}} \right)^{1/5} \frac{\bar{\omega}}{\omega_{x,y,z}} \bar{a} . \quad (2.3.9)$$

This represents the radius of a condensate strongly interacting condensate. Such condensates can be shown to exhibit a parabolic density distribution [22].

$$n_{\text{TF}}(\mathbf{r}) = |\psi(\mathbf{r})|^2 = \begin{cases} \frac{15N}{8\pi R_x R_y R_z} \left(1 - \frac{x^2}{R_x^2} - \frac{y^2}{R_y^2} - \frac{z^2}{R_z^2} \right) & \text{for } n_{\text{TF}} > 0 \\ 0 & \text{else} \end{cases} \quad (2.3.10)$$

Under the influence of dipolar interactions the density still holds a parabolic behaviour in every direction, but an anisotropy in the cloud radii arises. The new radii take the form [22]

$$R_\rho = \left[\frac{15N\kappa}{4\pi m\omega_\rho^2} \left(g + g_{\text{dd}} \left[\frac{3}{2} \frac{\kappa^2 f_{\text{dip}}(\kappa)}{1 - \kappa^2} - 1 \right] \right) \right]^{1/5} \quad (2.3.11)$$

$$R_z = \frac{R_\rho}{\kappa} = \left[\frac{15N}{4\pi m\omega_\rho^2 \kappa^4} \left(g + g_{\text{dd}} \left[\frac{3}{2} \frac{\kappa^2 f_{\text{dip}}(\kappa)}{1 - \kappa^2} - 1 \right] \right) \right]^{1/5} \quad (2.3.12)$$

and are now primarily dependent on the strength of the dipolar interaction, as they scale with the dipolar coupling strength g_{dd} and a scaling factor depending on the cloud aspect ratio κ , the dipolar anisotropic function [22]

$$f_{\text{dip}}(\kappa) = \frac{1 + 2\kappa^2}{1 - \kappa^2} - \frac{3\kappa^2 \text{artanh}(\sqrt{1 - \kappa^2})}{(1 - \kappa^2)^{3/2}} \quad (2.3.13)$$

which is a monotonically decreasing function with values ranging from 1 for BECs highly elongated in the magnetic field direction, down to -2 for highly oblate cases (see figure 4). The qualitative reason for a modification of the cloud form under dipolar influences can be illustrated in a very intuitive way. Our BEC, being a physical system, always strives to minimise its energy, resulting in a minimisation of $f_{\text{dip}}(\kappa)$ and therefore κ , leading to an elongation in the field direction, that can be understood through the equivalent of classical dipoles, arranging themselves head-to-tail along an external magnetic field.

2.3.4 Beyond Mean-Field Effects - Quantum Fluctuations

The energy minimisation of the condensate seems to lead inevitably to a collapse of the condensate. Minimising κ should result in an ever increasing density, shrinking the BEC practically to zero volume. In contrast to this, a restabilisation after a first shrinking step of the dBEC, connected to the quantum fluctuations term in equation (2.3.2), leads to a novel state of matter named "Quantum Droplet" [14,15]. Going beyond the previously discussed mean-field approach, Lee, Huang and Yang were able to calculate an additional correction term in order to take the quantum fluctuation term in equation (2.3.2) into account, first only for pure contact interaction [16]. Passing over from pure contact interaction to the consideration of dipolar effects, an extension within the local-density approximation was introduced by Lima and Pelster in 2011 [18]. Following their discussions, the correction-term for the BEC's energy density has the form

$$\frac{E_{\text{QF}}}{V} = \frac{64}{15} g n^2 \sqrt{\frac{n a_s^3}{\pi}} F_5(\epsilon_{\text{dd}}) \quad (2.3.14)$$

with the correction factor

$$F_l(\epsilon_{\text{dd}}) = \frac{1}{2} \int d\theta_k \sin(\theta_k) \sqrt{1 + \epsilon_{\text{dd}} (3 \cos^2(\theta_k) - 1)}. \quad (2.3.15)$$

This energy density correction only plays a relevant role for high densities or strong interaction strengths.

2.3.5 Complete effective GPE

Summarising the effects of all previously discussed interactions, the resulting effective GPE that will be used for the simulations later on in this thesis reads [22]

$$i\hbar \partial_t \Psi(\mathbf{r}, t) = \left[-\frac{\hbar^2 \nabla^2}{2m} + V_{\text{ext}}(\mathbf{r}, t) + g|\psi|^2 + \int V_{\text{dd}}(\mathbf{r} - \mathbf{r}') |\psi(\mathbf{r}')|^2 d\mathbf{r}' + \frac{32g\sqrt{a}}{3\sqrt{\pi}} \left(1 + \frac{3}{2}\epsilon_{\text{dd}}^2\right) |\psi|^3 \right] \Psi(\mathbf{r}, t) \quad (2.3.16)$$

contain influences of the kinetic energy (that shall from now on be called quantum pressure) in the first summand, external potentials in the second, contact interaction in the third, dipolar interactions in the fourth and quantum fluctuations in the last summand.

2.4 Excitations in a dBEC

After building a theoretical foundation for the behaviour of a dipolar Bose-Einstein condensate, we can pass over to possible excitations that can be excited in such a system. These discussions will provide the basis for an understanding of the breakdown of superfluidity in later parts of this thesis.

2.4.1 Speed of Sound in a Homogeneous Dipolar Gas

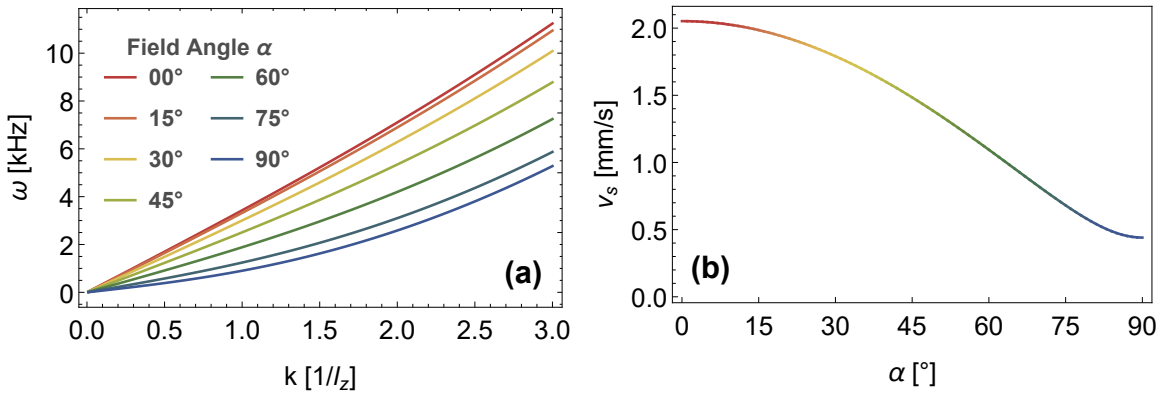


Figure 5: a) Dispersion relation, following equation 2.4.1 for a homogeneous ^{162}Dy condensate with a central atomic density of $n_0 = 2 \cdot 10^{20} \text{ m}^{-3}$. The corresponding parameters are $m = 162 \text{ u}$, $a_s = 140 \text{ a}_0$, $a_{\text{dd}} = 131 \text{ a}_0$ and therefore $\epsilon_{\text{dd}} = 0.873$. b) The speed of sound for the same conditions following equation (2.4.3) as a function of the angle α between magnetization and excitation.

The Bose-Einstein condensates we are working on are trapped and therefore highly complex systems, for whom the exact dispersion relation is unknown. Therefore the a first intuitive approach is to examine the homogeneous three-dimensional case in order to get some basic

insights. The Bogoliubov excitation spectrum for a dipolar homogeneous cloud [40] (shown in figure 5(a)) reads

$$\omega_{\text{hom}}(k, \alpha) = k \sqrt{\frac{\hbar^2 k^2}{4m^2} + \frac{gn_0}{m} [1 + \epsilon_{\text{dd}} (3 \cos^2(\alpha) - 1)]} \quad (2.4.1)$$

where $k = |\mathbf{k}|$ is the absolute value of the wavevector \mathbf{k} and $\alpha = \angle(\mathbf{k}, \mathbf{\mu}_m)$ the angle between \mathbf{k} and the polarization direction $\mathbf{\mu}_m$ (in the case of strong magnetic fields identical to the direction of the magnetic field \mathbf{B}). A closer look at the sum under the square root on the right hand side of equation 2.4.1 reveals two different dependencies on the wavevector k . For high momenta, the dispersion relation is dominated by the first summand, resulting in the well known quadratic dispersion dependence $\omega(k) = \hbar k^2/2m$ of free particles, independent of the angle α and therefore any dipolar influences. On the other hand, in the case of small momenta, with the second summand determining the behaviour, dipolar effects become relevant. Here the dispersion relation scales linearly with the wavevector k , as is a general behaviour of phonons. The dispersion relation allows us to determine the system's sound velocity v_s following

$$v_s(\alpha) = \lim_{k \rightarrow 0} \left(\frac{\omega(k)}{k} \right). \quad (2.4.2)$$

For our homogeneous system described by equation 2.4.1 this takes the form

$$v_{s,\text{hom}}(\alpha) = \sqrt{\frac{gn_0}{m} [1 + \epsilon_{\text{dd}} (3 \cos^2(\alpha) - 1)]} \quad (2.4.3)$$

and is shown in figure 5(b) for the parameters in our Dysprosium BEC, meaning a central density of $n_0 = 2 \cdot 10^{20} m^{-3}$, a mass of $m = 162u$ and a relative dipolar strength of $\epsilon_{\text{dd}} = a_{\text{dd}}/a_s = 131 a_0/140 a_0 = 0.873$. It reveals a velocity maximum for propagation parallel to the external magnetic field ($\alpha = 0^\circ$) and a minimum orthogonal to it ($\alpha = 90^\circ$). That leads to elliptical sound waves depicted in the next section. This behaviour can be understood intuitively in the following way. A density wave propagating through the BEC creates a landscape of alternating planes with either high or low density. If the magnetization direction is parallel to the phonon's wavevector, the microscopic dipoles on the plane, being lifted from the former flat surface, interact repulsively, leading to an increased energy and therefore increased speed of sound. On the other hand, if the dipoles are aligned inside the density planes, it is energetically favourable to align along each other, reducing the overall energy and therefore the speed of sound.

A surprising property of equation (2.4.1), arising from the just discussed phenomenon of energy minimization, is, that the speed of sound in a homogeneous BEC gets imaginary for dipolar interactions exceeding the contact interactions ($\epsilon_{\text{dd}} = g_{\text{dd}}/g \geq 1$). This process is called "phonon instability" and softens the phonon modes into negative energy, leading to a collapse of the BEC [20].

Apart from the creation of sound waves in the homogeneous case, under trapped conditions other excitations can exist and the dispersion relation gets modified. One example thereof is a strong confinement in one direction, allowing the possibility for Roton-creation, a quasi-particle at a finite momentum value. This case is discussed in more detail in section A.1.

It is worth mentioning that in both cases, homogeneous and highly trapped, a description by a continuous dispersion relation is only useful as long as the excitation has a smaller wavelength than the size of the condensate ($k R_{\text{BEC}} \leq 1$).

2.4.2 Anisotropic Speed of Sound

In order to illustrate the anisotropy in the speed of sound following equation (2.4.3) we compare the simulated density profiles of a purely contact-interacting and a dipolar BEC. Therefore simulation results for the relative density distribution $\Delta n(\mathbf{r}, t) = n(\mathbf{r}, t) - n_0(\mathbf{r}, t)$, meaning the difference between the density distribution $n(\mathbf{r}, t)$ at a given time t and the density distribution of the cloud in its energetic ground state in equilibrium $n_0(\mathbf{r}, t)$, are shown in figure 6. The atoms there are initially confined in a small volume and then abruptly released.

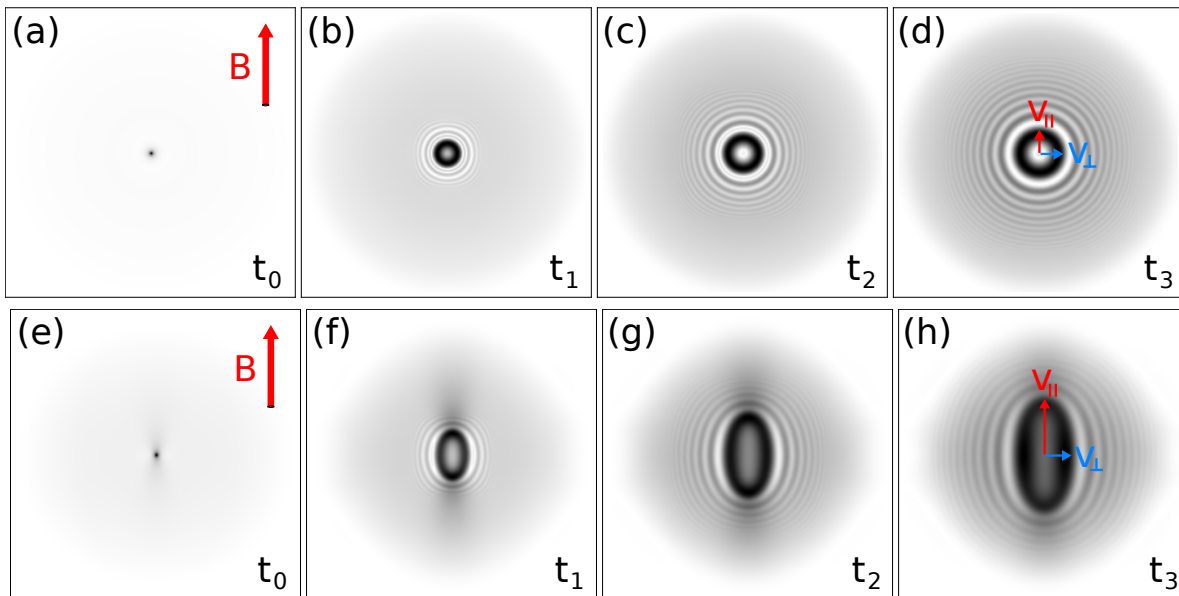


Figure 6: Simulated relative density distribution for the flow of ^{162}Dy -atoms for pure contact interaction ((a)-(d)) and for additional dipole-dipole-interactions ((e)-(f)) after equidistant time steps t_0 to t_3 . The atoms start all trapped in the center of our numerical grid. After releasing they start to flow outward creating density waves, revealing a constant speed of sound in the pure contact-interaction case and a clear anisotropy in favour of the the direction parallel to an external magnetic field under additional dipolar interactions.

In (a)-(d) the situation for pure contact interaction is shown, exhibiting an isotropic speed of sound in both directions. Compared to this in (e)-(h) additional dipole-dipole interactions are implemented, resulting in a significant anisotropy in the systems speed of sound with a drastically increased propagation speed in the direction of an external magnetic field v_{\parallel} and a practically unchanged velocity in the orthogonal direction v_{\perp} .

3 Experimental Setup

In the following chapter a short summary of the experimental procedures necessary to generate the data presented in this thesis will be given. The beginning will be a short introduction to the element Dysprosium and its relevant properties. A short overview of the experimental setup, utilized for the creation of degenerate Dysprosium gases, will be given, and we will finish with a description of the electro-optical deflector system (EOD) used for the creation of time-varying optical potentials in the form of a Gaussian laser beam moving inside of the BEC.

3.1 Dysprosium

The element used in this work is Dysprosium, a rare-earth element in the lanthanide group with 66 protons and electrons. It possesses a relatively high melting (1412 °C) and boiling point (2567 °C), as well as seven stable isotopes of which four are naturally occurring in significant proportion. Of these, ^{162}Dy (25.5%) and ^{164}Dy (28.3%) are bosonic, while ^{161}Dy (18.9%) and ^{163}Dy (24.9%) are fermionic [30].

These fermionic isotopes feature a nuclear spin of $I = 5/2$, resulting in a splitting into six hyperfine states, ranging from $F = 11/2$ to $F = 21/2$, while their bosonic counterparts miss any sort of hyperfine splitting. The 66 electrons result in an electronic ground state configuration of $[\text{Xe}]4f^{10}6s^2$, describing a partly filled 4f shell with and a closed 6s shell. These four missing electrons in the 4f shell, lead to an orbital angular momentum of $L = 6$ and total electronic spin of $S = 2$, resulting in a total angular momentum of $J = 8$.

This unusual high angular momentum is responsible for Dysprosiums high magnetic moment of $\mu_m = 9.93 \mu_B$, with the Bohr magneton μ_B , making it, together with Terbium, the element with the highest magnetic moment in the periodic system of elements. This magnetic moment, together with the mass of the ^{162}Dy isotope $m_{162} = 161.92 \text{ a.u.}$, where u describes the unified atomic mass unit results in a significant dipolar length. Following equation [2.2.5] it takes the value $a_{\text{dd}}^{\text{Dy}} = 131 a_0$, with the Bohr radius a_0 . The background s-wave scattering length a_s differs significantly for the two bosonic isotopes used in the course of this work, taking values of $a_{s,164} = 69(4) a_0$ [31] and $a_{s,162} = 141(17) a_0$ [35].

Following the discussions in chapter 2.2.2, a dipolar BEC is stable for $\epsilon_{\text{dd}} = a_{\text{dd}}/a_s < 1$.

While this is usually (apart from regions very close to Feshbach resonances) fulfilled for the ^{162}Dy -isotope, ^{164}Dy -condensates are stable only for increased scattering lengths, for example near Feshbach resonances. A second and experimentally better accessible way to increase stability is an adaptation of the trapping conditions. Due to anisotropy in the interactions, the clouds density distribution influences the systems robustness, allowing changes of the stability threshold through variations of the trap aspect ratio [32,48].

3.2 Creation of Dysprosium BECs

In the following a short overview of the experimental setup and the steps necessary to create a degenerate gas of Dysprosium shall be given. The atoms path through the three parts of the vacuum chamber, from the oven chamber over the MOT chamber to the glass cell, where they will end as a Bose-Einstein condensate. For a more detailed description of the whole process, we refer to the Ph.D. theses of Thomas Maier [33] and Holger Kadau [20].

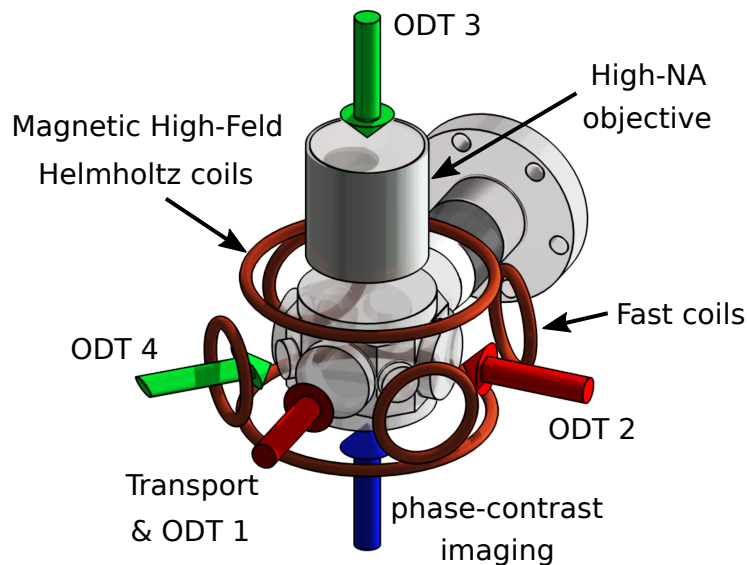


Figure 7: A scheme of the glass cell, that the atoms enter from the MOT via a transport beam. They are trapped in a crossed optical dipole trap (cODT) created by the laser beams ODT1 and ODT2. Possible imaging paths are time-of-flight absorption imaging from the side, as well as high-resolution insitu phase-contrast imaging in the vertical direction. Parallel to this a beam (ODT3) of an electro-optical deflector (EOD) system passes the high-numerical aperture objective, enabling the creation of time-dependent optical potentials. A light sheet (ODT4), representing a highly flattened laser beam, can be used to further manipulate the trapping conditions of the condensate. Magnetic field coils around the glass cell provide homogeneous as well as a controlled gradient magnetic fields, influencing properties of the trapped atoms.

From solid to gas

The utilized Dysprosium begins as a solid, in the form of a high-purity granulate (99.9 %) inside a molybdenum crucible in an effusion cell. This cell is localised inside of the vacuum system in the oven chamber, where our Dysprosium is heated up to temperatures of $T \approx 1250^\circ\text{C}$ under a pressure of $p \approx 10^{-9}$ mbar.

These conditions are sufficient for sublimation, allowing the atoms to leave the crucible through a small aperture. The atoms are cooled in the transverse direction through a transversed cooling scheme, using red-detuned light of the broad 421 nm transition. In the longitudinal direction the atoms possess a mean velocity of around 450 m/s, significantly too quick for trapping inside of a magneto-optical trap. Therefore we use a spin-flip Zeeman slower, also working on the 421 nm transition. This results in the atoms begin decelerated

to around 10 m/s, slow enough to allow trapping in a magneto-optical trap.

Cooling in a magneto-optical trap (MOT)

After leaving the Zeeman-slower, the atoms arrive in the MOT-chamber where they are captured in a narrow-line magneto-optical trap working at 626 nm with a linewidth of $\gamma_{626} \approx 136$ kHz. The chosen wavelength results in a red-detuning of the MOT lasers, A large beam diameter of 22.5 mm and consequently a high intensity of $250 I_{\text{sat},626}$ is chosen in order to trap as many atoms as possible. An additional spectral broadener is used to increase the laser linewidth, increasing the velocity range where trapping is possible. In the end, loading of around $8 \cdot 10^7$ atoms of ^{162}Dy at a central detuning of $35 \gamma_{626}$, at around $500 \mu\text{K}$, is possible. The final cooling step in the MOT consists of reducing the detuning to $5 \gamma_{626}$ and the intensity to $0.24 I_{\text{sat},626}$, lowering the temperature to $\approx 10 \mu\text{K}$, low enough to load them in an optical trap.

Transport to the glass cell

In order to transport the atoms from the MOT to the glass cell, we use a focused broadband fiber laser at 1070 nm. We focus the laser down to a beam waist of $\approx 40 \mu\text{m}$ with a maximum power of ≈ 72 W, producing a potential trap depth of $\approx 640 \mu\text{K}$. The transportation is carried out by moving the laser focus, where the atoms are primarily trapped, from the MOT to the glass cell. Therefore the last focussing lens of the transport beam is positioned on a translation-stage.

Our MOT, even after compressing, still has a Gaussian width of around $400 \mu\text{m}$, significantly bigger than the beam waist of the transport laser. In order to load as many atoms as possible, the overlap between the MOT and the transport beam should be optimized, therefore we position the mounted lens around 15 mm away from the MOT position, where the trapping area is 18-fold increased, but therefore the trapping depth reduced by the same amount. We deactivate the MOT, after superimposing it with the transport beam, thereby trapping the atoms purely in the optical tweezer. The focus is now moved to the atom position in 47 ms and subsequently to the glass cell within another 1.2 s over a distance of 37.5 cm. This procedure usually results in $\approx 10^7$ atoms with a mean temperature of $120 \mu\text{K}$ ending up in the glass cell.

Crossed optical dipole trap (cODT)

After entering the glass cell, the atoms are transferred into a crossed optical dipole trap, consistint of two laser beams ODT1 and ODT2, intersecting at an angle of 90° , both produced by a 1064 nm solid-state-laser with a power of 55 W. ODT1, being superimposed with the transport beam, is radially symmetric with a beam waist of $\approx 40 \mu\text{m}$ and a power of up to 12 W, while ODT2 has an elliptical shape with waists of $\approx 120 \mu\text{m}$ and $\approx 30 \mu\text{m}$ in horizontal and vertical direction.

Inside of the crossed dipole trap, the atoms are cooled with an orange 626 nm laser to increase the population in the crossed trap region. Up to $5 \cdot 10^5$ atoms with a temperature of about $20 \mu\text{K}$ can be trapped in the crossed ODT this way, with around five times that number still remaining in ODT1.

Forced evaporation to degeneracy

Degeneracy is achieved from here on through forced evaporative cooling. The idea behind this method is to remove the hottest atoms out of the gas by lowering the potential depth of the traps further and further. If this is done slow enough, the remaining atoms can rethermalize through two-body collisions, effectively reducing the mean temperature of the remaining particles. In this way, by reducing the intensity of the trap beams and thereby the potential depth, over around 4.5s, we end up with a Bose-Einstein condensate of up to 50.000 ^{162}Dy atoms with a mean temperature of 50 nK.

3.3 Time-Averaged Potentials by an Electro-Optical Deflector (EOD)

In the following a short introduction to the electro-optical deflector (EOD) system, that is used to create a time-dependent optical potential inside our Dysprosium condensate shall be given.

For a more detailed description of the system and the theory behind it, the master thesis of Matthias Wenzel [34] can be consulted.

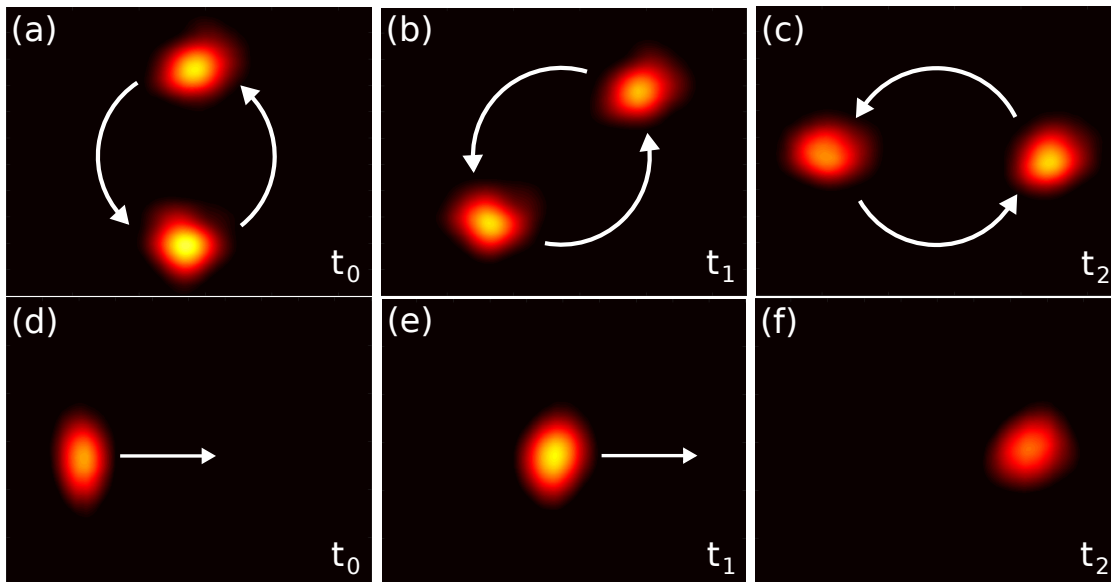


Figure 8: Intensity patterns of the ODT3 beam for different configurations of the EOD system are shown, taken with a CCD-Camera. In (a) two laser beam spots with Gaussian intensity distribution are created equidistantly to their center. At $t_1 > t_0$ (b) and $t_2 > t_1$ (c) the beam position is shown when rotating the potential pattern with a constant velocity. This configuration can be used to create vortex patterns inside the BEC. (d)-(f) show a linear stirring procedure, where the laser beam is moved in the horizontal direction from position (d) over (e) (at t_1) to position (f) (at t_2), usable for measurements of the critical velocity of the system, as shall be discussed in later parts of this work.

The EOD system used for the work in this thesis is presented in figure 9. It consists of a laser beam, passing a Pockels cell, able to vary the laser power, and two orthogonal reflectors, to manipulate the beams propagation direction.

We choose one power stabilized laser-system with a wavelength of 532 nm (figure 9(a)),

enabling the creation of attractive potentials for the Dysprosium atoms.

The choice of this wavelength is motivated by Dysprosium possessing a higher polarizability for 532 nm than for 1064 nm used in the dipole traps, enabling smaller spot sizes following the Abbe diffraction-limit.

A further 405 nm laser diode-system has been implemented and aligned during the course of this thesis (see figure 9(b)) for the purpose of allowing the creation of repulsive potentials as well.

These two beams are coupled into optical fibers and brought together onto the same optical table. The beams are overlapped (figure 9(c)) with a dichroic mirror, transmitting the green and reflecting the blue light. After that a part of the intensity is coupled into a photo diode in order to stabilize the laser power using either the AOM in (a) or (b).

The light then passes a Pockels cell that allows to precisely manipulate the polarization direction, enabling together with a following polarizer in the deflector system to tune the transmitted beam power very fast.

After the Pockels cell, the light arrives at the deflector-system, containing two orthogonal deflectors for moving the beam in horizontal and vertical direction, building the core of the whole EOD-apparatus.

In detail these deflectors consist of crystals that vary the deflection angle of passing light in dependence of an applied voltage. Therefore through variation of the voltage the beam position can be varied between defined positions $\mathbf{r}_i = (x_i, y_i)$ with a fixed frequency f_{scan} . The desired potential can now be designed by the correct selection of the iteration positions, moving for a time t_{move} between them, and holding at each spot for times t_{hold} .

An example for the potentials used in this thesis is shown in figure [8] where an example for linear as well as circular stirring is shown.

The desired potential would get blurred out if the time necessary to switch between the aspired positions is in the same order as the hold time on these spots ($t_{\text{move}} \approx t_{\text{hold}}$), due to the significant intensity contributions between them. However the Pockels cell functions as a sort of shutter, allowing us to turn down the laser intensity during the moving intervalls and turning it up again during the hold times, enabling us to create more detailed potential landscapes.

This whole procedure is controlled by the real-time processing system "ADwin Gold II". The corresponding code for the linear and circular stirring procedures shown in figure [8], written in Adbasic with a LabView interface, was implemented as part of this thesis.

The trap depth at the spots for a non-moving beam can be calculated to

$$V_{\text{stirrer}}^{532 \text{ nm}} = \frac{\text{Re}[\alpha]P}{\epsilon_0 \pi c w_0^2} = -27.3 \mu\text{K} \quad (3.3.1)$$

with the real part of the polarizability $\text{Re}[\alpha]$, calculated to be 429 a.u. for green light, the laser power P , typically $\approx 1 \mu\text{W}$ in our experiments, the vacuum permittivity ϵ_0 , the speed of light c and the beam waist w_0 estimated to be around $1.5 \mu\text{m}$.

Due to the fact that our EOD-beam is approximately parallel to the gravitational direction z , an additional gravitational potential $V_{\text{grav}} = mgz$ acts on the condensate particles, slightly reducing the resulting potential depth.

The time-averaged potential depth $V_{\text{stirrer}}(\mathbf{r})$ at any position is determined by the laser power, the hold duration at the respective position and how frequently it is passed.

When passing the deflector system, both beams (green and blue) enter the first deflector correctly linear polarized and therefore both get deflected identically. Problematic about the implementation of the additional 405 nm beam is that the waveplate inside the deflector system is optimized for 532 nm and therefore rotates the polarization of the blue light incompletely.

Therefore when entering the second deflector only the green light is correctly polarized, and gets deflected as expected, while a part of the blue beam, that did not obtain the correct polarization, passes undeflected.

A polarizer for blue light prevents the transmission of this undesired beam parts. In the end both beams are deflected in the desired way, whereby losses in the blue intensity have to be accepted due to the filtering of the undeflected parts.

In fact that does not pose a significant problem, for we only need a few milliwatt of stirrer power for our experiment. To reduce the power of the two beams accordingly we add several optical attenuators before the beam is significantly widened through a 7.5:1 telescope and focused into the glass cell through a 25 mm objective.

It is worth mentioning that, even though the double-pass-AOM system for the 405 nm laser diode was build and fully aligned during the course of this thesis, it did not produce any experimental data used in the analysis following in later chapters.

The main reason behind this is that the sign of the potential (negative for 532 nm and positive for 405 nm light) has negligible influence on the critical velocity of a superfluid system, while it is of significant importance for vortex creation [37].

For its irrelevance all the critical velocity measurements have been performed with the green laser beam.

The implemented 405 nm beam path has not been used beyond testing and aligning during this thesis, but will surely find its reason for being in future ground-breaking work like the creation of vortices out of dipolar materials.

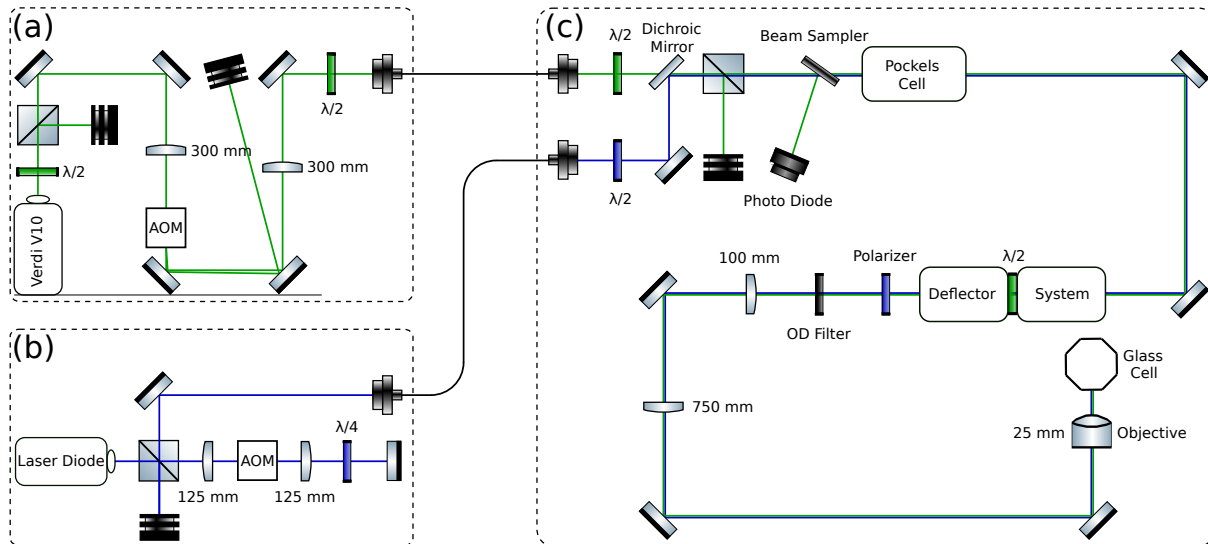


Figure 9: The EOD system with its respective beam paths is shown. (a) A Verdi V10 generates 532 nm laser light, that is power stabilized by an AOM and coupled into a fiber. (b) 405 nm light is produced by a laser diode, providing us with up to 150 nW. The power is stabilized by a double-pass-AOM system before coupling into an optical fiber. (c) After coupling out, both laser beams are overlapped by a dichroic mirror, transmitting the green and reflecting the blue light. A small fraction of the incoming intensity is coupled into a photo diode, for stabilising the laser power through the AOMs in (a) and (b). The beam then passes a Pockels cell, allowing to turn the beam power on and off as desired. Subsequently the laser passes the deflector system, where its direction can be manipulated. Finally the polarization of the 405 nm-beam gets linearized again and the power reduced to a few OD filter before the beam gets widened through a 7.5:1 telescope and guided to the 25 mm objective where it is focused into the glass cell.

4 Numerical Simulation Methods

Superfluid phenomena, like the critical velocity, are highly dependent on numerous distinct parameters from interaction mechanisms over trapping conditions to stirrer properties, making a satisfying analytical description unaccessible and creating the necessity for extensive numerical simulations in order to achieve a theoretical understanding of the processes.

4.1 Simulated Stirring Characteristics

For our analysis we perform numerical simulations on the extended Gross-Pitaevskii equation (eGPE)

$$\begin{aligned}
 i\hbar \partial_t \Psi(\mathbf{r}, t) &= \left[\hat{H}_{\text{QP}} + \hat{H}_{\text{ext}} + \hat{H}_{\text{con}} + \hat{H}_{\text{dip}} + \hat{H}_{\text{QF}} \right] \Psi(\mathbf{r}, t) \\
 &= \left[-\frac{\hbar^2 \nabla^2}{2m} + V_{\text{ext}}(\mathbf{r}, t) + g|\psi|^2 \right. \\
 &\quad \left. + \int V_{\text{dd}}(\mathbf{r} - \mathbf{r}') |\psi(\mathbf{r}')|^2 d\mathbf{r}' + \frac{32g\sqrt{a}}{3\sqrt{\pi}} \left(1 + \frac{3}{2}\epsilon_{\text{dd}}^2 \right) |\psi|^3 \right] \Psi(\mathbf{r}, t)
 \end{aligned} \tag{4.1.1}$$

containing the hamiltonians for quantum pressure \hat{H}_{QP} , external potential \hat{H}_{ext} , contact interaction \hat{H}_{con} , dipolar interaction \hat{H}_{dip} and quantum fluctuations \hat{H}_{QF} on a rectangular-shaped three-dimensional lattice with 128-512 grid. The external potential V_{ext} contains a time-independent harmonic trapping potential, reflecting the influence of dipole traps, and an attractive potential attributed to the stirring laser beam

$$V_{\text{ext}}(\mathbf{r}, t) = V_{\text{trap}}(\mathbf{r}) + V_{\text{stirrer}}(\mathbf{r}, t) \tag{4.1.2}$$

where the latter was chosen to possess a gaussian energy distribution in accordance with a gaussian laser beam profile in the experiment. It is movable in the plane with velocity \mathbf{v} (the projection in x-direction shall be denoted v_x and in y-direction v_y) in any desired direction.

$$V_{\text{stirrer}}(\mathbf{r}, t) = -\underbrace{\frac{Re[\alpha]P}{\epsilon_0 \pi c w_0^2}}_{V_0} \cdot \frac{1}{1 + \left(\frac{z}{z_R}\right)^2} \cdot \exp \left[-\frac{2(x - v_x t)^2 + 2(y - v_y t)^2}{w_0^2 \left(1 + \left(\frac{z}{z_R}\right)^2\right)} \right]. \tag{4.1.3}$$

Here z_R denotes the Rayleigh length $z_R = \pi w_0^2 / \lambda$, w_0 the beam waist, P the laser power and α the polarizability of our isotope Dy^{162} at a laser wavelength of 532 nm. Striving for conformance with the experimental conditions we typically choose a beam waist of 1.5 m , a laser power of 1 m and calculated the polarizability to be $Re[\alpha] \approx 429 \text{ a.u.}$.

4.2 Mathematical and Numerical Tools

Before discussing these simulation procedures in detail, it seems necessary to look into the utilized mathematical tools first. The simulation mechanism described in the following is based on the work of David Peter during his Master Thesis [38] and has been optimized further through the implementation of the Crank-Nicolson Method [39] to calculate derivatives faster and with higher numerical stability.

4.2.1 Split-step method

The time-evolution of a quantum mechanical wave function in the case of a time-independent Hamiltonian $[\hat{H}(t), \hat{H}(t')] = 0$ is well known to be given by

$$\Psi(t + \Delta t) = \exp\left(-\frac{i}{\hbar}\hat{H}\Delta t\right)\Psi(t) \quad (4.2.1)$$

for small time steps Δt . As the different energy contributions are independent of each other, we can decompose the Hamilton operator

$$\hat{H} = \hat{H}_{\text{QP}} + \hat{H}_{\text{ext}} + \hat{H}_{\text{con}} + \hat{H}_{\text{dip}} + \hat{H}_{\text{QF}} . \quad (4.2.2)$$

Plugging this decomposition into the time-evolution (4.2.1) we have to apply the Baker-Campbell-Hausdorff formula treating the sum of operators in an exponent

$$e^{(X+Y)\Delta t} = e^{X\Delta t} \cdot e^{Y\Delta t} \cdot e^{-\frac{1}{2}[X,Y]\Delta t^2} \quad (4.2.3)$$

where the latest factor holds some unpleasant complications for our calculations. Since the eigensystem of the quantum pressure Hamiltonian is the momentum space in contrast to real space for all the others, these contributions do not commute, forcing us to take a closer look at the commutation factor. The fact that its exponent scales quadratically with the size of the time-step Δt compared to the linear scaling of the other exponents, allows us to neglect it for small enough time-steps, resulting in a pure multiplication of the different energy contributions

$$e^{-\frac{i}{\hbar}\hat{H}\Delta t} = e^{-\frac{i}{\hbar}\hat{H}_{\text{QP}}\Delta t} \cdot e^{-\frac{i}{\hbar}\hat{H}_{\text{ext}}\Delta t} \cdot e^{-\frac{i}{\hbar}\hat{H}_{\text{con}}\Delta t} \cdot e^{-\frac{i}{\hbar}\hat{H}_{\text{dip}}\Delta t} \cdot e^{-\frac{i}{\hbar}\hat{H}_{\text{QF}}\Delta t} . \quad (4.2.4)$$

This reduces the calculation costs drastically, to the expense of the necessity for a higher number of time-steps. The main problem occurring from this procedure is the possibility for numerical instability, due to the second order spatical derivatives contained in the quantum pressure Hamiltonian. In order to counteract this tendency, a new numerical scheme was implemented for the time-evolution of the quantum pressure in our system.

4.2.2 Crank-Nicolson Scheme

Trying to find numerical solutions for a differential equation describing a quantum mechanical system can be challenging, as the corresponding Hamiltonians often contain derivatives, possibly leading to numerical instabilities when using basic methods as for example the regular Split-Step Method discussed above.

$$i\hbar \partial_t \Psi = \hat{H} \Psi \quad \Rightarrow \quad \partial_t \Psi = -\frac{i}{\hbar} \hat{H} (x, y, z, \partial_x^2, \partial_y^2, \partial_z^2) \Psi \quad (4.2.5)$$

The Crank-Nicolson Scheme provides a numerically stable method to deal with these derivatives. First splitting up the Hamiltonian into a part without any derivatives \hat{H}_{stat} and parts containing them \hat{H}_{dyn}^i will allow for a significant simplification of the problem.

$$\hat{H} = \hat{H}_{\text{stat}} + \sum_i \hat{H}_{\text{dyn}}^i \quad (4.2.6)$$

The basic idea is to solve the static and the dynamic parts after another, starting without the derivatives.

$$\Psi_i^{n+1/2} = \hat{H}_{\text{stat}} \Psi_i^n = e^{-i\Delta t \hat{H}_{\text{stat}}} \Psi_i^n \quad (4.2.7)$$

Here i denotes the spacial position on the quantized grid, Δt describes the duration of a time step and n the number of the time step with $n + 1/2$ clarifying that our new wavefunction describes only an intermediate step on the way to the final result for the next time step Ψ^{n+1} .

Working on a numerical grid with discrete timesteps and grid spacings, derivatives on a function Ψ_i^n are applied in the form of difference quotients

$$\partial_r \Psi_i^n = \frac{\Psi_{i+1}^n - \Psi_i^n}{\Delta r} \quad ; \quad \partial_r^2 \Psi_i^n = \frac{\Psi_{i+1}^n - 2\Psi_i^n + \Psi_{i-1}^n}{(\Delta r)^2} \quad (4.2.8)$$

$$\partial_t \Psi_i^n = \frac{\Psi_i^{n+1} - \Psi_i^n}{\Delta t} \quad ; \quad \partial_t^2 \Psi_i^n = \frac{\Psi_i^{n+1} - 2\Psi_i^n + \Psi_i^{n-1}}{(\Delta t)^2} \quad (4.2.9)$$

with the distance between neighbouring spatial lattice points Δr . With this the propagation due to one of the dynamic Hamiltonians can be given by

$$\frac{\Psi_i^{n+1} - \Psi_i^{n+1/2}}{\Delta t} = \frac{i}{2\hbar} \hat{H}_{\text{dyn}} (\Psi_i^{n+1} + \Psi_i^{n+1/2}) \quad (4.2.10)$$

where on the right side the mean value of Ψ^{n+1} and $\Psi^{n+1/2}$ was chosen, equivalent to the mean of applying a forward Euler method at time $n + 1/2$ and a backward Euler method at time $n + 1$. Assuming that \hat{H}_{dyn} consists of a second derivative in space, as it will be the case for the quantum pressure term, our result following equation [4.2.8], takes the form

$$\frac{\Psi_i^{n+1} - \Psi_i^{n+1/2}}{\Delta t} = \frac{i}{2\hbar(\Delta r)^2} \left[(\Psi_{i+1}^{n+1} - 2\Psi_i^{n+1} + \Psi_{i-1}^{n+1}) + (\Psi_{i+1}^{n+1/2} - 2\Psi_i^{n+1/2} + \Psi_{i-1}^{n+1/2}) \right] . \quad (4.2.11)$$

We end with this intrinsic equation, containing the known wavefunctions $\Psi_{i+1}^{n+1/2}$, $\Psi_i^{n+1/2}$, $\Psi_{i-1}^{n+1/2}$ at time $n + 1/2$ and the unknown wavefunctions Ψ_{i+1}^{n+1} , Ψ_i^{n+1} , Ψ_{i-1}^{n+1} at time $n + 1$. Choosing the desired boundary conditions, in our case the vanishing of the wavefunction on the borders of our grid ($\lim_{i \rightarrow 0} \Psi_i^n = 0$ and $\lim_{i \rightarrow i_{max}} \Psi_i^n = 0$ with i_{max} the grid length), describing closed boundary conditions, this equation posses a unique solution for the wavefunctions Ψ_i^{n+1} and $\Psi_{i \pm 1}^{n+1}$.

Should the original Hamiltonian contain more than one term with derivatives, than steps 4.2.10 or situationally 4.2.11 have to be repeated for every one of them. Executing this procedure on every grid point finishes one step of the time-evolution and the whole procedure can be repeated for every desired number of time-steps.

4.2.3 Real Time Evolution

In the following the time evolution due to the different energy contributions given by the individual terms in equation [4.2.4] shall be discussed. The four evolution steps from the wavefunction at time t to $t + \Delta t$ are implemented in the following order.

$$\Psi(\mathbf{r}, t) \xrightarrow{\hat{H}_{con}} \Psi_1(\mathbf{r}) \xrightarrow{\hat{H}_{dip}} \Psi_2(\mathbf{r}) \xrightarrow{\hat{H}_{QP}} \Psi_3(\mathbf{r}) \xrightarrow{\hat{H}_{QF}} \Psi_4(\mathbf{r}) \xrightarrow{\hat{H}_{ext}} \Psi(\mathbf{r}, t + \Delta t) \quad (4.2.12)$$

Contact interaction

The influence of contact interaction on the wavefunction can be described by the standard time-evolution for time-independent Hamiltonians (4.2.1) with the contact interaction Hamiltonian

$$\Psi_1(\mathbf{r}) = \exp\left(-\frac{i}{\hbar} gN |\Psi(\mathbf{r})|^2 \Delta t\right) \Psi(\mathbf{r}, t) . \quad (4.2.13)$$

Dipolar interaction

To simplify the calculation with the density integral of the dipolar part, it seems advisable to switch to Fourier space, where one takes advantage of the convolution theorem, making it take the form of a simple multiplication

$$\mathcal{F}\{\Phi_{dd}\} = \mathcal{F}\{V_{dd} * n\} = (2\pi)^{3/2} \cdot \mathcal{F}\{V_{dd}\} \cdot \mathcal{F}[n] . \quad (4.2.14)$$

Thereby the evolution can be conducted by using the Fourier-transformation \mathcal{F} and the corresponding back-transformation \mathcal{F}^{-1}

$$\begin{aligned} \Psi_2(\mathbf{r}) &= \exp\left(-\frac{i}{\hbar} \cdot \mathcal{F}^{-1}\left\{(2\pi)^{3/2} \cdot \mathcal{F}\{V_{dd}\} \cdot \mathcal{F}\{|\Psi_1|^2\}\right\}\right) \Psi_1(\mathbf{r}) \\ &= \exp\left(+\frac{i}{\hbar} \cdot g_{dd} N \mathcal{F}^{-1}\left\{(1 - 3 \cos^2(\alpha)) \cdot \mathcal{F}\{|\Psi_1|^2\}\right\} \Delta t\right) \Psi_1(\mathbf{r}) . \end{aligned} \quad (4.2.15)$$

Quantum Pressure

The quantum pressure term represents the biggest challenge in our whole procedure, due to the contained derivatives. The term itself takes the well known form

$$\hat{H}_{\text{QP}} = -\frac{\hbar^2}{2m}\nabla^2 = -\frac{\hbar^2}{2m}\frac{\partial^2}{\partial x^2} - \frac{\hbar^2}{2m}\frac{\partial^2}{\partial y^2} - \frac{\hbar^2}{2m}\frac{\partial^2}{\partial z^2} = \hat{H}_{\text{QP},x} + \hat{H}_{\text{QP},y} + \hat{H}_{\text{QP},z} . \quad (4.2.16)$$

Segmenting the Hamiltonian into three different parts with only derivatives in a single direction left, the Crank-Nicolson scheme, introduced in section [4.2.2], can be used to calculate this time-evolution in a numerically stable way.

Quantum Fluctuations

The Hamiltonian for quantum fluctuations does not contain derivatives and can therefore be calculated straight forward [18] by

$$\Psi_4(\mathbf{r}) = \exp\left(-\frac{i}{\hbar}\hat{H}_{\text{QF}}\Delta t\right)\Psi_3(\mathbf{r}) = \exp\left(-\frac{i}{\hbar}\cdot\frac{32}{2}gn\sqrt{\frac{na_s^3}{\pi}}F_5(\epsilon_{\text{dd}})\cdot\Delta t\right)\Psi_3(\mathbf{r}) \quad (4.2.17)$$

with F_5 given according to equation [2.3.15].

External potential

Similar to the contact interaction term, the calculation in real space enables the representation of the time-evolution by a pure multiplication

$$\Psi(\mathbf{r}, t + \Delta t) = \exp\left(-\frac{i}{\hbar}\cdot V(\mathbf{r})\cdot\Delta t\right)\Psi_4(\mathbf{r}) . \quad (4.2.18)$$

Here it is worth mentioning, that, for cases with activated stirring laser, the potential $V(\mathbf{r})$ is time-dependent, violating the requirements for usage of evolution [4.2.1], that is only valid for time-independent Hamiltonians. In fact, with the stirring velocities we are using, even a single oscillation contains several thousand time-steps, making the potential on a step-to-step basis practically constant, justifying the usage of this simplified evolution-mechanism.

4.2.4 Imaginary Time Evolution

Before performing real-time evolution steps, the starting step for all of our simulations is to find the ground state of the condensate under the chosen conditions, meaning especially

the chosen trapping conditions. We determine this ground state by solving the extended Gross-Pitaevskii equation [2.3.3] using the imaginary time evolution method [28]. The idea behind the imaginary time evolution is to replace the time t by an imaginary equivalent $\tau = -it$

$$\Psi(\tau + \Delta\tau) = \exp\left(-\frac{1}{\hbar}\hat{H}\Delta t\right)\Psi(\tau). \quad (4.2.19)$$

It is worth noting that this breaks the normalization, making it necessary to normalize again after every time step in order to ensure numerical stability. Decomposing the wavefunction Ψ into ground state Ψ_{GS} and excited part $\delta\Psi$, as well as assuming the ground state energy to be zero $\hat{H}\Psi_{\text{GS}} = 0$ results in

$$\Psi(\tau + \Delta\tau) = \Psi_{\text{GS}} + \exp\left(-\frac{1}{\hbar}\hat{H}\Delta t\right)\delta\Psi(\tau). \quad (4.2.20)$$

Choosing a vanishing ground state energy has the advantage that only positive eigenvalues are left, creating an exponential decay of the excited part $\delta\Psi$ for successive evolution steps and a convergence to the ground state wave function Ψ_{GS} .

4.3 Explicit Stirring Procedures

After reviewing the important mathematical tools we have formed the basis for a closer look at the simulation schemes for linear and circular beam stirring, that will be generating the results shown in the rest of this thesis.

4.3.1 Linear Stirring

Most of this thesis covers the investigation of anisotropy in the critical velocity, as will be further discussed in chapter [5], leading us to stir linearly in different directions with the Gaussian laser beam described in [4.1.3].

Figure 10 shows the simulated cloud at relevant times during the stirring procedure. We start with N atoms following a Gaussian density distribution with widths $\sigma_{x,y,z}$, that are chosen either by an educated guess or according to previous results under similar conditions, in a harmonic trapping potential $V_{\text{trap}}(\mathbf{r})$ without a stirrer $V_{\text{stirrer}}(\mathbf{r}, t) = 0$ (a). Then the ground state is found using imaginary time evolution of the eGPE (4.1.1) using the split-step method and the Crank-Nicolson scheme for the derivatives for an activated stirring laser in the center (b). After getting into the ground state, we perform one oscillation with the stirrer potential, moving it with a constant velocity \mathbf{v} from the center in the desired direction over a distance r_{max} (c), then back in the opposite direction for $2 r_{\text{max}}$ (d) and back to the center over another r_{max} . An additional free evolution time can be added at this point to investigate the behaviour of different formed density waves (e), whereby no additional heating takes place. We determine the induced heating $\Delta E_1 = E_{\text{tot}}^f - E_{\text{tot}}^i$ by comparing the system's total energy before (E_{tot}^i) and after (E_{tot}^f) the stirring.

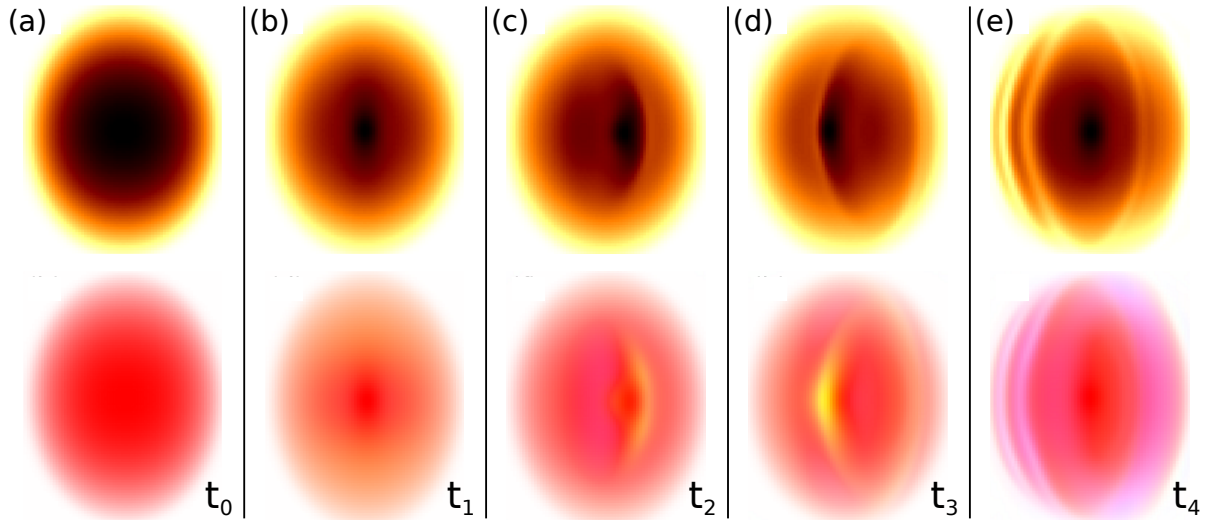


Figure 10: Density (upper row) and phase (lower row) of the simulated cloud, trapped under radially symmetric conditions with trap frequencies $f_{x,y} = 50$ Hz and $f_z = 168$ Hz, are shown at different times during the course of a linear stirring procedure at 1.5 m/s, significantly above the critical velocity. (a) shows the initial cloud condition with a Gaussian density distribution around the cloud center. (b) represents the energetic ground state with activated stirrer, calculated by imaginary time evolution. In (c) the laser beam is shortly behind it's first turning point, creating a density wave moving past it. After the second turning point (d) the stirrer creates a second wave, while the first one got reflected at the cloud edge, moving then parallel to the second one. At the end of the stirring procedure the stirrer arrived back to its starting point (e), having created two density waves that are interfering with each other.

4.3.2 Circular Stirring

Apart from measuring the critical velocity through phonon excitations, the creation of vortices, carriers of angular-momentum, is another interesting topic. Vortices will be discussed explicitly in chapter [6], but their relevant property for the moment is that they form, when a certain amount of angular momentum is put into a superfluid system, which can be achieved by stirring in a circular fashion inside of the condensate. Different stages during the procedure we are using for that purpose can be seen in figure 11. Similar to the linear stirring case we are starting with a Gaussian density distribution as shown in (a), depicting density and phase distribution of the condensate. The difference is that we are now using two laser beams instead of one, with the same distance to the cloud center, but on opposite sides. They are circulating around the center with a chosen angular velocity ω , chosen to be 50 Hz for the shown data. The ground state after imaginary time evolution is shown in (b), depicting a high density at the beam spots and a resulting overall reduction of the condensate size. This general appearance does not change during the course of our 300 ms stirring time as it can be seen in (c) after 100 ms. After starting to ramp down the laser power over 10 ms, the first vortex patterns are arranging after only a dozen of milliseconds as illustrated by the condensate in (d) 50 ms after deactivating the beams. Further free evolution time typically does not create any further vortices, but gives the cloud time to rethermalize and increase the contrast of the vortex lattice (e).

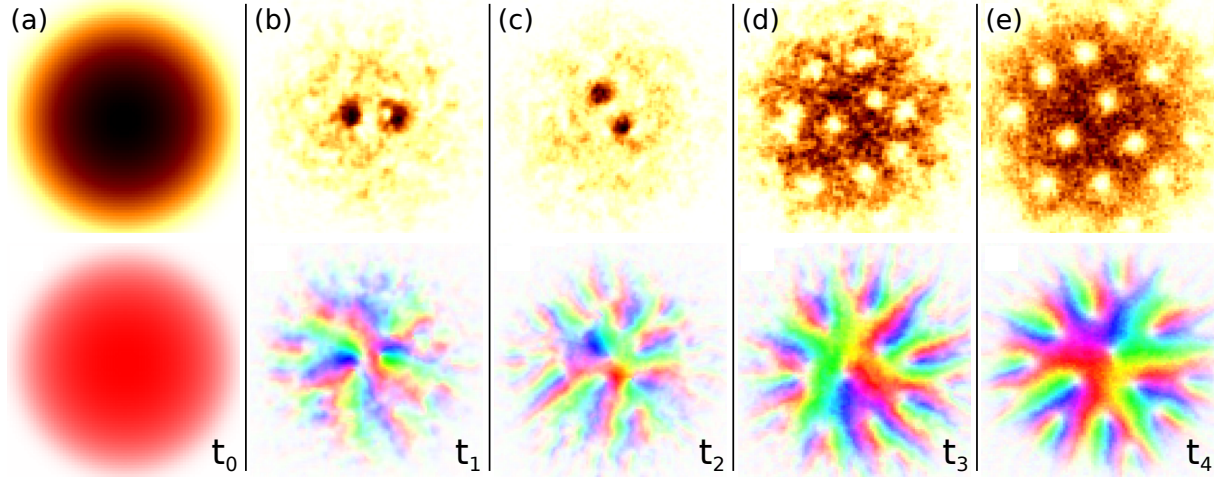


Figure 11: Density (upper row) and phase (lower row) of the simulated cloud, trapped under radially symmetric conditions with trap frequencies $f_{x,y} = 50$ Hz and $f_z = 500$ Hz, are shown at different times during the course of a circular stirring procedure for an angular stirring velocity of 50 Hz, above the critical frequency limit for vortex creation. (a) shows the initial Gaussian density distribution around the cloud center. (b) represents the energetic ground state with activated laser beams, calculated by imaginary time evolution. In (c) the laser beams are circulating for roughly 100 ms through the condensate. (d) depicts the situation 50 ms after the end of stirring and a rapid ramp down of the laser power. In (e) the condensate is shown at the end of the simulation process after 1 s of free evolution without laser beams.

4.4 Rescaling of Simulation Data

Striving for a detailed understanding of the investigated heating procedures, conformity between experimental data and simulations is highly desirable.

In the experiment, the BEC-fraction is easier accessible than the temperature, making it reasonable to convert our simulated temperature into BEC-fraction and compare on this basis. This conversion is performed straight forward following equation (2.1.4)

$$\frac{N_0}{N} = 1 - \left(\frac{T}{T_C} \right)^3$$

with the critical temperature for Bose-Einstein condensation according to equation [2.1.3]. First attempts in this direction revealed a significant deviation from lab results in the form of a highly enhanced heating in the simulations. This can be explained by the absence of any energy dissipation in the numerics, that is present in the experiment with hot atoms leaving the trap and the system losing energy over time.

To take this into account, we added a phenomenological coefficient c to adjust the heating.

$$\frac{N_0}{N} = 1 - \left(\frac{T_0}{T_C} + c \frac{\Delta T}{T_C} \right)^3 \quad (4.4.1)$$

As seen in the dotted lines in figure 12, with this additional factor, taking values on the order of 5% to 10%, we were able to match our data successfully for velocities below 0.5

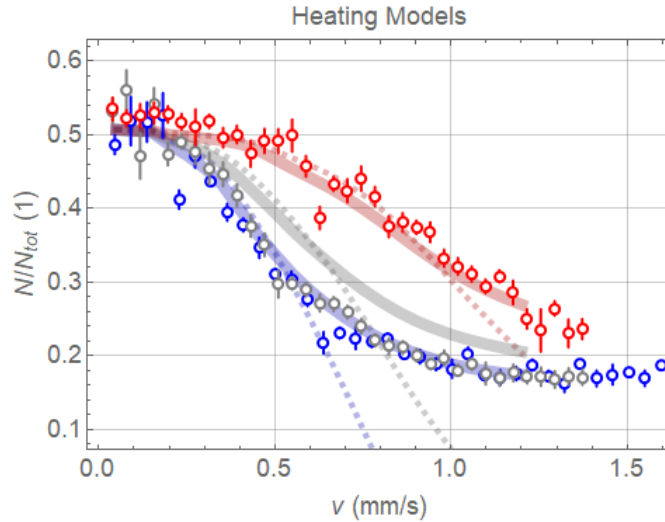


Figure 12: Comparison of the heating behaviour depicted in BEC-fraction, for experimental data (points with corresponding error bars) and simulation results (lines) is shown for an example run. Red symbolizes the reduction of BEC-fraction for stirring parallel to the dipole orientation, blue orthogonally to it and gray for a dipole-angle of 45° . Simulation data is fitted to the experimental results following equation (4.4.1) (dashed line) and equation (4.4.2) (solid line).

mm/s, but could not map the saturation effects kicking in for higher velocities in the experimental data. To respect this behaviour, probably caused by the loss of condensed atoms to the thermal fraction in the experiment, due to the heating and a reduction in further energy deposition. Therefore we scaled the heating additionally by the current BEC-fraction to replicate this procedure in the simulations, leading to

$$\frac{N_0}{N} = 1 - \left(\frac{T_0}{T_C} + c \frac{N_0}{N} \frac{\Delta T}{T_C} \right)^3. \quad (4.4.2)$$

This description allows for a remarkably good agreement between theory and experiment, as shown in the solid lines of figure 12. This is especially remarkable when considering that our numerics are working on the eGPE and therefore only describe zero-temperature processes, while a significantly large thermal fraction can be observed in the experimental data. This might indicate that thermal influences on the critical velocity and the heating behaviour in general play a subordinate role.

5 Breakdown of Superfluidity

The concept of superfluidity describes a wide range of remarkable many-particle phenomena where the most famous can be described as frictionless flow.

It arises in different areas of physics, manifesting itself in a vanishing electrical resistance in superconducting materials, where it was first observed [42], or as a loss of inner viscosity in liquid helium [43]. In this chapter we investigate a Dysprosium Bose-Einstein condensate under the influence of an external perturbation in the form of a Gaussian laser beam, with the aim to get insights into the breakdown process of this superfluid state. The corresponding breakdown procedure could be explained by Lev Landau in 1941 as a consequence of the creation of excitations inside the fluid [41]. This theory results in the postulation of the famous Landau-velocity that represents a remarkable connection between microscopic excitation spectra and macroscopic transport properties of superfluids.

5.1 Landau Critical Velocity

The starting point for the following discussions shall be an intuitive derivation of Landau's criterion. Even though the existence of superfluidity is a purely quantum mechanical phenomenon, the famous Landau velocity [41] for the breakdown of superfluidity can be derived in a remarkably intuitive way.

Considering an object with mass m moving inside a stationary superfluid with relative velocity \mathbf{v}_i , the initial energy E_i and momentum \mathbf{p}_i take the form:

$$E_i = \frac{m |\mathbf{v}_i|^2}{2} \quad ; \quad \mathbf{p}_i = m \mathbf{v}_i . \quad (5.1.1)$$

When passing through the fluid we assume the impurity to create an excitation at momentum \mathbf{p} and energy $\epsilon(\mathbf{p})$, resulting in the overall energy of both impurity and excitation of:

$$E_f = \frac{m |\mathbf{v}_f|^2}{2} + \epsilon(\mathbf{p}) \quad ; \quad \mathbf{p}_f = m \mathbf{v}_f + \mathbf{p} . \quad (5.1.2)$$

Here \mathbf{v}_f denotes the impurity's velocity after the interaction process, resulting in an excitation with momentum \mathbf{p} and energy $\epsilon(\mathbf{p})$. Using conservation of energy and momentum, one can easily show that

$$\mathbf{p} \cdot \mathbf{v}_i = \frac{|\mathbf{p}|^2}{2m} + \epsilon(\mathbf{p}) . \quad (5.1.3)$$

Separating the norm and direction of the impurities velocity ($\mathbf{v}_i = v_i \hat{\mathbf{v}}_i$) allows to explicitly solve for the velocity

$$v_i = \frac{\frac{|\mathbf{p}|^2}{2m} + \epsilon(\mathbf{p})}{\hat{\mathbf{v}}_i \cdot \mathbf{p}} . \quad (5.1.4)$$

This can only be fulfilled if v_i is larger than a minimal velocity threshold \mathbf{v}_c

$$v_i \geq v_c = \underset{\mathbf{p}}{\text{Min}} \left(\frac{\frac{|\mathbf{p}|^2}{2m} + \epsilon(\mathbf{p})}{\widehat{\mathbf{v}}_i \cdot \mathbf{p}} \right). \quad (5.1.5)$$

The right hand side of the upper inequality portrays the famous Landau critical velocity in its general form, describing which velocity the disturbance needs to exceed in order to be able to create excitations and therefore break the superfluid state. It is helpful, for promoting a deeper understanding of this relation, to take a closer look at two special cases.

In the strong coupling limit our excitation is a motion of the entire superfluid. In this case the overall momentum and energy result in $\mathbf{p} = \sum_i \mathbf{p}_i \equiv N \mathbf{p}_i$ and $\epsilon(\mathbf{p}) = N^2 p_i^2 / 2m$ where \mathbf{p}_i describes the single particle momentum, N the number of particles in the medium, and where we assume the momentum to be equally distributed over all superfluid constituents. Here the critical velocity v_c is zero, meaning that the pure presence of the impurity terminates the state of superfluidity.

In the weak coupling limit, the first summand in the numerator of the critical velocity can be neglected, resulting in the most prominent representation of Landau's critical velocity

$$v_c = \underset{\mathbf{p}}{\text{Min}} \left(\frac{\epsilon(\mathbf{p})}{\widehat{\mathbf{v}}_i \cdot \mathbf{p}} \right) \hat{=} \underset{\mathbf{k}}{\text{Min}} \left(\frac{\omega(\mathbf{k})}{\widehat{\mathbf{v}}_i \cdot \mathbf{k}} \right). \quad (5.1.6)$$

Here the right hand side, where to notation was switched from energy $\epsilon(\mathbf{p})$ and momentum \mathbf{p} to frequency $\omega(\mathbf{k})$ and wavevector \mathbf{k} , is the form of Landau's criterion that will be used for the rest of this thesis. The denominators in equation (5.1.6) imply some interesting behaviour. It has been shown [47] for dipolar superfluids, that, by plugging the dispersion relation (2.4.1) into the Landau criterion (5.1.6), the created excitations do not have to move in the same direction as the stirrer itself and an equation for the effective critical velocity has been derived that, adapted to our notation, takes the form

$$v_c(\eta) = v_{c,\parallel} v_{c,\perp} \left(\sin^2(\eta) v_{c,\parallel}^2 + \cos^2(\eta) v_{c,\perp}^2 \right)^{-1/2} \quad (5.1.7)$$

with $v_{c,\parallel}$ and $v_{c,\perp}$ describing the critical velocity parallel and orthogonal to the dipoles orientation and η the stirring angle inside the condensate-plane, ranging from parallel ($\eta = 0^\circ$) to orthogonal ($\eta = 90^\circ$) relative to the dipole-projection. Thus the critical velocity when stirring at a specific angle can be determined, as long as its counterparts along and perpendicular to the tilt are known. This predicted anisotropy in the sound velocity and therefore the critical velocity is a spectacular effect directly originating from the dipole-dipole interaction.

Such an anisotropy in the critical velocity has been predicted and discussed before [47,49], but has not been verified experimentally yet. In the following we will compare experimental and numerically simulated data for stirring a ^{162}Dy condensate with a macroscopic stirrer in order to proof the existence of this splitting. Using full numerical simulations enables us to take all possibly arising finite-size effects into account. Later on further simulations will deepen our qualitative understanding of the heating behaviour of such a stirred superfluid.

5.2 Anisotropy in the Critical Velocity of Dysprosium

In the strive for a full quantitative understanding of the critical Landau velocity in our system, we compare experimentally measured and numerically simulated heating behaviours of a ^{162}Dy condensate containing approximately 8,000 atoms and aim to extract the stirring velocity threshold above which significant heating in the dBEC sets in.

Our procedure for investigating the heating behaviour of a Dysprosium BEC, as it is fully explained in section [3.3], looks the following. After forming a ^{162}Dy condensate, we stir it linearly with a laser beam of size $w_0 = 1.5 \mu\text{m}$ and with a power of $P = 1.0 \mu\text{W}$. Through comparison of the system before and after the stirring we can determine the effective heating and through its onset the critical velocity of the system.

In order to determine this critical velocity v_c we apply a fit-function, partially zero, describing the dissipationless regime, and partially rising, describing the heating after exceeding the velocity threshold. The exact heating behaviour for a macroscopic stirrer with non-uniform potential depth, as is our Gaussian laser beam, is unknown. Therefore we will fall back onto a description as a point-like stirrer. The heating induced by such an impurity has been theoretically investigated in [45], resulting in the following approximated fit-function for our system

$$T_{\text{theo}}(v) = T_0 + h t_s \frac{v^3}{v_c^3} \left(\frac{v_c^2}{v^2} - 1 \right)^2 \Theta(v - v_c) \quad (5.2.1)$$

with T_0 as the initial temperature, h describing a heating-factor, t_s the overall stirring time, in all our systems chosen to be 1s, v_c the critical velocity threshold, v the stirrer velocity and Θ the Heaviside-function.

This function is of course obtained for an idealised system and can not quantitatively represent our data. This justifies the need for full numerical simulations. However, extracting a critical velocity in order to compare experimental and simulated results requires a fitting-function to be used. While using the function (5.2.1) achieves reasonable results for the relatively smooth simulation data, it generates massive fitting-errors in the case of the more diffuse experimental results, making it impractical to use here. Therefore we will content ourselves to a pragmatic linear fit-function that has already been used, in similar form, in the context of critical velocity measurements [50].

$$T_{\text{lin}}(v) = T_0 + h t_s \left(\frac{v}{v_c} - 1 \right) \Theta(v - v_c) \quad (5.2.2)$$

The results of this fitting-procedure to the experimental data points are presented in form of dotted lines in the figures 13, 14 and 15. The extracted velocity thresholds, marked by arrows in the figure, have been summarised in table 1. Linear fitting was performed for the experimental and simulated data, but to maintain clarity, only the former ones are shown in the plots.

| Plot | α [°] | R [μm] | f_x [Hz] | f_y [Hz] | f_z [Hz] | η [°] | $v_c(\text{Exp})$ [$\mu\text{m/s}$] | $v_c(\text{Sim})$ [$\mu\text{m/s}$] |
|------|--------------|---------------------|------------|------------|------------|------------|---------------------------------------|---------------------------------------|
| (a) | 0 | 2 | 49(1) | 52(2) | 168(1) | 0 | 198(31) | 210(7) |
| | | | | | | 45 | 197(16) | 189(18) |
| | | | | | | 90 | 210(40) | 211(6) |
| (b) | 90 | 1 | 49(1) | 52(2) | 168(1) | 0 | 350(39) | 358(8) |
| | | | | | | 45 | 144(36) | 268(8) |
| | | | | | | 90 | 161(13) | 162(11) |
| (c) | 90 | 1 | 81(7) | 39(2) | 140(9) | 0 | 260(49) | 334(15) |
| | | | | | | 45 | 105(13) | 204(4) |
| | | | | | | 90 | 128(30) | 160(10) |
| (d) | 90 | 2 | 49(1) | 52(2) | 168(1) | 0 | 565(54) | 710(19) |
| | | | | | | 45 | 216(54) | 213(12) |
| | | | | | | 90 | 208(58) | 188(20) |

Table 1: Critical velocities from experimental and simulated results shown in figures 13, 14 and 15 via the fitting function 5.2.2, with the standard fit deviation in brackets.

Creating anisotropy in the critical velocity

The most striking effect that will be extensively investigated in this chapter is the difference of the critical velocity in different directions relative to the dipole-orientation in our dipolar superfluid, a ^{162}Dy Bose-Einstein condensate.

This effect can be easily observed in figure 13 (a) and (b). In (a) the magnetic field is pointing out of the condensate plane, creating an isotropic interaction strength in all horizontal directions inside the BEC. Therefore stirring along different directions results in the same heating threshold. This behaviour is verified in the presented experimental and simulated results. When comparing this with (b), where the dipoles are tilted inside of the plane ($\alpha = 90^\circ$) and the interactions differ along and perpendicular to the tilt-direction, a significant change is therefore observable in the critical velocity.

Fitting a linear function onto the experimental data following equation (5.2.2), in the case of a vertical magnetic field orientation (a), reveals critical velocities that are identical ($v_c^a \approx 200 \mu\text{m/s}$) within their fitting-errors for parallel, orthogonal and in-between stirring. This is true for the experimental as well as the simulated results, even showing a notable agreement between these two. When tilting the magnetic field, the critical velocities separate, with a significant increase in the parallel ($v_{c,0^\circ}^b \approx 350 \mu\text{m/s}$) and a small decrease in the orthogonal stirring direction ($v_{c,90^\circ}^b \approx 160 \mu\text{m/s}$), again in excellent agreement between experimental and numerical results. Experimental data-points that have a significant deviation from their surrounding and are located near the trap frequencies (gray dots) are excluded from the fitting procedure, as they are most likely a result of a center-of-mass oscillation in the trap, creating additional heating that is in no context to the critical velocity we strive to investigate.

This increase of the critical velocity in the parallel stirring direction is in accordance with the theory for the speed of sound in a homogeneous system, as was discussed in section 2.4.1 where the sound velocity parallel to the dipole orientation was predicted to be higher than orthogonal to it. Stirring under an angle of $\eta = 45^\circ$ features a special behaviour with a critical velocity between the earlier discussed cases in the simulation ($v_{c,45^\circ}^{b,\text{Sim}} \approx 270 \mu\text{m/s}$),

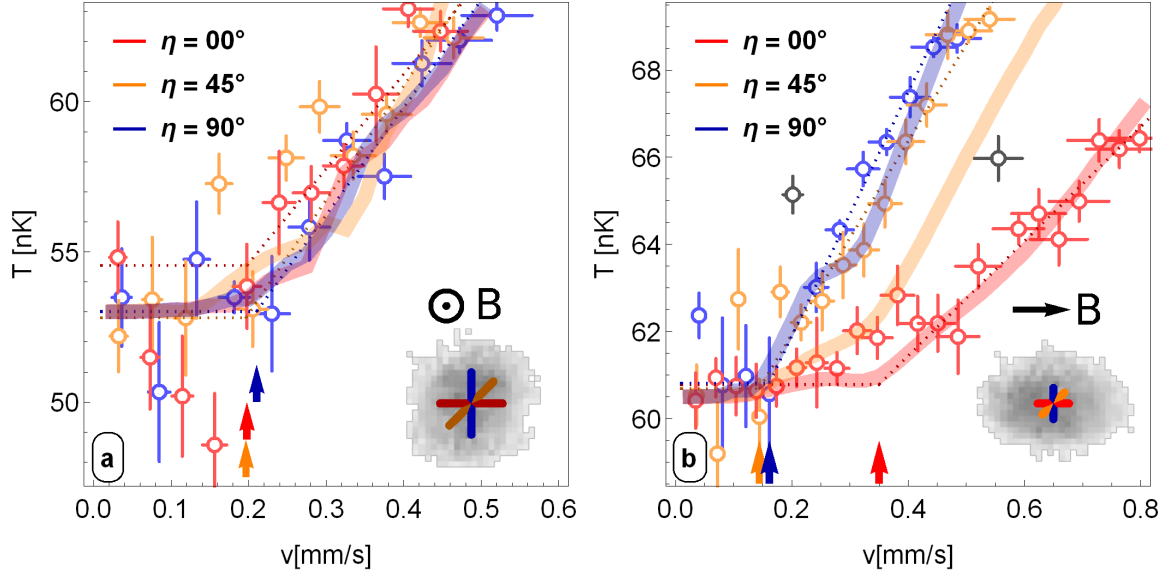


Figure 13: Comparison of the Heating behaviour when tilting the magnetic field out of (a) and into the BEC plane (b). Experimental (dots) and simulated (broad lines) results for the heating of a ^{162}Dy condensate with approx 8,000 atoms when stirred with a Gaussian laser beam with a beam waist of $w_0 = 1.5 \mu\text{m}$ and power of $P = 1.0 \mu\text{W}$. The respective trapping conditions and stirrer parameters are summarised in table 1 together with the critical velocity threshold determined following a linear fit via equation (5.2.2). The fits to the experimental data points are shown in the form of dotted lines and the fitted critical velocity is highlighted by coloured arrows on the bottom side, for the experimentally measured data. Additionally a density scheme of the respective measured cloud is shown in the bottom right corner with colored bars representing the stirring path. It is worth noting that the width of the bars does not reflect the correct beam waist of the stirrer, which is significantly bigger. Experimental data-points that have a significant deviation from their surrounding and are located near the trap frequencies (gray dots) are excluded from the fitting procedure.

but a behaviour similar to the orthogonal ($v_{c,45^\circ}^{b,\text{Exp}} \approx 144 \mu\text{m/s}$) stirring in the experimental data. This simulation result represents an uncommon case. A similarity with the orthogonal stirring case can be identified in all other data sets and can be justified following the discussions around equation (5.1.7) in the last section.

When applying the results discussed there, a critical velocity of $v_{c,45^\circ}^{b,\text{Theo}} = 205.8 \mu\text{m/s}$ can be calculated, being significantly closer to the orthogonal than the parallel stirring result. These data sets demonstrate in a very intuitive way how the anisotropic interaction strength over the macroscopic size of the condensate, due to the direction-dependent dipole-dipole interaction between the condensate particles, induces a split-up of the critical velocity in different directions relative to the dipole tilt.

Influence of Magnetostriction

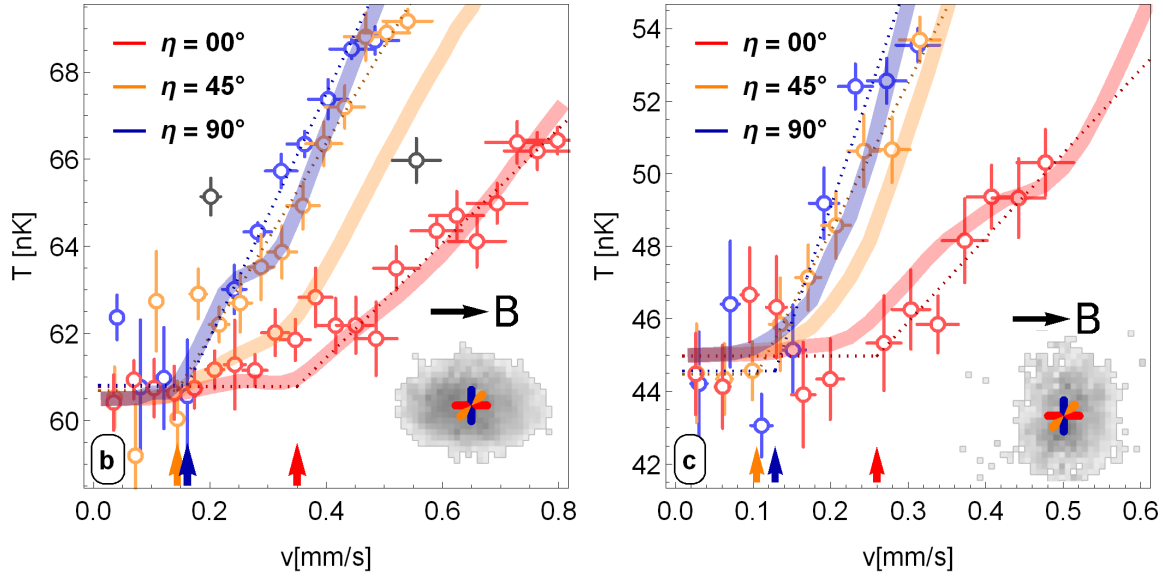


Figure 14: Comparison of the heating when changing the cloud aspect ratio from $\kappa_a = R_x/R_y \approx 1.4$ (b) to $\kappa_b = R_x/R_y \approx 1.4^{-1}$ (c). The meaning of the plot constituents is identical to figure 13. Even though the exact critical velocity position varies when inverting the cloud aspect ratio, the splitting itself remains, proving that magnetostriction is not the origin of the phenomenon.

It might not be obvious that the anisotropy in the critical velocities is an effect of the anisotropic interaction itself, but rather a relict of the anisotropic density distribution due to the effects of magnetostriction on the atomic cloud modifying the density landscape following equation (2.4.3).

In order to falsify this claim, the heating behaviour of two condensates with reversed cloud aspect ratios is compared in figure 14 (b) and (c). For both cases, (b) with $\kappa_a = R_x/R_y \approx 1.4$, and (c) with $\kappa_b = R_x/R_y \approx 1.4^{-1}$ we estimate the critical velocity via a linear fit to the experimental and simulated data, with the results shown in table 1.

Comparing the resulting critical velocities for both cloud conditions, several relevant aspects are striking. First of all, in agreement with the discussion above, stirring parallel to the dipole-tilt-direction results in a significantly higher critical velocity and lower overall heating compared to stirring in other directions. This clearly shows that the observed effect is not caused by magnetostriction.

Furthermore the significant mismatch between the simulated and experimentally measured heating behaviours of $\eta = 45^\circ$ -case, as it was known from (b) has significantly decreased in (c), with the numerical results here confirming the similarity to the orthogonal stirring case. The quantitative difference in the critical velocities between (b) and (c) might be caused by them not possessing the exact same density distribution.

Overall the analysis of figure 14 (b) and (c) demonstrated that the anisotropy in the critical velocity is not caused by pure magnetostriction effects, even though the cloud form and therefore the trapping conditions seem to have an impact on the exact value of the critical velocity.

Varying the Stirring Amplitude

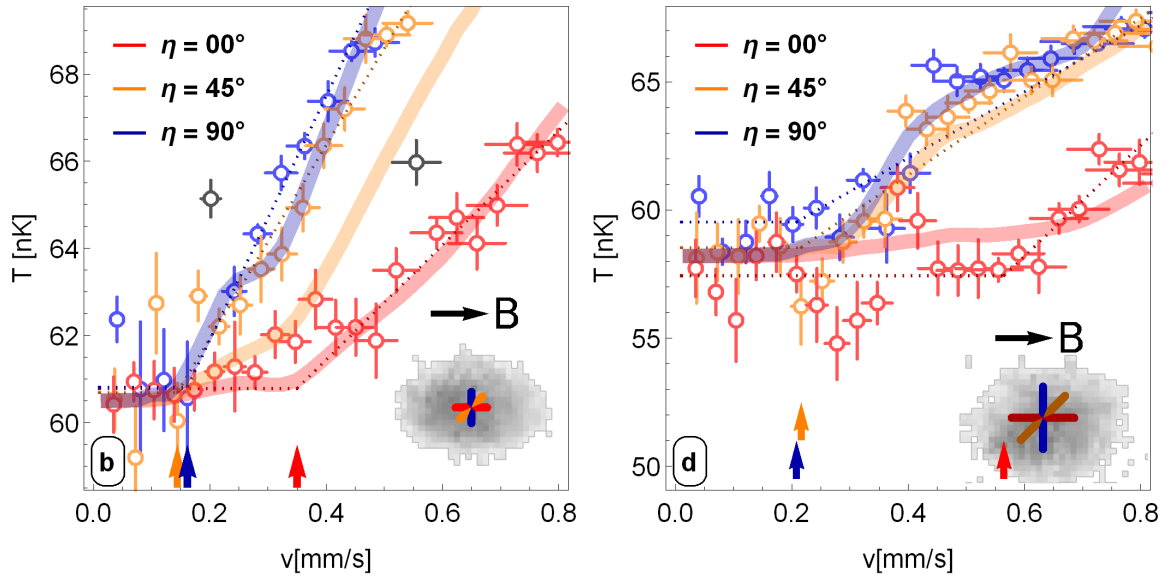


Figure 15: Comparison of the heating when increasing the stirring amplitude from $R = 1.0 \mu\text{m}$ (b) to $R = 2.0 \mu\text{m}$ (c). The meaning of the plot constituents is identical to figure 13. Stirring over an increased distance and therefore stirring lower density regions increases the critical velocity in all stirring direction, whereby the effect is significantly stronger parallel to the dipole-tilt.

The next logical step is to study variations in the stirring procedure. For this reason the stirring amplitude has been varied from $1.0 \mu\text{m}$ to $2.0 \mu\text{m}$ from figure 15(b) to (d). An increase in the stirring amplitude is also equivalent to affecting areas with lower density against the edges of the condensate possessing a lower local speed of sound, following the discussions in section 2.4.1.

Apart from this an overall increase in the critical velocity is observable in all stirring directions, whereby the $\eta = 45^\circ$ -case ($v_{c,45^\circ}^{\text{d,Exp}} = 216 \mu\text{m/s}$) again behaves nearly identical to the orthogonal stirring version ($v_{c,90^\circ}^{\text{d,Exp}} = 208 \mu\text{m/s}$). This behaviour is again in agreement with the simulated ($v_{c,45^\circ}^{\text{d,Sim}} = 213 \mu\text{m/s}$) result, that predict the same similarity.

Furthermore the structure of the heating process has obviously noticeably changed from (b) to (d), exhibiting a flat heating region after the original onset of dissipation for the orthogonal stirring direction and significantly later onset of heating in the orthogonal direction. Such variations will be investigated in more detail in the following section 5.3.

The fitted critical velocities orthogonally and diagonal to the field direction only changed insignificantly, while parallel stirring shows a drastically later onset of heating. It can, at this point, not clearly be verified whether this effect is caused by stirring in lower density regions, or by other effects, motivating ones again a more detailed numerical investigation of the critical velocity dependencies that shall be given in the next section.

Short Summary

The most important results of this thesis are summarised in figures 13, 14 and 15. There it was verified experimentally as well as numerically that the critical velocity in a ^{162}Dy Bose-Einstein condensate can be manipulated by an outer magnetic field aligning the atomic dipoles, allowing to achieve different critical velocity thresholds parallel and orthogonal to the projection of this dipoles.

The described splitting is not caused by a pure density modification through magnetostriction and the exact values of the critical velocity can be altered by changing the cloud shape as well as certain parameters of the stirring procedure, like the stirring amplitude.

5.3 Qualitative Behaviour of the Critical Velocity

The previously shown experimental results were able to verify a splitting of the critical Landau velocity in the condensate plane if the dipoles in a dipolar superfluid are tilted ($\alpha \neq 0^\circ$). In the following a quantitative analysis of a ^{162}Dy condensate's heating behaviour under variation of different parameters of the stirring process shall be given. As no experimental data corresponding to the following simulations exist, we will limit ourselves to qualitative discussions of the resulting heating behaviour.

5.3.1 Anisotropic Heating of a Dipolar Superfluid

Following the discussions in section 5.2, where the existence of a separation of the critical velocities in different directions due to the anisotropy in the dipole-dipole interaction of the condensate particles has been demonstrated, it seems natural to investigate this splitting in more detail. Therefore we manipulate the dipole-orientation in the cloud through an external magnetic field and observe how the overall heating behaviour, following a stirring sequence, behaves.

In figure 16 the simulated heating per atom in dependence of the stirring velocity for different magnetic field angles from $\alpha = 0^\circ$ (a) to $\alpha = 90^\circ$ (d) is presented. A negligible heating can be observed in the beginning of each of the shown heating curves, transitioning smoothly into an approximately linear regime, before saturation effects start to gain impact and the overall heating decreases again. The origin of this saturation is not fully understood yet. It might originate in the fact that at high frequencies the BEC experiences a time-averaged potential rather than a moving impurity.

Comparing the overall amount of heating in figure 16 (a)-(d) it is noticeable that tilting the magnetic field inside the BEC-plane reduces the heating by the stirring procedure. A closer look at the beginning of the heating curves reveals that the onset of heating, even though it can only be estimated, seems to be practically constant in the orthogonal stirring direction (solid lines), but moves to higher velocities for orthogonal stirring (dashed lines). This behaviour is in excellent agreement with the experimental results in the last section (figure 13) and reflects the behaviour of sound waves in a homogeneous condensate as discussed section 2.4.1.

Herewith we verified that this behaviour, as it was identically observed in chapter 5.2, behaves monotonically also for arbitrary intermediate angle conditions.

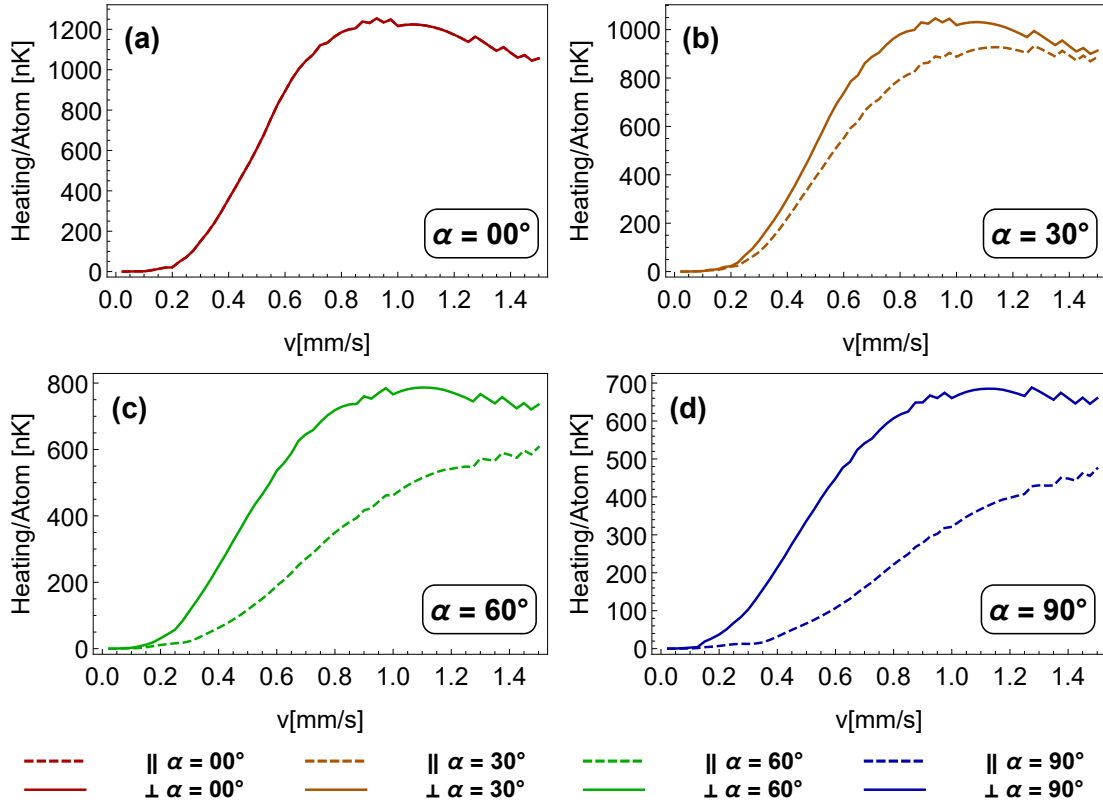


Figure 16: The simulated heating per atom in dependence of the velocity of the stirring beam and of the magnetic field angle for 8,000 atoms in a cylindrically symmetric trap with a radial trap frequency of $f_{x,y} = 50$ Hz and a vertical trap frequency of $f_z = 168$ Hz and for a stirring amplitude of $R = 1 \mu\text{m}$, is shown. The heating behaviour for stirring parallel and orthogonal to the projection of the magnetic field onto the condensate-plane, can be seen in dashed and solid lines. (a)-(d) present the heatings rescaled to 1 s of overall stirring time for one specific field angle respectively.

5.3.2 Variation of the Stirring Angle

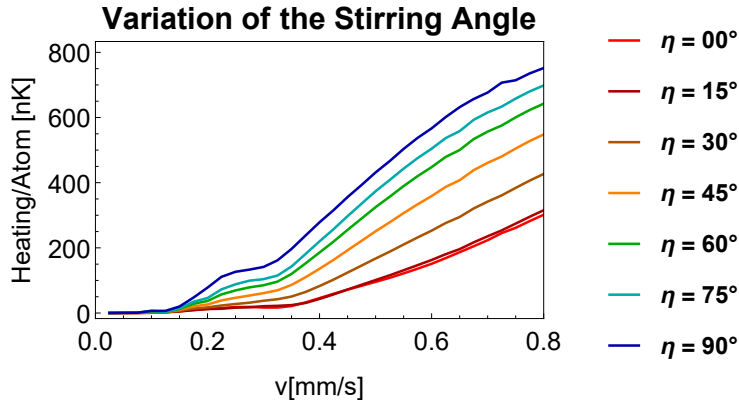


Figure 17: Simulation for the heating per atom in dependence of the stirring beam's velocity and its angle with respect to the magnetic field (η) for 8,000 atoms with trap frequencies of $f_x = 49$ Hz, $f_y = 52$ Hz and $f_z = 168$ Hz for a stirring amplitude of $R = 1 \mu\text{m}$. The magnetic field is tilted inside the BEC-plane ($\alpha = 90^\circ$). The simulated heating for a single oscillation is rescaled to an overall stirring time of 1 s.

A further interesting aspect is the heating behaviour of the BEC when stirring along different angles with respect to the magnetic field being tilted into the BEC plane ($\alpha = 90^\circ$). This problem has been theoretically investigated in [47] where it could be shown that the critical velocity only coincides with the speed of sound in the system when stirring parallel ($\eta = 0^\circ$) or orthogonally ($\eta = 90^\circ$) to the dipole orientation. In the intermediate steps the critical velocity is described by equation (5.1.7) as was discussed in section 5.1. The results of these simulations can be seen in figure 17 in form of the heating rescaling to a full second of stirring .

What can be observed is a monotonous increase in the overall heating when varying the stirring angle η from parallel to orthogonal relative to the dipole orientation. In the simulated heatings a clear peak around $200 \mu\text{m/s}$ is apparent. This corresponds to a stirring frequency of

$$f_s = \frac{v_s}{4R} = \frac{200 \frac{\mu\text{m}}{\text{s}}}{4 \mu\text{m}} = 50 \text{ Hz} \quad (5.3.1)$$

which is equivalent to the mean radial trap frequency. Therefore this peak can be understood as an additional heating due to the excitation of the center-of-mass oscillation of the condensate.

In the presented results a clear trend is observable showing the anisotropy in the condensate heating, with a monotonous decrease of the dissipation when stirring parallel either than orthogonal relative to the dipole-orientation.

This agrees nicely with the already discussed theoretical predictions for the behaviour of the speed of sound in a three-dimensional homogeneous system in 2.4.1.

5.3.3 Variation of the Stirring Amplitude

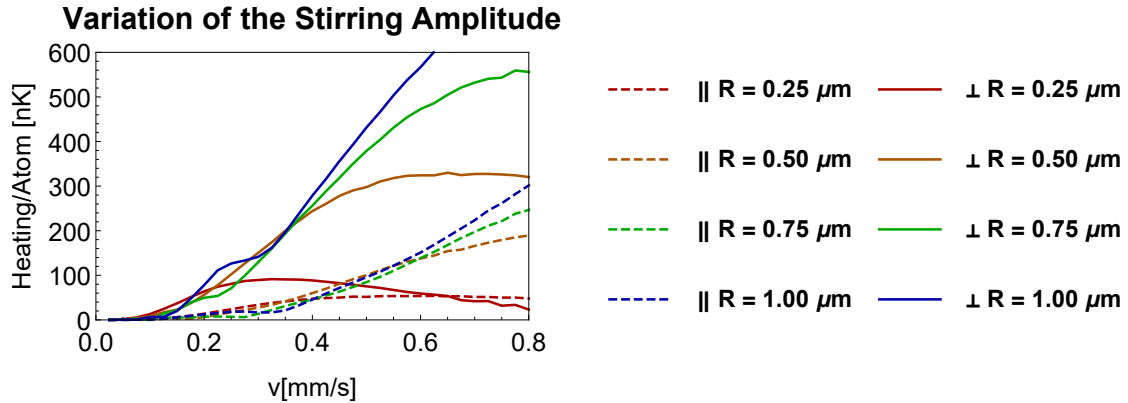


Figure 18: Simulated heating per atom of a ^{162}Dy condensate with 8,000 atoms in a trap with trap frequencies of $f_x = 49\text{ Hz}$, $f_y = 52\text{ Hz}$ and $f_z = 168\text{ Hz}$ in an external magnetic field tilted inside the BEC plane ($\alpha = 90^\circ$) when varying the stirring velocity of a stirrer with a beam waist of $w_0 = 1.5\text{ }\mu\text{m}$. The heating after rescaling to $t_{\text{stir}} = 1\text{ s}$ is shown when varying the amplitude of the stirring movement.

In the next step we study the effect of a variations in the stirring amplitude, meaning the distance that the stirrer travels each oscillation while the dipoles are oriented inside the BEC plane ($\alpha = 90^\circ$).

In figure 18 the heating per atom rescaled to a full second of stirring is shown for different stirring amplitudes inside a cloud with a radius of around $4\text{ }\mu\text{m}$.

It is apparent that the dissipated energy increases strongly with the stirring amplitude. This can be understood when considering the density distribution of a (dipolar) Bose-Einstein condensate that forms an inverted parabola with decreasing density against the edges. Stirring with bigger amplitudes around the center reaches regions with lower density, resulting in a decreased local speed of sound following equation (2.4.3). This simplifies the creation of sound waves, increasing again the overall heating.

The heating peak around $v \approx 200\text{ }\mu\text{m/s}$ that we identified as the center-of-mass oscillation in the last section, grows significantly with the stirring amplitude, indicating that it involves long-wavelength excitations.

What is further clearly visible in figure 18, is that the heating maximum, before saturation effects get to strong, shifts to higher velocities when the stirring amplitude is increased. The maximum of heating shifts to higher velocities as the amplitude is increased, which seems to agree with the assumption that this saturation is caused by time-averaging at high frequencies. The critical velocity in the form of the onset of heating can not clearly be identified, as the position of the heating peak makes the behaviour in the relevant velocity range unpredictable.

5.3.4 Variation of the Beam Size

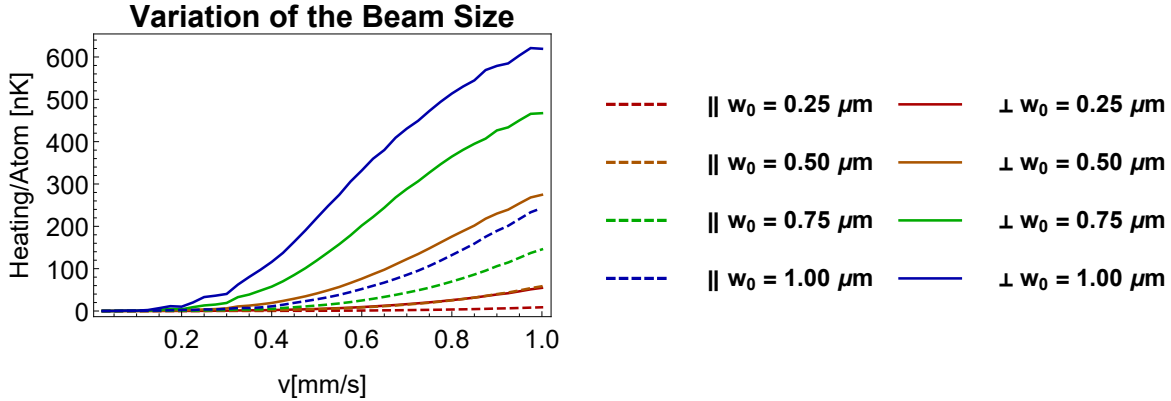


Figure 19: The simulated heating per atom rescaled to 1 s of a ^{162}Dy condensate with 8,000 atoms trapped by trap frequencies of $f_x = 49$ Hz, $f_y = 52$ Hz and $f_z = 168$ Hz when stirring with varying velocity and a radius of $R = 1$ μm , rescaled to a stirring duration of $t_{\text{stir}} = 1$ s, is shown. Resulting thereby the generated heating for different stirrer sizes from $w_0 = 0.25$ μm to $w_0 = 1.00$ μm is compared. The curve for parallel stirring with a beam size of $w_0 = 0.50$ μm is nearly directly on its orthogonal $w_0 = 1.25$ μm counterpart and is therefore hardly visible.

Further we vary the size of the stirring beam. Most of the theoretical work on stirred dipolar quantum gases is based on point-size stirrers [45,47], making it interesting to investigate the influence of the size of macroscopic stirrers. We vary the beam waist and laser power as described in the following. Changing the beam waist of a Gaussian laser beam also alters the potential depth following equation (3.3.1). In order to distinguish between the influence of changes in beam waist w_0 and potential depth V_{stirrer} , the latter will be held constant by adapting the laser power P .

$$V_{\text{stirrer}} \propto \frac{P}{w_0^2} \xrightarrow{V_{\text{stirrer}} \text{ constant}} P \propto w_0^2 \quad (5.3.2)$$

Under these conditions, the heating behaviour takes the form shown in figure 19 with the heating per atom rescaled to a stirring duration of 1 s for different beam waists at a constant potential depth. With increasing beam waist the overall heating seems to increase significantly. This can be explained by two different considerations. First by increasing the beam waist, the area of the beam increases significantly and a higher number of atoms is accelerated by the stirrer, increasing the overall heating.

Secondly when the beam with a bigger beam waist is oscillating with the same oscillation amplitude as a smaller one, it stirs regions with lower density, reducing the speed of sound and simplifying the creation of excitations. This last point would also predict a reduction in the systems speed of sound and therefore possibly in the critical velocity. A close look at the heating in the low velocity regime confirms this.

5.3.5 Variation of the Potential Depth

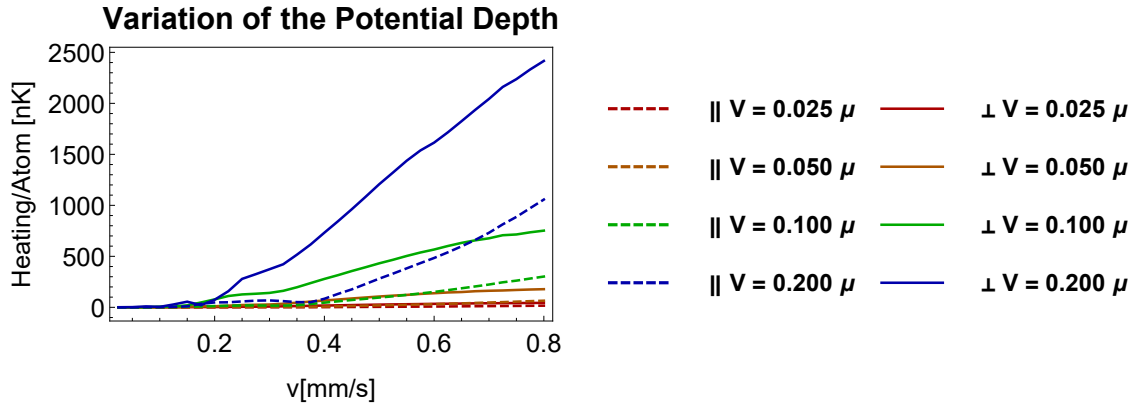


Figure 20: The simulated heating per atom rescaled to 1 s of heating for a ^{162}Dy condensate with 8,000 atoms with trap frequencies of $f_x = 49$ Hz, $f_y = 52$ Hz and $f_z = 168$ Hz when stirring with varying velocity at a beam waist of $w_0 = 1.5 \mu\text{m}$ and a radius of $R = 1 \mu\text{m}$, rescaled to a stirring duration of $t_{\text{stir}} = 1$ s, is shown. The potential depth of the stirrer is increased from $0.25 \mu\text{W} \hat{=} 0.025 \mu$ to $2.0 \mu\text{W} \hat{=} 0.200 \mu$.

The second beam parameter whose influence we want to investigate is the potential depth, leading to the heating curves shown in figure 20. The potential depth is varied by changing the laser power from $0.25 \mu\text{W} \hat{=} 0.025 \mu$ to $2.00 \mu\text{W} \hat{=} 0.200 \mu$, where the power can be translated into potential depth by equation (3.3.1). This then needs to be compared to μ , the chemical potential of the dipolar condensate [12], given by

$$\mu = g n (1 - \epsilon_{\text{dd}} f_{\text{dip}}(\kappa)) . \quad (5.3.3)$$

with $f_{\text{dip}}(\kappa)$ the dipolar anisotropic function given in equation (2.3.13) and a κ for our clouds of around 3.57. With higher potential depths the heating increases drastically by a factor of around 60 between the $V = 0.025 \mu$ and $V = 0.200 \mu$. This can be understood in the following way. When increasing the stirring potential, the interaction with the atoms increases, pulling more particles into the beam and increasing the transferred energy.

Experimentally a trade-off has to be found between obtaining observable heating within the lifetime of the sample and a sufficiently low coupling to observe superfluid flow and the onset of heating. This justifies the choice of laser power that was made.

5.3.6 Influence of the Number of Stirring Cycles

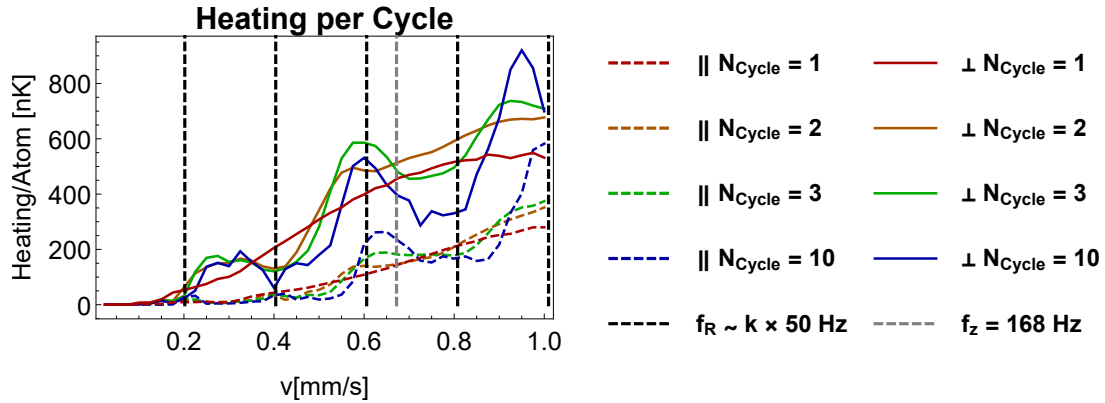


Figure 21: The simulated heating per atom rescaled to 1 s of stirring time divided by the number of stirring cycles is shown. The BEC, consisting of 7,500 atoms, was trapped in a trap with frequencies $f_x = 49$ Hz, $f_y = 52$ Hz and $f_z = 168$ Hz and was stirring by an attractive laser beam with $1 \mu\text{m}$ stirring amplitude and a beam waist of $w_0 = 1.5 \mu\text{m}$. The vertical lines represent the mean radial (black) and horizontal (gray) trap frequencies.

All the simulation results in this chapter are calculated for a single stirring oscillation and then rescaled to an overall stirring time of 1 s, in order to make them comparable with experimental results, where the heating after a single oscillation would be not detectable. In order to verify that this rescaling procedure is even useful, and that therefore effects of density variations when stirring multiple times over the same locations play no significant role, we compare the heating after different numbers of stirring cycles.

The heating for several oscillation cycles is rescaled down again to 1 oscillation for comparability. This just means that the heating is divided by the respective number of cycles with the results shown in figure 21

The heating for a higher number of oscillations seems to oscillate around the single oscillation case with increasing amplitude for higher cycle numbers. This might indicate that we continue pumping collective modes, like the center-of-mass oscillation discussed before, with every successive cycle. A phenomenon like this would quite surely not appear in a realistic experimental setup, where strongly accelerated atoms would just leave the trap. With an increasing reduction in the atom number, the heating would then reduce and the long-term behaviour would differ from a linear tendency. Another possible explanation for the curious heating after several cycles might be that every oscillation cycle is able to create density waves moving through the condensate. The stirrer on its path will surely cross them over and over again. Depending on the exact stirrer velocity these waves will be passed more often in parallel or anti-parallel direction, what might cause either an increase or decrease in the respective heating.

In the end, the heating after several stirring cycles in our simulations seems to behave roughly as the multiple of a single stirring move, validating the validity of our scaling procedure.

5.3.7 Variation of the S-Wave-Scattering Length

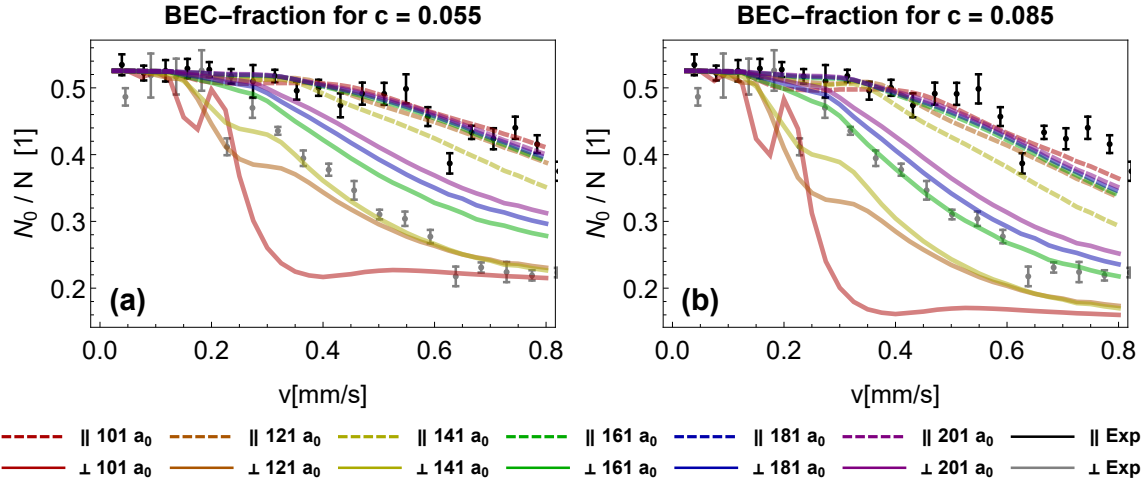


Figure 22: The simulated heating behaviour for a ^{162}Dy condensate with 8,000 atoms, trapped under $f_x = 49$ Hz, $f_y = 52$ Hz and $f_z = 168$ Hz, for different contact scattering lengths is shown. In (a) and (b) experimental and simulated results are compared in form of the resulting BEC-fraction. The simulation data is fitted onto the experimental results following equation 4.4.2 with the corresponding heating factor c given on topside of the plots.

A further aspect of interest is whether the data collected during the work on this thesis can be used to determine not exactly known characteristics of the used dipolar atoms. Therefore in the following the influence of the background scattering length of ^{162}Dy shall be evaluated. In (a) and (b) the simulated results are fitted onto experimental results for a ^{162}Dy cloud in the form of the resulting BEC-fraction following equation (4.4.2). During this fitting the heating factor c is chosen in a way to achieve optimal agreement between the experimental and simulated results. The heating peak that we connected to a center-of-mass oscillation in the last sections can be seen to increase massively with a reduction in the s-wave scattering length a_s . Similar to that, the overall amount of heating noticeably increases with the scattering length. This is understandable as a reduction in the scattering length reduces the systems speed of sound, following equation (2.4.3) and therefore making phonon excitation easier.

An optimal agreement between experimental and simulated data is not creatable by varying the heating factor c for any of the shown data sets, but a very good agreement in the orthogonal stirring direction can be created for three scattering lengths ($a_s = 121 a_0$, $a_s = 141 a_0$ and $a_s = 161 a_0$) to the cost of deviations in the parallel direction for high velocities. Examples are shown in (a) with the $a_s = 141 a_0$ curve fitting best, while in (b) the $a_s = 161 a_0$ data set is chosen to fit the experimental results as good as possible. In both cases the conformity to the experiment is given for velocities below approximately $600 \mu\text{m/s}$ in the parallel direction. Overall our results do not allow us to determine to s-wave scattering length for ^{162}Dy exactly, but narrow it down to a region between $121 a_0$ and $161 a_0$. These findings are thereby in excellent agreement with conclusions published by the Stanford group of Benjamin Lev, where the s-wave scattering length for ^{162}Dy

was determined in several attempts to be $a_s = 141(17) a_0$ [35], $a_s = 154(22) a_0$ [51] and $a_s = 122(10) a_0$ [58,59].

6 Vortices

In the previous chapter the onset of dissipation in a superfluid above a critical flow velocity threshold was discussed, and the creation of excitations, following an argumentation of Lev Landau, was identified as the origin of this phenomenon.

While phonons and rotons are possible quasi-particles able to cause this breakdown of superfluidity, another mechanism exists that can arise at even lower flow velocities: Vortex creation [50]. Superfluids are irrotational, as will be shown in the first section of this chapter, and therefore need a process to get rid of that angular momentum, should it be added to the system. This is done by the creation of an excitation that carries angular momentum, the vortex, a density hole with particles rotating around a central core [60].

Verifying the presence of vortices is of special interest, since it gives the clearest visible evidence for the existence of superfluidity in a system [61]. While vortices have been observed many times in isotropic systems [50,62], they have never been observed in a dipolar system, enabling us to perform pioneering work in this direction with our Dysprosium dBECs. Due to the anisotropic dipole-dipole interactions in Dysprosium we expect variations in the density distribution around the vortex core [71], as well as adaptations in their relative alignment [40,64,65].

6.1 Theoretical Background

In order to allow an easy access into the very broad topic of vortices in superfluids we will start with a very short introduction of the most relevant characteristics and properties analysed in later parts of this chapter. More detailed explanations and derivations can be found in the summary papers [60,57] or in the well known standard work [22].

Vortices in homogeneous superfluids

The wave function of a weakly interacting BEC can be written in the form [22]:

$$\Psi(\mathbf{r}) = \sqrt{n_0} e^{i\phi(\mathbf{r})} \quad (6.1.1)$$

where the density-dependence n_0 and phase-behaviour $\phi(\mathbf{r})$ can be separated.

The latter is directly related to the local particle velocity [23].

$$\mathbf{v}(\mathbf{r}) = \frac{\hbar}{m} \nabla \phi(\mathbf{r}) \quad (6.1.2)$$

A remarkable property of condensates following the above velocity dependence is that they are irrotational, as can be seen by taking the curl of $v(\mathbf{r})$.

$$\nabla \times \mathbf{v}(\mathbf{r}) = \frac{\hbar}{m} \nabla \times \nabla \phi(\mathbf{r}) = 0 \quad (6.1.3)$$

This results from $\phi(\mathbf{r})$ being a scalar field and the fact that the curl of a scalar fields gradient always vanishes $\nabla \times (\nabla \phi) = 0$. Due to its inability to rotate, the superfluid is

forced to process the desired angular momentum in form of the creation of a vortex. The intuitive reason for vortex creation is therefore, that the only way to satisfy $\nabla \times \nabla\phi = 0$ is to displace all particles from the rotation spot ($n_0 = 0$) and thereby creating a hole in the condensate, a vortex core. The phase coherence of a superfluid forces the phase change around a closed path around the vortex core to be multiples of 2π [22]

$$\oint \mathbf{v}(\mathbf{r}) \cdot d\mathbf{l} = 2\pi \frac{\hbar}{m} n_v = \frac{h}{m} n_v \quad (6.1.4)$$

with $n_v = 0, \pm 1, \pm 2, \dots$ describing the angular momentum of the vortex constituents as multiples of h/m , typically labeled "charge", of the vortex. The velocity of particles moving on circular lines perpendicular to the vortex axis at a distance r_\perp can be derived from equation (6.1.4) to be

$$v = \frac{\hbar}{m r_\perp} n_v . \quad (6.1.5)$$

With the conducted groundwork we are now able to look for the onset of vortex creation and therefore the rotation speed threshold above which the first vortices appear. The energy necessary for forming a vortex is mainly given by the kinetic energy of the particles circulating the core, given by [22]

$$E_v = \int \frac{1}{2} \rho v^2 d\mathbf{r} = \pi l \rho n_v^2 \left(\frac{\hbar}{m} \right)^2 \ln \left(\frac{R_\perp}{\xi} \right) \quad (6.1.6)$$

where ρ describes the local mass density and we integrated over a hollow cylinder with length l , inner radius ξ (corresponds to the radius of the vortex core) and outer radius R_\perp around the vortex line. When doing this rotation the fluid constituents hold an angular momentum

$$\mathbf{L} = \int \rho v r d\mathbf{r} = \pi l \rho n_v \left(\frac{\hbar}{m} \right) R_\perp^2 \quad (6.1.7)$$

where the integration was performed again over a cylinder with length l and radius R_\perp . In a rotating system vortex creation gets energetically favourable when $E - \boldsymbol{\Omega} \cdot \mathbf{L} < 0$ or respectively when the angular velocity exceeds the critical threshold value

$$\Omega_{c,\text{hom}} = \frac{E_v}{|\mathbf{L}|} = \frac{\hbar}{m R_\perp^2} n_v \ln \left(\frac{R_\perp}{\xi} \right) \stackrel{n_v=1}{=} \frac{\hbar}{m R_\perp^2} \ln \left(\frac{R_\perp}{\xi} \right) . \quad (6.1.8)$$

In the last step we set the vortex charge n_v to 1, because only these ones are stable. This can be illustrated by the scaling behaviours of the vortex energy E_v (scaling with n_v^2) and the particle momentum L (scaling with n_v), making vortex creation for higher charges highly energetically undesirable.

Vortices in trapped superfluids

Of course a homogeneous superfluid is a highly idealised system that would require the medium to possess infinite extend. Superfluids in atomic physics are typically trapped to a close region in space, making them clearly inhomogeneous. Therefore the previous results need to be extended in order to describe our dipolar Bose-Einstein condensate in a satisfying way. The trapping primarily creates a space-dependency in the density distribution $n_0 \rightarrow n_0(\mathbf{r})$ that needs to be considered in the derivations shown above. We do not wish to repeat the full calculations again but will focus on the most relevant results. For a more detailed derivation we refer again to the sources mentioned in the beginning.

The so called "healing-length" ξ is defined as the distance around the core where the kinetic and interaction energy balance each other [60] ($E_{\text{kin}} = E_{\text{WW}}$). The intuitive name origins from the visual picture that the condensate has "healed" its defect in form of the vortex core at this distance. This can be shown to be at

$$\xi = \frac{\hbar}{\sqrt{m n_0 g}} = \frac{1}{\sqrt{4\pi n_0 a_s}} \quad (6.1.9)$$

for a purely contact interacting BEC, with a_s the background scattering length and n_0 the peak density in the absence of the vortex. With this we receive the final version of the critical frequency for stable vortex creation in a purely contact-interacting system in the form of

$$\Omega_{\text{c,trap}} = \frac{5}{2} \frac{\hbar}{m R_{\perp}^2} \ln(\sqrt{4\pi n_0 a_s} R_{\perp}) \quad (6.1.10)$$

scaling with the condensates density and scattering length.

This relation will most probably not result in a perfect description of our strongly dipolar Dysprosium condensate, as anisotropic dipolar influences are not taken into account.

As an exact derivation of the critical frequency in dipolar systems is not known yet, we will still use this equation as a rough guide while keeping in mind that, especially for strong dipole-tilts, the healing-length and therefore the critical frequency will most likely be significantly modified. This modification is expected to create an anisotropy in the density distribution around the vortex cores, increasing the density in the direction of the magnetic field and reducing it orthogonal to it [71]. Further it has been predicted that vortex lattices that typically hold a triangular Abrikosov formation under isotropic conditions [65] might change to linear lines [64] or even more peculiar patterns [40].

6.2 Vortex Creation

After having discussed the basic theory, it is time to take a look at the specifications of the vortex creation procedure in our simulations.

This section intends to offer insights into the process for vortex formation in a cylindrically symmetric ^{164}Dy Bose-Einstein condensate and the critical stirring frequency threshold in the case of an attractive as well as a repulsive potential that is used to stir the condensate.

6.2.1 Forming Mechansims

Vortices have been generated by other experiments in the past via laser stirring [37,63] in order to introduce angular momentum to the system.

The first problem when it comes to stirring a condensate for the creation of excitations like vortices, is to find a working parameter space for the relevant degrees of freedom in trapping and stirrer details. After some experimenting it became clear that slightly oblate clouds with a trap aspect ratio of around $\kappa = f_z/f_r \approx 10 - 15$ seem to be promising candidates for our simulations. The condensate discussed in the following is trapped accordingly in a trap with trap frequencies of $f_{x,y} = 40$ Hz and $f_z = 500$ Hz, which is equivalent to a trap aspect ratio of $\kappa = 12.5$.

Figure 23 presents different intermediate stages during an exemplary stirring process between an undisturbed ^{164}Dy condensate out of 4,000 atoms and the resulting vortex lattice after stirring and an additional formation time. At this point we are not yet interested in the influences of the anisotropic dipole-dipole interaction of the magnetic Dysprosium atoms. While still including it into the simulations, for now we choose a magnetic field pointing out of the BEC plane and therefore an isotropic dipolar interaction in the BEC plane. Additionally to the density distribution, the respective phase is depicted to verify that the forming holes in the condensate are real vortices and not just random density variations. Following the discussions in the previous chapter the phase around a vortex core varies by 2π , making the phase distribution a clear indicator for the presence of a vortex. The stirring is performed by two Gaussian laser beams with a distance of $R = 2 \mu\text{m}$ to the cloud center, each possessing a beam waist of $w_0 = 1 \mu\text{m}$ as well as an individual power of up to $P_{\text{max}} = 1 \mu\text{W}$ and rotate around the cloud center with a frequency of $f = 50$ Hz.

The process starts with the ground state of the dipolar condensate after imaginary time evolution of an original Gaussian density distribution shown in figure 23 at t_0 . Then the two laser beams start to rotate, while their power is ramped up linearly from zero to $P_{\text{max}} = 1 \mu\text{W}$ over $t_{\text{ramp}} = 10$ ms, followed by $t_{\text{stir}} = 300$ ms of stirring and a down ramping over t_{ramp} . The density and phase of the cloud is shown in figure 23 at the beginning of the stirring procedure (t_1), in the middle (t_2) and at the end (t_3).

It is visible that the condensate particles get attracted into the two laser beam spots in the beginning (t_1). Then they form interesting density symmetries during the stirring process, probably caused by the atoms not being able to follow the beams quick enough, therefore leaving the laser spots and getting reabsorbed multiple times over the stirring cycles (t_2). In the end, shortly before ramping down the power of the stirring beams, the cloud seems to be completely disordered (t_3).

Because the simulations do not contain any energy dissipation and conserve the number of particles, the atoms can not leave the trap. In a real experiment this is the point where a high number of particles would probably be lost, illustrating the main reason why vortex creation through stirring is highly difficult to perform under realistic experimental conditions and why we mainly fall back on idealised simulation procedures. After the laser beams are deactivated, the condensate is given several seconds of free evolution time in order to rethermalize and form vortices.

The first vortices become visible about 400 ms after the end of stirring when the particles start to form a coherent cloud again (t_4). Further time steps are depicted after 1 s (t_5), 3 s (t_6) and 5 s (t_7) of overall simulation time, illustrating how the condensate stabilizes again,

resulting in an improved contrast and a better visibility of the vortex cores.

It is worth highlighting that the number of vortices seems to be determined relatively shortly after the first ones become visible (between t_4 and t_5) and is preserved thereafter. This behaviour was observed in all simulations containing vortex creation and underlines that the process of forming a vortex can only happen during the chaotically swirled state of the condensate where the particles stabilize into a collective cloud. The vortex number does not change later on, as a certain amount of angular momentum is necessary to create them and after the stirring procedure the amount of angular momentum in the system is conserved.

The fact that the number of created vortex cores shows to be determined after a relatively short free evolution time of a few hundred milliseconds enables the reduction in overall simulation time. Still this duration, being in the order of 1 s might prove problematic under realistic experimental conditions. Typical lifetimes of vortices have been shown [62, 78] to be of comparable size, making the creation of vortex lattices quite difficult.

The results discussed in the following sections will all arise from simulations containing a stirring time of $t_{\text{stir}} = 300$ ms and a free evolution time of 1 s (between t_5 and t_6). At this point the qualitative vortex formation is clearly visible and further evolution time brings no additional information.

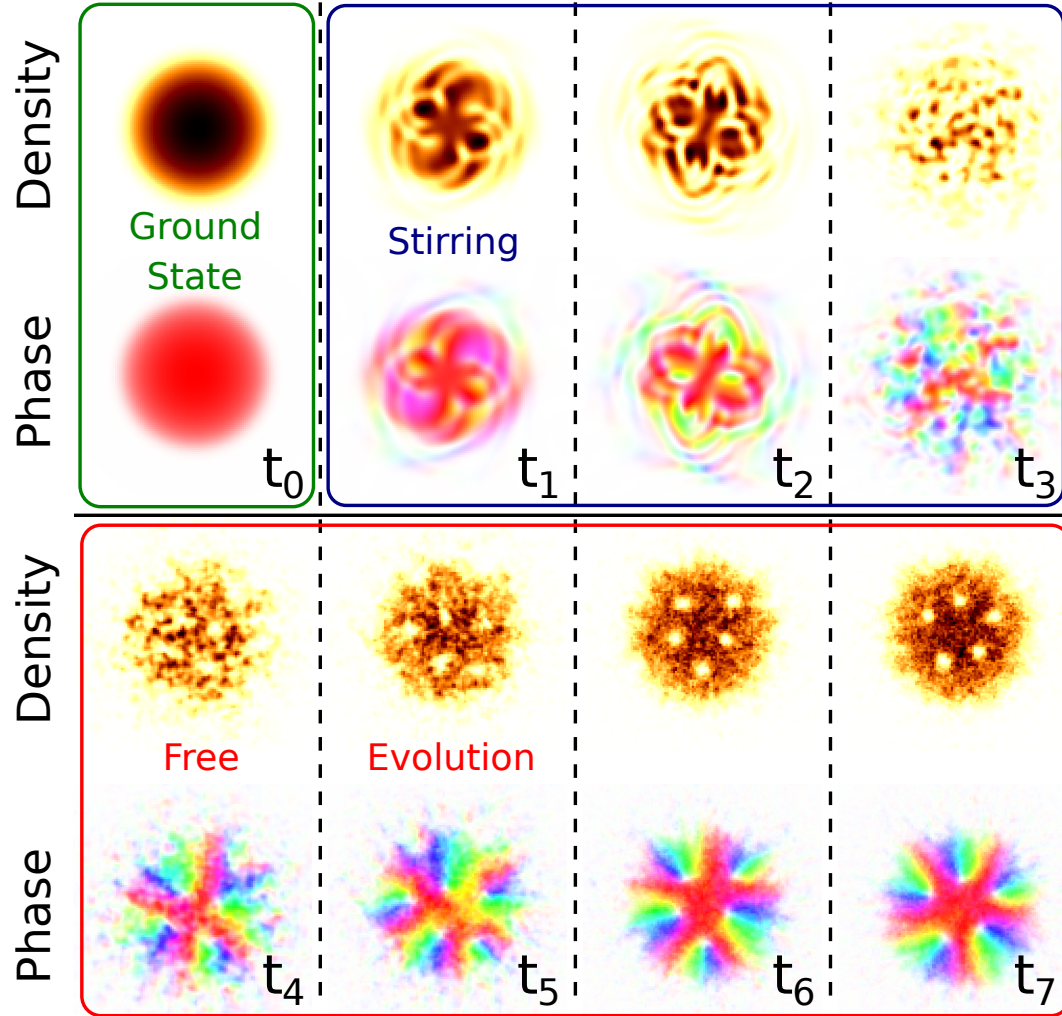


Figure 23: Density and phase plots of a simulated ^{164}Dy condensate out of 4,000 atoms during stirring with two Gaussian laser beams at a distance of $R = 2\ \mu\text{m}$ to the center with a frequency of $f = 50\ \text{Hz}$ at different times t_0 - t_7 . The beam waist of this stirrers is $w_0 = 1\ \mu\text{m}$ and the power ramped up to $P_{\text{max}} = 1\ \mu\text{W}$. We are starting with the the ground state of the cloud after imaginary time evolution without any stirrer influences at t_0 (green box). Then the condensate gets stirred for $t_{\text{stir}} = 300\ \text{ms}$. Here the cloud condition is shown at the beginning (t_1), in the middle of the stirring procedure (t_2) and at the end (t_3) (blue box). Finally we apply a free evolution time to allow the condensate to rethermalize and create vortices. Different stages of this vortex formation are presented with the first appearing vortices after around 700 ms (t_4 followed by the cloud consolidating after 1 s (t_5), 3 s (t_6) and 5 s (t_7) (red box).

6.2.2 Critical Frequency

When trying to create vortices through stirring of a superfluid, a certain critical stirring frequency needs to be exceeded, as was discussed in section 6.1.

In figure 24 the simulated density and phase distribution of a ^{164}Dy condensate under similar conditions as in the previous section is shown for stirring with attractive and repulsive beams at different velocities f . For our qualitative discussions we ignore that the potential depth of the beam would theoretically depend on the polarizability of Dysprosium to the respective wavelength and just assume an identical potential depth for attractive and repulsive beams, enabling us to just switch the sign ($V_{\text{attr}} = -V_{\text{rep}}$). The condensate is trapped in a highly oblate form with trap frequencies of $f_{x,y} = 40 \text{ Hz}$ and $f_z = 500 \text{ Hz}$.

Figure 24 reveals two relevant characteristics of the vortex creation mechanism through stirring. First of all, when increasing the stirring frequency, the first vortex gets created at roughly the critical frequency and more and more vortices tend to appear when even further accelerating the stirring. The fact that the creation does not start exactly at the critical frequency corresponding to conditions at the center of the condensate is the density scaling of this critical frequency following equation (6.1.10). It reduces with the density, therefore vortices are expected to be first created at the edges of the condensate where the local critical rotation frequency might be lower than in the center.

When comparing attractive and repulsive stirrers with identical potential depth, it is apparent that the repulsive beams always generate more or at least the same amount of vortices as their attractive counterparts. This behaviour is well known [37] and can be understood through the density dependence of the critical frequency in equation (6.1.10). The repulsive laser beams reduce the local density around them, what then again reduces the local critical frequency, simplifying the creation of vortices.

This tendency was the motivation for us to build a 405 nm laser setup, as discussed in detail in chapter 3.3, a wavelength forming a repulsive potential for Dysprosium atoms.

Calculating the theoretical critical rotation frequency following equation (6.1.10) with the following parameters of our system ($n_0 \approx 10^{20} \text{ 1/m}^{-3}$, $R_{\perp} \approx 4 \mu\text{m}$) results in a value of $f_c = \omega_c / (2\pi) = 83.97 \text{ Hz}$ at the center of the condensate, which is significantly higher than the one we are experiencing in figure 24. Due to the density and therefore critical frequency reducing against the edges, this is an understandable result.

Overall it could be shown that repulsive stirrers are more efficient in vortex creation than attractive ones and that even stirring below the critical frequency allows vortex creation in off-center positions with lower density.

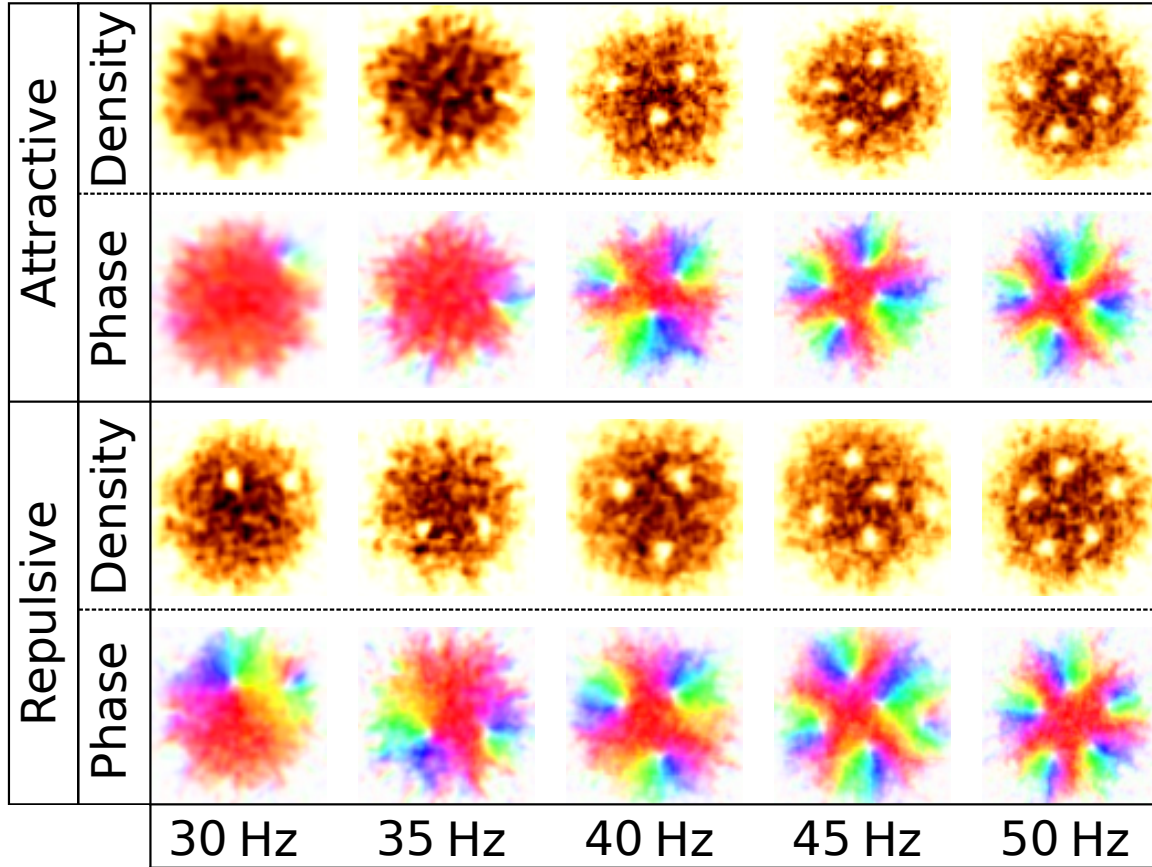


Figure 24: Density and phase plots of a simulated ^{164}Dy condensate out of 4,000 atoms after stirring with two Gaussian laser beams at a distance of $R = 2\ \mu\text{m}$ to the center under variation of the stirring frequency. The beam waist of the stirring beams is fixed at $w_0 = 1\ \mu\text{m}$ and the maximal power after ramping up is chosen to be $P_{\text{max}} = 1\ \mu\text{W}$. The resulting vortex configuration after 300 ms of stirring and 1 s of free evolution time is depicted for different stirring frequencies when using either an attractive or a repulsive laser beam. In all shown cases the dipoles are aligned out of the condensate plane ($\alpha = 0^\circ$), making the DDI isotropic.

6.3 Influence of Anisotropic Trapping

Our simulations about the creation and behaviour of vortices should, apart from the basic question whether their creation is possible at all, also provide insights into possible challenges for later experimental verifications. In a realistic experiment the parameters of a system are seldom exactly known, but feature small deviations from the desired value, due to measurement inaccuracies and other experimental difficulties.

A good example of these properties are the exact trap frequencies, having a significant impact on the density distribution and therefore overall shape of the investigated condensate. Over time the exact value of the trap frequencies can drift noticeably, motivating us to explore the influence of resulting anisotropies in the cloud.

In figure 25 the resulting vortex configuration for different radial trap frequency combinations are shown, ranging from an isotropic configuration with $f_{x,y} = 40$ Hz to increasingly anisotropic conditions up to $f_x = 37$ Hz and $f_y = 43$ Hz.

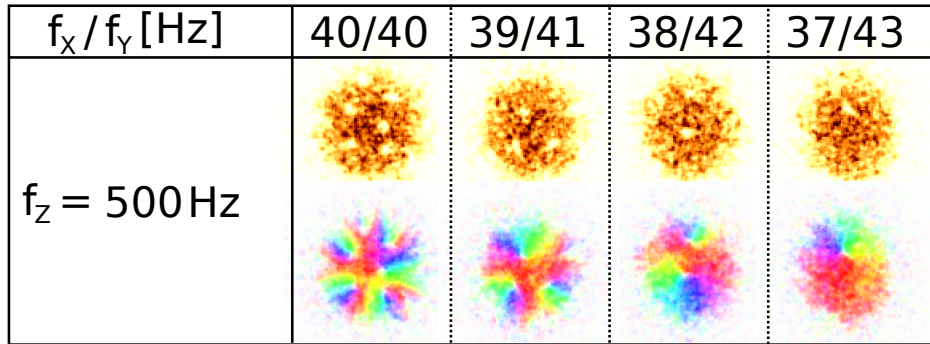


Figure 25: Density distribution of a ^{164}Dy condensate of 4,000 atoms, trapped under varying trapping conditions after 300 ms of stirring and 1 s of free evolution time. We are stirring with two repulsive laser beams with beam waist $w_0 = 1.5\mu\text{m}$, rotating them around the cloud center with at a distance $R = 2\mu$ with a frequency $f_{\text{stir}} = 50$ Hz. The vertical trap frequency is fixed to $f_z = 500$ Hz and the radial trap frequencies are varied, starting from the isotropic case $f_{x,y} = 40$ Hz and increasing the anisotropy from left to right.

Comparing the resulting vortex formations reveals that isotropic radial conditions enable the highest number of vortices, in our case 6 visible ones. The more anisotropic the system becomes, the less vortices seem to form. In figure 26 the radial trap frequencies are fixed to $f_{x,y} = 40$ Hz, forming radially symmetric conditions, and we vary the vertical trap frequency f_z .

Starting with $f_z = 300$ Hz, 7.5 times the radial counterparts, the number of created vortices after the stirring process reduces with increasing entrapment, going down from seven to only two visible vortices for $f_z = 1000$ Hz.

This can be understood when considering equation (6.1.10). Increasing the vertical trap frequency while holding its radial counterparts constant increases the density in the condensate, leading to a higher critical frequency and therefore a reduction in the number of created vortices.

Our results, especially in figure 25, highlight the problem that even relatively small deviations in the radial trap frequencies can result in a drastic reduction in vortex creation

efficiency. Therefore when trying to verify this results under experimental conditions one would have to invest some time to carefully calibrate the exact trapping parameters. Regarding the vertical trap frequency, the creation mechanism seems to be more robust, as variations in the order of hundred Hertz are necessary to reduce the vortex number in our example due to an increase in the density and therefore higher necessary frequencies.

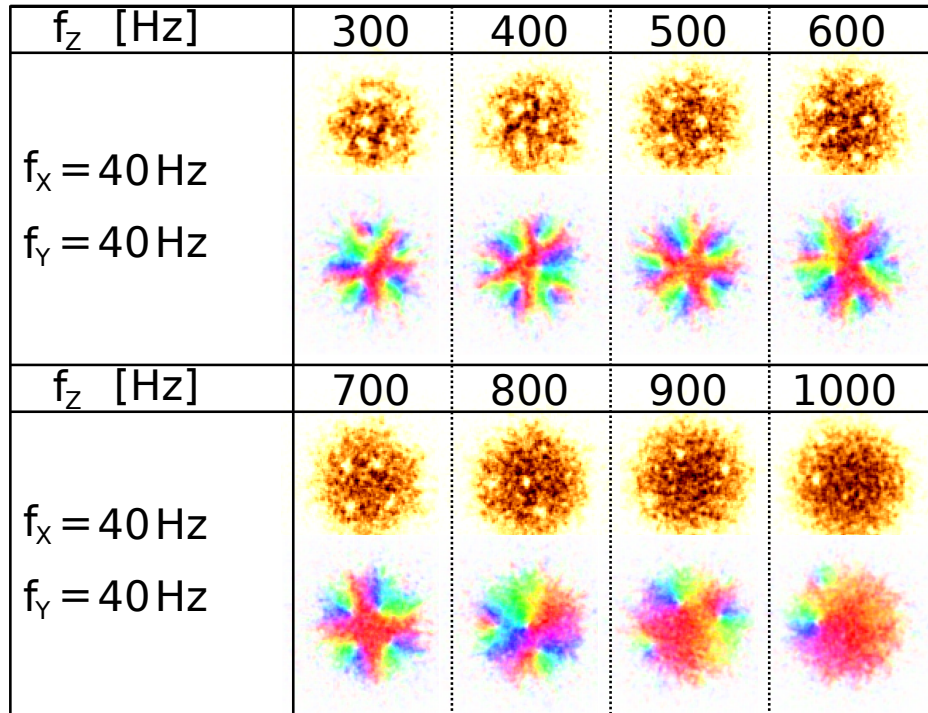


Figure 26: Identical conditions to figure 25 but here the radial trap frequencies are fixed to symmetric conditions of $f_{x,y} = 40$ Hz and the vertical trap frequency is varied from 300 to 1000 Hz.

6.4 Vortices at Tilted Magnetic Fields

As it was shown on multiple occasions over the course of this thesis, the significant advantage of Dysprosium, compared to other materials, is its high magnetic moment and therefore a strong dependence of its macroscopic behaviour from the dipole alignment of its constituents. In this section the influence of an external magnetic field, aligning all the microscopic dipoles, on the creation of vortices and their arrangement shall be investigated.

6.4.1 Static solutions

For the creation of vortices, angular momentum needs to be added to a superfluid state, in the following case a ^{162}Dy condensate with 10,000 atoms in a trap with $f_x = 40$ Hz, $f_y = 40$ Hz and $f_z = 500$ Hz and dipoles aligned along the angle α as shown in figure 27. Apart from the relatively complex procedure of stirring inside the condensate, numerical simulations allow us to add angular momentum directly. Theoretically this is equivalent to switching into the reference frame of a condensate rotating with the angular frequency ω around its center. The resulting Hamiltonian in this frame H' is equivalent to the original one in the system of rest H reduced by the rotation energy $N \mathbf{L} \boldsymbol{\omega}$ where it is assumed that all particles possess an angular momentum of \mathbf{L} .

$$H' = H - N \mathbf{L} \boldsymbol{\omega} = H - 2\pi N |\mathbf{L}_z| f \quad (6.4.1)$$

As vortices with constituents possessing an angular momentum bigger than \hbar are unstable, as was discussed in section 6.1, \mathbf{L} will be chosen accordingly to $\mathbf{L} = L_z \cdot \hat{\mathbf{e}}_z = 1 \hbar \cdot \hat{\mathbf{e}}_z$.

Applying imaginary time evolution with the Hamiltonian 6.4.1 results then in the ground state of the system rotating with frequency f . For a rotation frequency of 15 Hz the ground states under all shown angles do not contain any vortices, showing that in this situation the critical frequency for vortex creation is not reached. At $f = 20$ Hz the isotropic case of $\alpha = 0^\circ$ possesses a vortex lattice as its ground state, which however changes with an increased dipole tilt. As was mentioned in section 6.1, a complete theoretical model describing dipolar influences on vortex creation has not been developed yet, forcing us to rely on qualitative discussions of the observed effect. As can be seen in general in figure 27, the number of created vortices reduces when increasing the field tilt. There are two possible ways to explain that following previous results in this chapter.

First of all, dipolar effects create an anisotropy in the condensates density distribution, comparable to the effects of an anisotropic trap. A significant reduction in vortex creation efficiency has already been observed there and will probably transfer to this system.

Secondly, dipolar interactions tend to decrease the size of the cloud, increasing the density around the center area, which, following equation (6.1.10) increases the critical frequency for vortex creation and therefore reduces the number of vortices.

Of special interest is the alignment of the created vortices. While vortices under isotropic conditions tend to arrange themselves in an Abrikosov lattice [65], they form vortex lines along the dipole projection when the system becomes increasingly anisotropic, as was already predicted by [64]. When taking a close look at the shape of the vortex cores in figure 27, it becomes visible that the core-size increases from the center to the edges. This

behaviour has already been predicted in equation (6.1.9) when considering that the density reduces outwards. We could not observe this for the stirring results before, as the contrast there was drastically worse. Further the form of the vortex cores can be seen to change when going to higher tilt angles. In the radially isotropic case ($\alpha = 0^\circ$), the core is round but gets more and more elongated for higher tilt angles. This is a theoretically known behaviour, discussed in detail for example in [71].

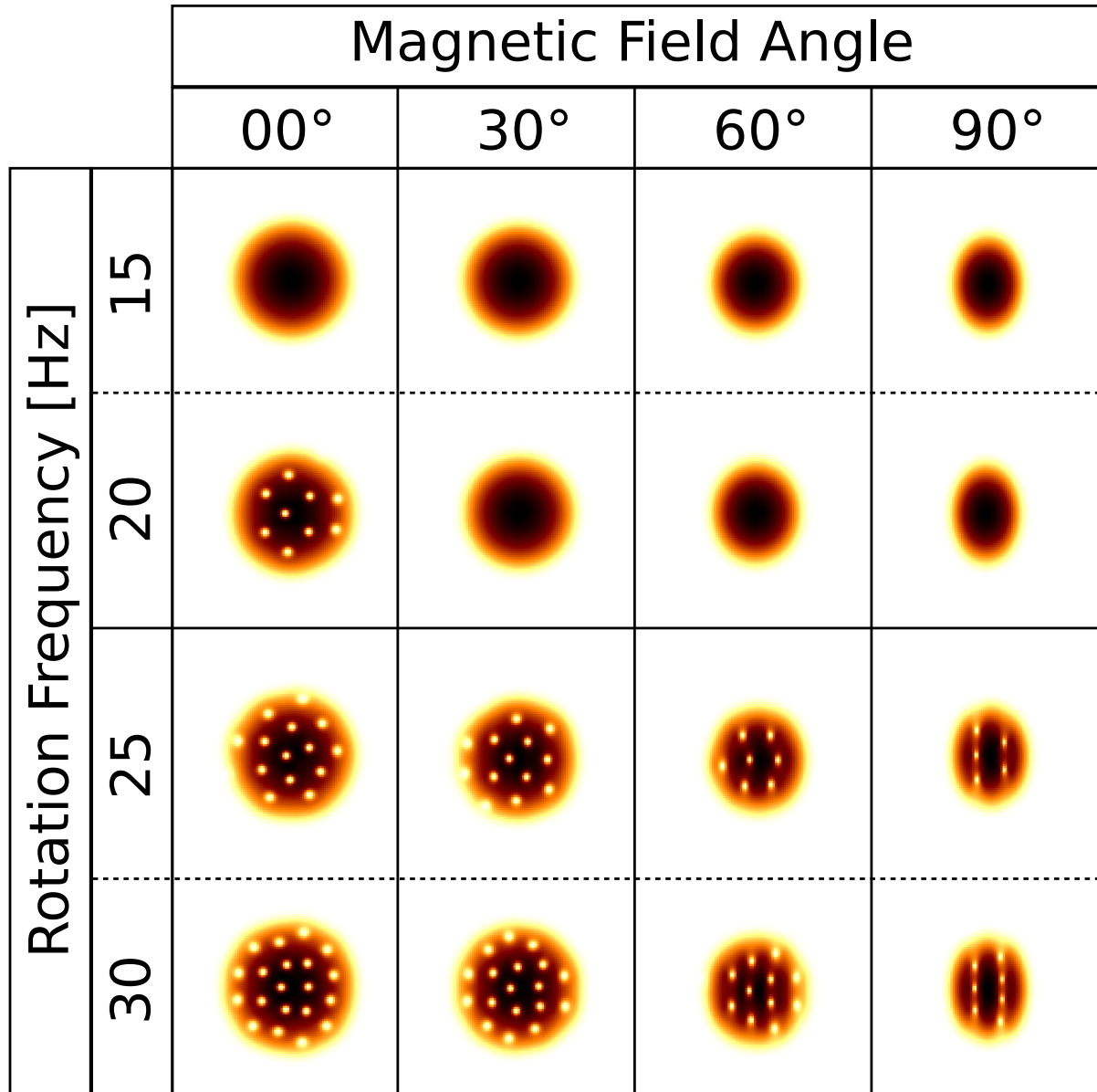


Figure 27: Ground states of a ^{162}Dy condensate of 10,000 atoms, trapped with $f_x = 40$ Hz, $f_y = 40$ Hz and $f_z = 500$ Hz, when rotated with a frequency f and the particle dipoles oriented along an angle α . A reduction in the number of created vortices for higher magnetic field angles and a change in their alignment from a triangular to a linear alignment can be observed. Further the vortex core size increases from center to the edges of the condensate and the core gets elongated along the dipole-orientation.

6.4.2 Dynamic solutions

Even though rotating the whole condensate, as it was theoretically performed in the last section, results in very well pronounced vortex lattices, it is practically very challenging to perform such a procedure under realistic conditions in our setup. Therefore we will come back to the more feasible way of circular stirring and check whether the results presented in the last section could be reproduced for parameters accessible with our experimental setup.

In figure 28 the density and phase distributions for simulated ^{162}Dy condensates out of 20,000 atoms trapped with $f_x = 40$ Hz, $f_y = 40$ Hz and $f_z = 500$ Hz when stirring with different frequencies f under magnetic field angles α between 0° and 90° .

In the figure, the conditions below (upper two rows) and above (lower two rows) the critical frequency threshold are compared. Using equation (6.1.10) to determine the critical rotation frequency for vortex creation with the parameters of our condensate ($n_0 \approx 1.2 \cdot 10^{20} \text{ m}^{-3}$ and $R_\perp \approx 5 \mu\text{m}$) results in $f_c = \omega_c / (2\pi) = 55.0$ Hz for the central position of the cloud. Again vortex creation can be observed below this threshold, but mostly with some distance to the center, where the local density and therefore the local critical frequency is reduced. In contrast to the ground state results in the last section the vortex core size does not significantly change between central and outer regions and an alignment in linear lines is only visible with much good will, as the vortex number overall and especially in the tilted clouds is reduced compared to the static ground state solutions. The conservation of the core size might possibly be caused by the vortices being formed in the outer regions before distributing themselves. The shape variations in form of elongations of the core along the magnetic field are visible similar to the ground state results.

Summarising this section we reproduce fundamental vortex behaviours, known from the ground state solutions in the last section, in a dynamical system via laser stirring for parameters that are roughly in the accessible region for our experimental setup. Apart from a significantly lower vortex number, especially in the inhomogeneous clouds, the vortex core size seems to vary significantly less in the same cloud compared to the ground state solutions.

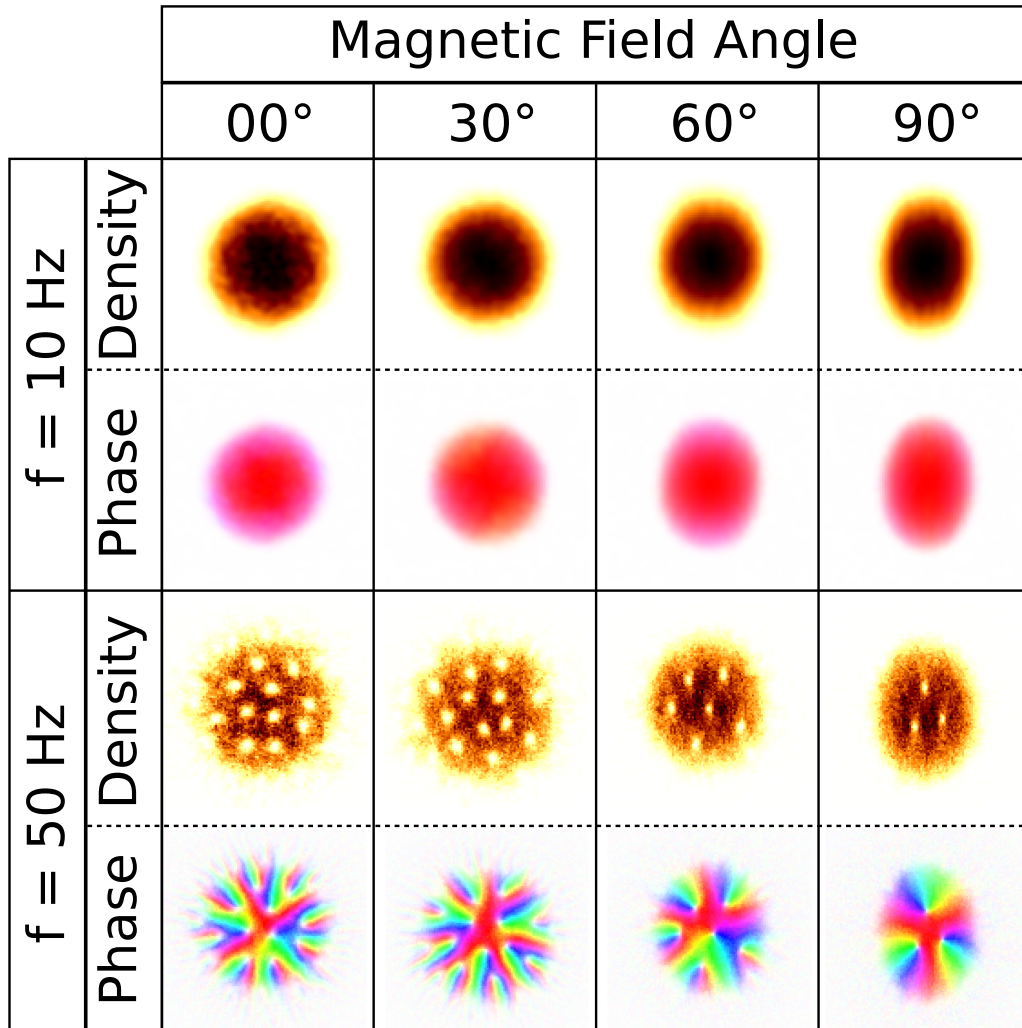


Figure 28: Density and phase of dynamic vortex states given by a ^{162}Dy condensate of 20,000 atoms, trapped with $f_x = 40$ Hz, $f_y = 40$ Hz and $f_z = 500$ Hz, when rotated by a frequency f with the particle dipoles oriented along an angle α given by the first row. Above a certain rotation frequency threshold vortices start to form. The number of creates cores reduces significantly for higher magnetic field tilt angles and the vortex core becomes elongated. Surprisingly, the variations in the core size inside the same cloud are drastically less pronounced than they were in the ground state solutions in figure 27

7 Conclusion and Outlook

The aspiration of the work presented in this thesis was to gain insights into the behaviour of a superfluid system consisting of highly dipolar constituents. For this purpose we investigated the breakdown of superfluidity and the creation of vortices in ^{162}Dy and ^{164}Dy Bose-Einstein condensates through linear and circular stirring with laser beams.

When the flow inside of a superfluid exceeds a certain velocity threshold, dissipation arises and the superfluid state breaks down. This behaviour was first theoretically explained by Lev Landau in 1941 through the creation of quasiparticles in the medium. Therefore the critical, or "Landau", velocity can be determined from the knowledge of the systems dispersion relation, connecting in a remarkable way microscopic and macroscopic properties of the superfluid.

In order to determine the critical velocity for our system we stirred the Dysprosium condensate using a 532 nm laser beam with different velocities and measured the resulting heating behaviour. Comparing the results of the experiment with full numerical simulations yielded an astonishing agreement. By fitting a bilinear function onto the heating the critical velocity could then be identified.

It was verified experimentally and numerically that the critical velocity in a Dysprosium BEC can be manipulated by an outer magnetic field aligning the atomic dipoles, allowing to achieve different critical velocity thresholds parallel and orthogonal to the projection of the dipoles. This splitting is not caused by a pure density modification through magnetostriction and the exact value of the critical velocity could be altered by changing the cloud shape, as well as certain parameters of the stirring procedures.

This represents the first experimental proof of the theoretically predicted anisotropy in the critical velocity of a dipolar superfluid.

The qualitative behaviour of the condensates heating under variation of different trap and stirring parameters has been studied through further numerical simulations. It could be shown that stirring multiple times along the same path through the condensate creates an approximately linear increase in heating in the simulations. Tilting the magnetic field inside the condensate plane, the critical velocity increases in the parallel and stays roughly constant in the orthogonal direction, what could be shown to be in agreement with the theory for the speed of sound in a homogeneous Bose-Einstein condensate. Further the overall heating reduces with the field tilt. Stirring with different angles through the anisotropic system resulted in a monotonous decrease in the dissipation threshold from a parallel to an orthogonal stirring direction. When increasing the stirring amplitude, the overall heating increases and the heating maximum moves to higher velocities. Bigger stirring beams increased the heating but reduced the critical velocity. Variations in the potential depth also increased the overall amount of created heating. As the exact background scattering length of ^{162}Dy is unknown, we varied this parameter in our last linear stirring simulation and compared the resulting heating to experimental measurements. Through this we were able to narrow the scattering length down to a region between $121 a_0 < a_s^{\text{Dy},162} < 161 a_0$ which is in good agreement with the different results published by the Stanford group of Benjamin Lev.

In the second part of this thesis the influence of dipolar interactions on vortex creation and lattice arrangement was evaluated.

We started by verifying that our simulations were able to allow the creation of vortices

by stirring with two identical laser beams circularly around the condensate center. After finding the correct parameter space it could be shown that vortex formation requires a free evolution time after the stirring procedure, in order to allow the condensate to rethermalize. Examining this creation procedure in detail revealed that a stirring time of $t_{\text{stir}} = 300$ ms and a free evolution time of $t_{\text{evo}} = 400$ ms tended, depending on the exact system parameters, to be the minimum duration for a successful vortex excitation.

The critical rotation frequency of the stirrers was investigated with the simulation results being in accordance with theoretical estimations. Variations in the trap frequencies revealed a noticeable decline in vortex creation when the system becomes inhomogeneous in relation to both horizontal, and to a lesser degree to the vertical, trapping direction, what might raise challenges in experimental verifications of our numerical results.

In the end the dipoles were tilted inside the condensate plane and the resulting influence on vortex creation investigated. The ground state of a rotating condensate could be shown to be able to possess vortices under tilted conditions, even though their number decreased and higher rotation frequencies were necessary to create them when tilting the magnetic field. It could further be shown that vortices change their relative arrangement from a triangular Abrikosov-lattice to linear vortex lines along the projection of the tilted dipoles. These behaviours were observed again in a dynamic system when circularly stirring the condensate with two Gaussian laser beams.

Outlook

All the investigations on the vortex behaviour presented in this thesis were based on numerical simulations. The necessary modifications in the experimental setup for their realisation have already been performed during the course of this thesis, through the implementation and full alignment of a 405 nm laser beam path through the EOD system. Using the ^{162}Dy isotope in our condensate has already been shown to result in bigger condensates than its ^{164}Dy counterpart, what could enable the experimental verification of our simulation results.

Of further interest is the exact arrangement of the vortex lattice under more sophisticated conditions. We could already show a linear lattice alignment along the dipole-tilt projection, but under certain conditions even more interesting lattice patterns have been predicted [65] and should be realisable in our simulations and hopefully in the experiment. Especially interesting is the behaviour of a ^{162}Dy - ^{164}Dy mixture when it comes to superfluid properties. As we could show in section 5.3.7 the heating behaviour significantly depends on the background scattering length. It would be interesting to explore how the critical velocity, as well as the critical rotation frequency for vortex creation and the resulting vortex lattice formation would behave. At least for the latter point theoretical predictions exist [66] and promise interesting observations.

A Appendix

A.1 Speed of Sound in a strongly trapped Dipolar Gas and Roton excitation

A homogeneous condensate certainly is a highly idealised system, not easily realisable. The other extreme case is a strongly trapped, and therefore inhomogeneous, Bose Einstein condensate. An additional positive side-effect of a BEC highly compressed in the dipole direction is the avoidance of the phonon-instability collapse, discussed in the context of the homogeneous three-dimensional case. By a strong enough confinement in the magnetization direction (here and later arbitrarily chosen to be the z -direction) meaning that the trapping potential has to exceed the chemical potential ($= n_0(g + 2g_{dd}) \gg \hbar\omega_z$), the density distribution and therefore the wavefunction can be restricted to the ground state of the harmonic oscillator. As a consequence, excitations in this direction will be exponentially suppressed, preventing a heavy phonon mode propagation and thus the collapse. The new quasi-2D-system makes an adaption of the dispersion relation 2.4.1 necessary, resulting in [20]

$$\omega(\mathbf{k}, \alpha, \eta) = k \sqrt{\frac{\hbar^2 k^2}{4m^2} + \frac{gn_0}{m} [1 - \epsilon_{dd} F(\mathbf{k}, \alpha, \eta)]} \quad (\text{A.1.1})$$

with

$$F(\mathbf{k}, \alpha, \eta) = \cos^2(\alpha) \left(-2 + 3\sqrt{\pi} k e^{k^2} \text{Erfc}(k) \right) + \sin^2(\alpha) \left(1 - 3\sqrt{\pi} k \cos^2(\eta) e^{k^2} \text{Erfc}(k) \right). \quad (\text{A.1.2})$$

Here k describes the absolute value of the wavevector \mathbf{k} , α again depicts the angle between \mathbf{k} , $\mathbf{\mu}_m$, and η is the angle of propagation inside the condensate plane and $\text{Erfc}(k)$ describes the complementary error function. Comparing this dispersion relation for the trapped system (equation A.1.1) with the one for a three dimensional homogeneous system (equation 2.4.1) reveals a similar structure, but a difference in the dipolar dependency. The quasi-2D-system reveals an anisotropy in the dipolar contribution dependent on the wavevector k , as is obvious from equation A.1.2. This contribution monotonously decreases with k . Figure 29 shows the dispersion relation (a,c,e) and the corresponding speed of sound (b,d,f) in dependence of the stirring angle η for different orientations of the magnetic field. If the dipoles are aligned orthogonal to the BEC-plane ($\alpha = 00^\circ$) and therefore creating an isotropic interaction strength in the condensate, the speed of sound is identical in all horizontal directions (a,b). When tilting the dipoles, the dispersion relation splits up for different stirring directions, creating anisotropy in the sound velocity that is nearly unchanged along the dipole-tilt and drastically decreased orthogonal to it (c,d). Should the magnetic field to fully tilted inside the plane ($\alpha = 90^\circ$), the split in the dispersion relation reaches its maximum, while the speed of sound following equation 2.4.3 gets surprisingly identical in all directions.

Even though the stability problem is changed, compared to the three dimensional case, it has not totally vanished. Equation A.1.1 still holds the possibility of imaginary solutions

for $g + 2g_{\text{ad}} < 0$. A second instability problem arises from the momentum dependence in A.1.2, enabling a local energy minimum for finite momenta. The quasi-particles related to this minimum are called "rotons", and their energetic minimum "roton minimum". If the local maximum beforehand is also taken into account, enabling a "maxon", the whole spectrum is typically called "roton-maxon spectrum"[21].

Similarly to the phonon instability, the collapse mechanism sets in, when the energy of the roton minimum reaches zero, making it energetically favorable to occupy this mode macroscopically, while the difference lies in the fact that this minimum exists at a finite momentum, meaning that the corresponding instability shows a characteristic roton length scale.

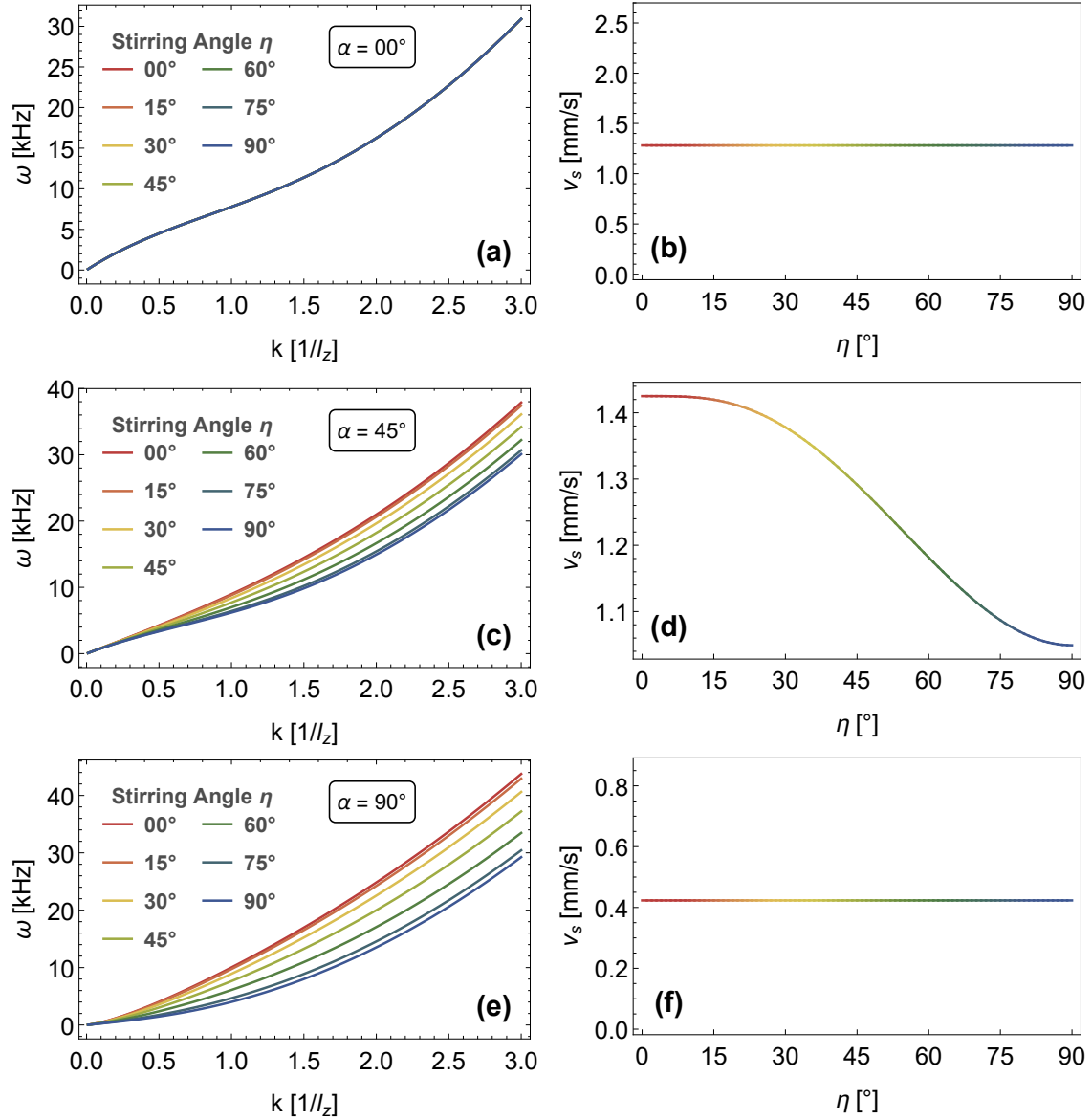


Figure 29: Dispersion relation ((a),(c),(e)), following equations A.1.1, and corresponding speed of sound ((b),(d),(f)), for a ^{162}Dy Bose-Einstein condensate under different magnetic field angles α . An atomic density of $n_0 = 2 \cdot 10^{20} \text{ m}^{-3}$ is assumed, comparable to the central density in the regime of our experimental and simulated results shown in later parts of this thesis.

B Bibliography

References

- [1] S. Bose, Plancks Gesetz und Lichtquantenhypothese, *Zeitschrift für Physik*, 26, 178-181 (1924)
- [2] A. Einstein, Quantentheorie des einatomigen idealen Gases, *Sitzungsbericht der Preussischen Akademie der Wissenschaften*, pages 261-267 (1924)
- [3] A. Einstein, Quantentheorie des einatomigen idealen Gases, 2. Abhandlung. *Sitzungsbericht der Preussischen Akademie der Wissenschaften*, pages 3-14 (1925)
- [4] M. H. Anderson, J. R. Ensher, M. R. Matthews, C. E. Wieman, and E. A. Cornell, "Observation of Bose-Einstein condensation in a dilute atomic vapor", *Science* 269, 198 (1995).
- [5] W. Ketterle, D. S. Durfee and D. M. Stamper-Kurn, Making, probing and understanding Bose-Einstein condensates, *arXiv:cond-mat:9904034* (1999)
- [6] A. Griesmaier, J. Werner, S. Hensler, J. Stuhler and T. Pfau, Bose-Einstein Condensation of Chromium, *Phys. Rev. Lett.*, 94, 160401 (2005)
- [7] K. Aikawa, A. Frisch, M. Mark, S. Baier, A. Rietzler, R. Grimm and F. Ferlaino, Bose-Einstein Condensation of Erbium, *Phys. Rev. Lett.*, 108, 210401 (2012)
- [8] M. Lu, N. Q. Burdick, S. H. Youn and B. L. Lev, Strongly Dipolar Bose-Einstein Condensate of Dysprosium, *Phys. Rev. Lett.*, 107, 190401 (2011)
- [9] S. Yi and L. You, Trapped condensates of atoms with dipole interactions, *Phys. Rev. A*, 63, 053607 (2001)
- [10] R. Oldziejewski and K. Jachymski, Properties of strongly dipolar Bose gases beyond the Born approximation, *Physical Review A*, 94(6), 063638 (2016)
- [11] G. Baym and C. J. Pethick, Ground-State Properties of Magnetically Trapped Bose-Condensed Rubidium Gas, *Phys. Rev. Lett.*, 76, 6-9 (1996)
- [12] F. Dalfovo, S. Giorgini, L. P. Pitaevskii and S. Stringari, Theory of Bose-Einstein condensation in trapped gases, *Rev. Mod. Phys.*, 71, 463-512 (1999).
- [13] C. Eberlei, S. Giovanazzi and D. H. J. O'Dell, Exact solution of the Thomas-Fermi equation for a trapped Bose-Einstein condensate with dipole-dipole interactions, *Phys. Rev. A*, 71, 033618 (2005)
- [14] H. Kadau, M. Schmitt, M. Wenzel, C. Wink, T. Maier, I. Ferrier-Barbut and T. Pfau, Observing the Rosensweig instability of a quantum ferrofluid, *Nature*, 520, 194-197 (2016)

- [15] I. Ferrier-Barbut, H. Kadau, M. Schmitt, M. Wenzel and T. Pfau, Observation of Quantum Droplets in a Strongly Dipolar Bose Gas, *Phys. Rev. Lett.*, 116, 215301 (2016)
- [16] T.D. Lee, K. Huang and C. N. Yang, Eigenvalues and Eigenfunctions of a Bose System of Hard Spheres and Its Low-Temperature Properties, *Phys. Rev.*, 106, 1135-1145 (1957)
- [17] N. N. Bogolyubov, On the theory of superfluidity, *J. Phys. (USSR)*, 11, 23-32 (1947)
- [18] A. R. P. Lima and A. Pelster, Beyond mean-field low-lying excitations of dipolar Bose gases, *Phys. Rev. A*, 86, 063609 (2012)
- [19] F. Wächtler and L. Santos, Quantum filaments in dipolar Bose-Einstein condensates, *Phys. Rev. A* 93, 061603 (2016)
- [20] H. Kadau, Rosensweig Instability and Droplets in a Quantum Ferrofluid of Dysprosium Atoms, Ph.D. Thesis, Universität Stuttgart (2016)
- [21] L. Santos, G. V. Shlyapnikov and M. Lewenstein, Roton-Maxon Spectrum and Stability of Trapped Dipolar Bose-Einstein Condensates, *Phys. Rev. Lett.*, 90, 250403 (2003)
- [22] L. Pitaevskii and S. Stringari, Bose-Einstein condensation and superfluidity. Vol. 164. Oxford University Press, 2016.
- [23] G. P. Volovik, The universe in a helium droplet. Vol. 117. Oxford University Press on Demand, 2003.
- [24] K. B. Davis, M. O. Mewes, M. R. Andrews, N. J. van Druten, D. S. Durfee, D. M. Kurn, and W. Ketterle, "Bose-Einstein condensation in a gas of sodium atoms", *Phys. Rev. Lett.* 75, 3969 (1995)
- [25] H. Feshbach. "Unified theory of nuclear reactions" *Annals of Physics* 5.4 : 357-390 (1958)
- [26] F. Dalfovo, S. Giorgini, L. P. Pitaevskii and S. Stringari, Theory of Bose-Einstein condensation in trapped gases, *Rev. Mod. Phys.*, 71, 463-512 (1999)
- [27] C. Eberlein, S. Giovanazzi, and D. O'Dell, Exact solution of the Thomas-Fermi equation for a trapped Bose-Einstein condensate with dipole-dipole interactions, *Physical Review A* 71.3 : 033618. (2005)
- [28] M. Chiofalo, S. Succi and M. Tosi, Ground state of trapped interacting Bose-Einstein condensates by an explicit imaginary-time algorithm, *Phys. Rev. E*, 62, 7438-7444 (2000)
- [29] A. Lima, A. Pelster, Quantum fluctuations in dipolar Bose gases. *Phys. Rev. A* 84, 041604 (2011)
- [30] I. Segal, L. Halicz and I. T. Platzner, Isotope ratio measurements of dysprosium by multiple collection inductively coupled plasma mass spectrometry, *International Journal of Mass Spectroscopy*, 216, 177-184 (2002)
- [31] Ferrier-Barbut, Igor, et al. Scissors Mode of Dipolar Quantum Droplets of Dysprosium Atoms. *Physical Review Letters* 120.16:160402 (2018)

- [32] I. Ferrier-Barbut, M. Wenzel, M. Schmitt, F. Böttcher and T. Pfau, Onset of a modulational instability in trapped dipolar Bose-Einstein condensates. *Physical Review A* 97.1:011604 (2018)
- [33] T. Maier, Interactions in a Quantum Gas of Dysprosium Atoms, Ph.D. Thesis, Universität Stuttgart (2015)
- [34] M. Wenzel, A dysprosium quantum gas in highly controllable optical traps, Universität Stuttgart(2015)
- [35] Y. Tang , W. Kao, K. Li, S. Seo, K. Mallayya, M. Rigol, S. Gopalakrishnan and B.L. Lev, Thermalization near integrability in a dipolar quantum Newton's cradle, Arxiv: 1707.07031
- [36] M. Schmitt, A Self-bound Dilute Quantum Liquid of Dysprosium Atoms, Ph.D. Thesis, Universität Stuttgart (2017)
- [37] V. P. Singh, W. Weimer, K. Morgener, J. Siegl, K. Hueck, N. Luick, H. Moritz and L. Mathey, Probing superfluidity of Bose-Einstein condensates via laser stirring. *Physical Review A* 93.2:023634 (2016)
- [38] D. Peter, Theoretical investigations of dipolar quantum gases in multi-well potentials, Universität Stuttgart (2011)
- [39] P. Muruganandam and S. K. Adhikari, Fortran programs for the time-dependent Gross-Pitaevskii equation in a fully anisotropic trap, *Computer Physics Communications* 180.10:1888-1912 (2009)
- [40] T. Lahaye, C. Menotti, L. Santos, M. Lewenstein and T. Pfau, The physics of dipolar bosonic quantum gases, *Reports on Progress in Physics* 72. 12: 126401 (2009)
- [41] L. Landau, Theory of the superfluidity of helium II, *Phys. Rev.* 60, 356-358 (1941)
- [42] H. K. Onnes, Investigations into the properties of substances at low temperatures, which have led, amongst other things, to the preparation of liquid helium. Nobel lecture, 4 (1913)
- [43] P. L. Kapitsa, Viscosity of Liquid Helium below the λ -Point, *Nature* 141, 74 (1938)
- [44] A. J. Leggett, Bose-Einstein condensation in the alkali gases: Some fundamental concepts, *Rev. Mod. Phys.*, 73(2):307-356 (2001)
- [45] G. E. Astrakharchik and L. P. Pitaevskii, Motion of a heavy impurity through a Bose-Einstein condensate, *PRA* 70.1:013608 (2004)
- [46] F. Pinsker, Gaussian impurity moving through a Bose-Einstein superfluid, *Physics of Condensed Matter*, Vol. 521, p.36-42 (2017)
- [47] Z. Yu, Landau's criterion for an anisotropic Bose-Einstein condensate, *PRA* 95.033618 (2017)

- [48] T. Koch, T. Lahave, J. Metz, B. Fröhlich, A. Griesmaier and T. Pfau, Stabilization of a purely dipolar quantum gas against collapse, *Nature physics*, 4(3), 218. (2008)
- [49] C. Ticknor, R. Wilson and J. Bohn, Anisotropic superfluidity in a dipolar Bose gas, *PRL* 106(6), 065301 (2011)
- [50] R. Onofrio, C. Raman, J. Vogels, J. Abo-Shaeer, A. Chikkatur and W. Ketterle, Observation of superfluid flow in a Bose-Einstein condensed gas, *PRL* 85(11), 2228. (2000)
- [51] Y. Tang, A. Sykes, N. Burdick, J. DiSciaccia, D. Petrov and B. Lev, Anisotropic expansion of a thermal dipolar Bose gas, *PRL* 117(15), 155301 (2016)
- [52] J. Weiner, V. Bagnato, V. Zilio and P. Julienne, Experiments and theory in cold and ultracold collisions, *Reviews of Modern Physics*, 71(1), 1 (1999)
- [53] P. Julienne and J. Vigue, Cold collisions of ground- and excited state alkali-metal atoms, *PRA* 44.7: 4464 (1991)
- [54] D. Blume and C. Greene, Fermi pseudopotential approximation: Two particles under external confinement, *PRA* 65(4), 043613 (2002)
- [55] T. Lahaye, C. Menotti, L. Santos, M. Lewenstein and T. Pfau, The physics of dipolar bosonic quantum gases, *Reports on Progress in Physics*, 72(12), 126401 (2009)
- [56] L. Salasnich, Time-dependent variational approach to Bose-Einstein condensation, *International Journal of Modern Physics B*, 14(1), 1-11 (2000)
- [57] A. Fetter, Vortices and Dynamics in Trapped Bose-Einstein Condensates, *Journal of Low Temperature Physics* 161(5-6), 445-459 (2010)
- [58] Y. Tang, A. Sykes, N. Burdick, J. Bohn and B. Lex, s-wave scattering lengths of the strongly dipolar bosons Dy 162 and Dy 164, *PRA*, 92(2), 022703 (2015)
- [59] Y. Tang, A. Sykes, N. Burdick, J. Bohn and B. Lev, Erratum: s-wave scattering lengths of the strongly dipolar bosons Dy 162 and Dy 164 [*PRA* 92, 022703 (2015)], *PRA* 93(5), 059905 (2016)
- [60] N. Parker, B. Jackson, A. Martin and C. Adams, Vortices in Bose-Einstein Condensates: Theory. In *Emergent Nonlinear Phenomena in Bose-Einstein Condensates* (pp. 173-189), Springer, Berlin, Heidelberg (2008)
- [61] M. Tsubota, K. Kasamatsu and M. Kobayashi, Quantized vortices in superfluid helium and atomic Bose-Einstein condensates, *arXiv preprint arXiv: 1004.5458* (2010)
- [62] K. Madison, F. Chevy, W. Wohlleben and J. Dalibard, Vortex formation in a stirred Bose-Einstein condensate, *PRL* 84(5), 806 (2000)
- [63] K. Madison, F. Chevy, W. Wohlleben and J. Dalibard, Vortices in a stirred Bose-Einstein condensate, *Journal of Modern Optics*, 47(14-15), 2715-2723 (2000)

- [64] Y. Cai, Y. Yuan, M. Rosenkranz, H. Pu and W. Bao, Vortex patterns and the critical rotational frequency in rotating dipolar Bose-Einstein condensates, arXiv preprint arXiv: 1801.07225 (2018)
- [65] L. Mingarelli, E. Keaveny and R. Barnett, Vortex lattices in binary mixtures of repulsive superfluids, PRA 97(4), 043622 (2018)
- [66] R. Kumar, L. Tomio, b. Malomed and A. Gammal, Vortex lattices in binary Bose-Einstein condensates with dipole-dipole interactions, PRA 96(6), 063624 (2017)
- [67] B. Ouboter, Heike Kamerlingh Onnes's discovery of superconductivity, Scientific American 276(3), 84-9 (1997)
- [68] I. Bloch, J. Dalibard and W. Zwerger, Many-body physics with ultracold gases, Rev. Mod. Phys. 80, 885 (2008)
- [69] S. Ianeselli, C. Menotti and A. Smerzi, Beyond the Landau criterion for superfluidity, Journal of Physics B: Atomic, Molecular and Optical Physics, 39(10), S135 (2006)
- [70] S. Subramaniyan, Vortex formation and hidden vortices in dipolar Bose-Einstein condensates, Physics Letters A, 381(36), 3062-3065 (2017)
- [71] B. Mulkerin, D. O'Dell, A. Martin and N. Parker, Vortices in the two-dimensional dipolar Bose gas, In Journal of Physics: Conference Series (Vol. 497, No. 1, p. 012025). IOP Publishing (2014)
- [72] Q. Chen, J. Stajic, S. Tan and K. Levin, BCS-BEC crossover: From high temperature superconductors to ultracold superfluids. Physics Reports, 412(1), 1-88 (2005)
- [73] Y. Lozonik and V. Yudson, Feasibility of superfluidity of paired spatially separated electrons and holes; a new superconductivity mechanism. JETP letters, 22(11), 274-276 (1975)
- [74] W. Lamb, Nobel lecture: Fine structure of the hydrogen atom, Nobel Lecture, December 12, 1955
- [75] W. Ketterle, Nobel lecture: When atoms behave as waves: Bose-Einstein condensation and the atom laser. Reviews of Modern Physics, 74(4), 1131 (2002)
- [76] S. Haroche, Nobel lecture: Controlling photons in a box and exploring the quantum to classical boundary. Reviews of Modern Physics, 85(3), 1083 (2013)
- [77] C. Cohen-Tannoudji and D. Guery-Odelin, Advances in atomic physics: an overview. (2011)
- [78] X. He, Dynamic analysis of vortex lifetime in 2-D and 3-D turbulence simulations. Physica D: Nonlinear Phenomena, 37(1-3), 453-462 (1989)

Danksagungen

Am Ende möchte ich mich noch bei all jenen bedanken, die mich in den letzten Monaten während der Erstellung dieser Arbeit unterstützten. Besonderer Dank gilt hierbei:

- **Prof. Dr. Tilman Pfau** für die Möglichkeit diese Arbeit an seinem Institut anzufertigen, sowie die Ermöglichung so mancher unterhaltsamer, geselliger wie lehrreicher Unternehmungen von Oberstdorf bis nach Erlangen.
- **Prof. Dr. Peter Michler** für die Zeit, die er sich für unsere Gespräche genommen hat, sowie seine vielen interessierten Rückfragen die zur Verbesserung unser beider Verständnis des Themas beitrugen und viele Denkanreize boten, die meine weiteren Analysen geprägt haben.
- **Matthias Wenzel, Fabian Böttcher, Jan-Niklas Schmidt und Igor Ferrier-Barbut** für die fantastische gemeinsame Zeit in und außerhalb der Universität, die vielen kleinen Projekte, die mir auch fernab des direkten Wirkens an der Masterarbeit die Möglichkeit gaben vielerlei experimentelle wie technische Fähigkeiten auszubauen, sowie die Ruhe und Geduld wenn mal nicht alles nach Plan lief.
- **Carl Bühner** für die gemeinsam verbrachte Zeit in und außerhalb der Arbeit, besonders während der unglaublich fruchtbaren Diskussionen auf gemeinsamen Zugfahrten.
- Dem **PI5-IT-Team**, namentlich **Daniel Weller, Nicolas Zuber** und **Harald Kübler**, den stillen Helden des Instituts, ohne deren unermüdliches Engagement wir alle verloren, und die numerischen Resultate dieser Arbeit nicht möglich gewesen wären. Besonderer Dank gilt hier **Daniel** für seine Hilfe und unendliche Geduld besonders zu Beginn meiner Simulationsarbeit, als ich mitunter mehrfach täglich sein neugieriger, wie verzweifelter Besucher war.
- natürlich dem gesamten **Rest des 5. Physikalischen Instituts** für eine einmalige Arbeitsatmosphäre und viele anregende Gespräche am und außerhalb des Arbeitsplatzes.